Title
Tidal and Seasonal Observations of Stratification and Water Temperature in Lower SouthSan Francisco Bay

Author
Hoang, Olivia

Publication Date
2019

Peer reviewed|Thesis/dissertation

Tidal and Seasonal Observations of Stratification and Water Temperature in Lower South San Francisco Bay

by

Olivia Hoang

A dissertation submitted in partial satisfaction of the

requirements for the degree of

Doctor of Philosophy

in

Engineering - Civil and Environmental Engineering

in the

Graduate Division

of the

University of California, University of California, Berkeley

Committee in charge:

Professor Mark Stacey, Chair
Professor Evan Variano
Associate Professor Laurel Larsen
Dr. Christopher Holleman

Fall 2019

Tidal and Seasonal Observations of Stratification and Water Temperature in Lower South San Francisco Bay

Abstract

Tidal and Seasonal Observations of Stratification and Water Temperature in Lower South San Francisco Bay

by

Olivia Hoang

Doctor of Philosophy in Engineering - Civil and Environmental Engineering

University of California, University of California, Berkeley

Professor Mark Stacey, Chair

San Francisco Bay sits within a highly urbanized community and is home to endangered species and fish nurseries. The surrounding dense population creates large wastewater effluent resulting in high nutrient levels in the estuary. Scientists wonder why there have not been annual phytoplankton blooms as observed in other estuaries with lower nutrient levels such as the Chesapeake Bay [8]. Some have hypothesized it is due to high turbidity levels and tidal breakdown of stratification creating nonideal environments for phytoplankton growth. However, decadal-trends show that the estuary is becoming less turbid, and with changes in climate patterns, there is potential for persistent stratification.

This dissertation breaks down the mechanics responsible for observed development of stratification over the ebb tide and destratification at the end of ebb to mid flood tides. Results reveal longitudinal mechanics are primarily responsible for development and destruction of stratification at times of high velocity. During tide transitions, lateral exchange allows for the interaction of perimeter-shoal waters. Seasonal differences in salinity and water temperature are observed in order to develop an understanding of how the estuary responds to various climates. Seasonal trends indicate changes in precipitation lead to high variability of the magnitude and range of salinity, magnitude of stratification, and perimeter water temperature. Salinity and temperature observations are used to calculate residence time and longitudinal dispersion rates for Lower South San Francisco Bay. Present-day conditions reveal stratification is broken down on each tide, but further research should be done applying these observed salinity and temperature gradients with adjustments for potential future climate conditions.

To my parents, Phil and Jennifer Hoang,

the two people who have shown me unconditional love and support every single day of my life.

Contents

Contents **ii**

List of Figures **iv**

List of Tables **xi**

1 Introduction **1**
1.1 Estuarine Hydrodynamics . . . 2
1.2 Channel versus Shoal . . . 4
1.3 Stratification . . . 4
1.4 Longitudinally Driven Tidal Straining . . . 5
1.5 Laterally Driven Stratification . . . 5
1.6 Stratification and Turbulent Mixing . . . 6
1.7 Stratification and Shear . . . 7

2 Longitudinal versus Lateral Estuarine Dynamics and Their Role in Tidal Stratification Patterns in Lower South San Francisco Bay **8**
2.1 Introduction . . . 9
2.2 Methods . . . 11
2.3 Overview of Conditions . . . 13
2.4 Analysis . . . 22
2.5 Discussion . . . 28
2.6 Concluding Remarks . . . 32

3 Using Eulerian Temperature Measurements to Estimate Residence Time in Lower South San Francisco Bay **35**
3.1 Introduction . . . 35
3.2 Data Sources and Box Model . . . 37
3.3 Results . . . 51
3.4 Discussion . . . 52
3.5 Conclusions . . . 54

4 Seasonal Variability in Lower South San Francisco Bay **55**

4.1 Introduction 55
4.2 Deployment Site 56
4.3 Equipment Deployed 56
4.4 CIMIS and SFEI Moored Sensors 57
4.5 Annual Cycle 61
4.6 Comparison of Fall 2015, Winter 2015-2016, and Winter 2016-2017 Seasons . 64
4.7 Event Response, Winter 2015-2016 76
4.8 Summary 81

5 Conclusions **82**

Bibliography **86**

List of Figures

1.1 Graphic of longitudinally driven tidal straining described by Simpson (1990) [52] 5

2.1 Bathymetry in Lower South San Francisco Bay consisting of a deeper, center channel in the Northwest to Southeast direction with broad, shallow shoals. White dots show where lines of CTD and ADCPs were placed for field deployment. Shades of purple correspond to -15 m MLLW, dark blue -6 m MLLW, light blue 0 m MLLW, and green 3 m MLLW. Positive x is defined in the southeast direction. Positive y is defined in the northeast direction. Line 2 is centrally located and lies at $y = 0$. See more details on mooring water depths in Table 2.1. Bathymetry from 2005 Hydrographic Survey of South San Francisco Bay, California [16] . . . 12

2.2 Salinity [PSU] and precipitation [mm] plot. Precipitation data from the California Irrigation Management Information System (CIMIS) station in Union City [58]. Note: Flood tides correspond to gray shading. Ebb tides correspond to white shading. Hatching refers to larger flood/ebb tides when there is a diurnal asymmetry. See Figure 2.6 for the longitudinal velocity time series clarifying shading and hatching periods. 14

2.3 Stratification (S_z) shown in units of PSU, is calculated by taking the difference in measured salinities in the bottom and top CTDs on line 2. Note: Flood tides correspond to gray shading. Ebb tides correspond to white shading. Hatching refers to larger flood/ebb tides when there is a diurnal asymmetry. 16

2.4 Longitudinal salinity Gradient [PSU/m] calculated using instantaneous salinity measurements at lines 1 and 3. Top plot shows the average longitudinal salinity gradient and the bottom plot shows the vertical difference. Note: Flood tides correspond to gray shading. Ebb tides correspond to white shading. Hatching refers to larger flood/ebb tides when there is a diurnal asymmetry. 17

2.5 The lateral salinity gradient [PSU/m] was calculated using instantaneous salinity measurements at lines 2 and 6. The average lateral salinity gradient was calculated using the top and bottom salinity measurements at line 2 and the top salinity measurement at line 6. Due to limitations in field measurements it is assumed that the water in the shoal is well-mixed at line 6 allowing us to use the top salinity measurement for the entire water column. The top lateral salinity gradient (dashed) is calculated by using only the measurements at the top of lines 2 and 6 which reveals a reversal sign by the end of the ebb tide meaning the shoal is saltier than the channel through differential advection. 19
2.6 Top and bottom longitudinal velocities [m/s] were calculated by averaging the longitudinal velocities in the top 2 m and the bottom 2 m of the water column. Tidal asymmetries were defined visually by the amplitude of the top longitudinal velocity. (A) shows the time variation of top and bottom longitudinal velocity and (B) shows the shear. Note: Flood tides correspond to gray shading. Ebb tides correspond to white shading. Hatching refers to larger flood/ebb tides when there is a diurnal asymmetry. 20
2.7 Top and bottom lateral velocities [m/s] were calculated by averaging the lateral velocities in the top 2 m and the bottom 2 m of the water column. (A) shows the time variation of top and bottom lateral velocity and (B) shows the shear. Large shear events consistently occur at the end of the ebb tide in both the spring and neap. Persistent lateral exchange, but small magnitude, occurs over the flood tide. Note: Flood tides correspond to gray shading. Ebb tides correspond to white shading. Hatching refers to larger flood/ebb tides when there is a diurnal asymmetry. 21
2.8 The measured rate of change of stratification (black), $\frac{\partial S_z}{\partial t}$ $[\frac{PSU}{s}]$, was calculated by taking the time derivative of the bottom-top salinity difference at line 2 and with a rolling-average window of 30 minutes. The calculated rate of stratification (blue), was calculated by taking the sum of observed values of longitudinal straining, longitudinal advection, lateral straining, and lateral advection. (A) Entire time series, (B) First, dry spring tide, (C) Second, wet spring tide. Note: Flood tides correspond to gray shading. Ebb tides correspond to white shading. Hatching refers to larger flood/ebb tides when there is a diurnal asymmetry. 22
2.9 Longitudinal straining and longitudinal advection in [PSU/s]. Longitudinal salinity gradients were calculated using lines 1 and 3. (A) Entire time series, (B) First, dry spring tide, (C) Second, wet spring tide. Note: Flood tides correspond to gray shading. Ebb tides correspond to white shading. Hatching refers to larger flood/ebb tides when there is a diurnal asymmetry. 25
2.10 Lateral straining and lateral advection in [PSU/s]. Lateral salinity gradients were calculated using lines 2 and 6. (A) Entire time series, (B) First, dry spring tide, (C) Second, wet spring tide. Note: Flood tides correspond to gray shading. Ebb tides correspond to white shading. Hatching refers to larger flood/ebb tides when there is a diurnal asymmetry. 27

2.11 Velocity vectors at line 2 shows differences in lateral exchange flow patterns in the ebb to flood versus the flood to ebb tide transitions. Red arrows represent the bottom depth flows and the yellow arrows represent the top flow directions. (A) At the ebb to flood transition we see a pulse of lateral flow from the near bed shoal to the mid-column channel. Note the pictured longitudinal shear that occurs during this tidal transition. As the tide transitions from ebb to flood, the bottom reverses sign before the top. (B) At the flood to ebb transition we see a two-layer lateral exchange flow where the bottom is directed from the channel to the shoal and the flow at the top of the water column is directed from the shoal to the channel. Ebb tides correspond to white shading. Hatching refers to larger flood/ebb tides when there is a diurnal asymmetry. 28

2.12 Longitudinal (green) and lateral (red) Simpson Numbers at line 2 [26]. The larger the value of the Simpson number, the more likely the water column is to stratify. Note: Flood tides correspond to gray shading. Ebb tides correspond to white shading. Hatching refers to large flood/ebb tides when there is a diurnal asymmetry. 30

2.13 Fill plot of measured versus calculated $\frac{\partial S_z}{\partial t}$ $[\frac{PSU}{s}]$. Note the vertical distance shown for each color is the contribution of that term. The areas are not overlaid, so the magnitude of lateral straining is added onto the area of longitudinal straining, not behind. The positive area has not had the negative area subtracted from it. By adding the positive area and the negative area at each time step, you would get the blue lines shown in Figure 2.8. The measured value of $\frac{\partial S_z}{\partial t}$ is plotted in black. (A) Shows the first, dry spring tide. (B) Zooms into 4 tidal cycles outlined by the black box in subplot A. (C) Shows the second, wet spring tide. (D) Zooms into 4 tidal cycles outlined by the black box in subplot C. 33

2.14 Tidal phase averaged calculated longitudinal straining, longitudinal advection, lateral straining, and lateral advection. Longitudinal gradients were calculated using lines 1 and 3 to estimate and lateral gradients using lines 2 and 6 . The first half shows tidally-averaged values over the ebb tide, and the second half in gray shows tidally-averaged values over the flood tide. Longitudinal straining works to create stratification from mid-ebb until mid-flood. Longitudinal advection creates stratification at the end of the ebb tide and then works to destratify at the beginning of the flood tide. Lateral straining becomes important at the end of the ebb tide and the end of the flood tide. At the end of the ebb tide, lateral straining creates stratification and over mid to late-flood lateral straining overstrains the water column inputting turbulent energy maintaining a homogeneous vertical salinity structure in the channel. 34

3.1 Locations of observed temperatures. Water temperature at San Mateo Bridge and Alviso Slough were collected by the San Francisco Estuary Institute's (SFEI) moored sensors program. Water temperature at LSSFB is an original data set collected by UC Berkeley. 38

3.2 Control volumes used to represent the ocean, estuary, and perimeter for the temperature exchange model where $K_{D,1}$ represents the diffusive flux between the estuary and perimeter surface area and $K_{D,2}$ represents the diffusive flux between the estuary and ocean surface area. 39
3.3 Measured conditions for the time window of interest. Top left figure shows measured solar radiation in $\frac{W}{m^2}$ along with hourly precipitation. Top right figure shows measured air temperature in degrees Celsius. Bottom left figure displays wind speed in $\frac{m}{s}$. Lastly, the bottom right figure shows measured water temperatures for the perimeter, estuary, and ocean control volumes. The perimeter water temperature is measured at Alviso and the ocean water temperature is measured at San Mateo. Refer to Figure 3.1 for a map of these locations. 42
3.4 Thermal heating and cooling contributions from each variable in Table 3.1 where H_S is the sensible heat transfer, H_L is the heat loss due to evaporation, H_1 is the long wave radiation, H_2 is the back radiation from the water surface and H_{SW} is the short wave radiation that is directly measured from CIMIS. Variables H_S and H_2 are dependent on water surface temperature which varies for the estuary and perimeter. Estuary values of H_S and H_2 are shown by dashed lines. The values displayed in this figure show the daily thermal energy contributed to the estuary or perimeter control volumes from each H contributor. H in $\frac{W}{m^2}$ is converted to thermal energy in $\frac{J}{m^2}$ by integrating hourly calculations/observations of H-values over the entire day. 43
3.5 Varying techniques used to look at a single value to represent the daily temperature in the estuary. Time and tidal schemes were used including taking the daily average, taking the daily minimum, taking the daily maximum, taking the temperature that occurred at 6 AM on each day, taking the temperature that occurred at 6 PM on each day, taking temperature at the time the daily lowest low water level occurred, and taking the temperature at the time the daily highest high water level occurred. 44
3.6 Root mean square error modeled versus observed for $K_{D,1}$ ranging from 0 to 200 m^2/s and $K_{D,2}$ ranging from 30 to 100 m^2/s. The length of the estuary, perimeter, and ocean is set to 6440 meters, 2250 meters, and 12,870 meters respectively. Depth of the estuary, perimeter, and ocean is 2 meters, 2 meters, and 15 meters. The first table contains RMSE for modeled versus observed temperature time series in the estuary. The second table is for perimeter comparisons. The last table is a weighted average of the estuary, perimeter RMSE values (weight by volume, 75% estuary, 25% perimeter). The model is run from May 29, 2016 to August 1, 2016 with $C_{P,H_2O} = 4186\ \frac{J}{kg\ degC}$, $\rho_{H_2O} = 1000\ \frac{kg}{m^3}$, estuary depth = 2 m, perimeter depth = 2 m. 46

3.7 Modeled versus measured estuary and perimeter temperatures using $K_{D,1} = 2\ m^2/s$, $K_{D,2} = 50\ m^2/s$. Model was run for temperatures beginning May 26, 2016 and ending August 31, 2016 with an initializing estuarine temperature of 15.8 degrees Celsius, initial perimeter temperature of 17.9 degrees Celsius, and a constant ocean input temperature of 20 degrees Celsius. 47
3.8 Step ocean temperature input where $T_o = 17.5$ deg C April 1 - May 31 and $T_o = 21$ deg C June 1 - August 31, perimeter water depth of 2 meters, estuary water depth of 10 meters. $K_{D,1} = 100\ m^2/s$, $K_{D,2} = 50\ m^2/s$. Model was run for temperatures beginning April 1, 2016 to August 31, 2016. The initial estuary temperature is set to 15.8 deg C and the initial perimeter temperature is set to 17.8 deg C. 48
3.9 Constant ocean temperature input of 20 deg C, perimeter water depth of 2 meters, varying estuary water depth of 2 meters, 3 meters, 4 meters, and 5 meters . . . 49
3.10 In order to determine the sensitivity of selected lengths plugged into equations 3.13 and 3.14, this figure shows how adjustments in the length of estuary, length of perimeter, and length of the ocean affects the final residence times for a given $K_{D,1} = 100\ m^2/s$ and $K_{D,2} = 50\ m^2/s$. Only one value was adjusted for each calculation in order to understand the sensitivity of $T_{perimeter}$ and of $T_{estuary}$ to that variable. Original values used to calculate $T_{perimeter,\ original}$ and $T_{estuary,\ original}$ are $L_{estuary} = 6440$ meters, $L_{perimeter} = 2250$ meters, $L_{ocean} = 12,870$ meters. . . 50
3.11 Implicit modeled versus measured estuary and perimeter temperature beginning May 26, 2016. Estuary and perimeter depth is set to 2 meters. $K_{D,1}$ is set to 100 m^2/s and $K_{D,2}$ is set to 50 m^2/s 51

4.1 Monthly precipitation sums from San Francisco Downtown Station (RG31) Data from 1907 - 2018. Bar graphs display the monthly sum of precipitation in inches at Union City from Table 4.4. Note: Monthly precipitation is available from January 2015 - April 2017. 57
4.2 CIMIS weather station location: Union City No. 171. 58
4.3 SFEI nutrients program deployment locations and depth of sensors 59
4.4 Top water temperature at channel marker 17 in degrees Celsius 62
4.5 Measured seasonal salinity with biofouling removed at channel marker 17. Measured stratification calculated by taking the difference between the measured salinity at the bottom of the water column and the measured salinity at the top of the water column. We were unable to recover the measured salinity from the bottom CTD during the orange deployment (October 2016 - January 2017), so there is no measured stratification during that period. 63

4.6 Longitudinal (top panel) and lateral (bottom panel) salinity in PSU during wet, winter season (2016-2017). Middle panel is the salinity difference between Dumbarton and CM17. Dumbarton is located down estuary from CM17 while Coyote and Mowry are located up estuary. Precipitation at Union City shown in mm. The middle panel displays the longitudinal salinity difference between Dumbarton and CM17. Note: Flood tides correspond to gray shading. Ebb tides correspond to white shading. Hatching refers to larger flood/ebb tides when there is a diurnal asymmetry. The start of each tide is determined by the vertically averaged longitudinal velocity. 66
4.7 Longitudinal and lateral water temperatures during wet, winter season (2016-2017). Dumbarton is located down estuary from CM17 while Coyote and Mowry are located up estuary. Note: Flood tides correspond to gray shading. Ebb tides correspond to white shading. Hatching refers to larger flood/ebb tides when there is a diurnal asymmetry. The start of each tide is determined by the vertically averaged longitudinal velocity. 67
4.8 Longitudinal and lateral salinity in PSU during winter season (2015-2016). Dumbarton is located down estuary from CM17 while Coyote and Mowry are located up estuary. Note: Flood tides correspond to gray shading. Ebb tides correspond to white shading. Hatching refers to larger flood/ebb tides when there is a diurnal asymmetry. The start of each tide is determined by the vertically averaged longitudinal velocity. 68
4.9 Longitudinal and lateral water temperatures during winter season (2015-2016). Dumbarton is located down estuary from CM17 while Coyote and Mowry are located up estuary. Note: Flood tides correspond to gray shading. Ebb tides correspond to white shading. Hatching refers to larger flood/ebb tides when there is a diurnal asymmetry. The start of each tide is determined by the vertically averaged longitudinal velocity. 69
4.10 Longitudinal salinity in PSU during dry, fall season (2015). Dumbarton is located down estuary from CM17 while Coyote is located up estuary. Note: Flood tides correspond to gray shading. Ebb tides correspond to white shading. Hatching refers to larger flood/ebb tides when there is a diurnal asymmetry. The start of each tide is determined by the vertically averaged longitudinal velocity. 70
4.11 Air temperature (black line) and water temperatures (colored lines) in degrees Celsius during dry, fall season (2015) 71
4.12 Historical sunrise and sunset times from timeanddate.com for San Jose, California in September 2015 and Water temperatures for two days (September 21, 2015 and September 22, 2015) in dry, fall season (2015). The x-axis is the local hour (PDT). Note: Flood tides correspond to gray shading. Ebb tides correspond to white shading. Hatching refers to larger flood/ebb tides when there is a diurnal asymmetry. The start of each tide is determined by the vertically averaged longitudinal velocity. 73

4.13 Scatter plot of channel velocity versus top salinity for three varying seasons at CM17 within the deep channel of LSSFB (*34.47798, -122.07658*). In increasing buoyancy input: September 2015, February 2016, and January 2017. Positive channel velocities correspond to flood tides and is shaded in gray. Negative channel velocities correspond to ebb tides and has a white background. A few tides were selected out of the deployment for these scatter plots: September 13 - 16, 2015, February 22 - 25, 2016, and January 27 - 29, 2017. 74
4.14 Scatter plot of channel velocity versus stratification for three varying seasons at CM17 within the deep channel of LSSFB (*34.47798, -122.07658*). In increasing buoyancy input: September 2015, February 2016, and January 2017. Positive channel velocities correspond to flood tides and is shaded in gray. Negative channel velocities correspond to ebb tides and has a white background. Stratification is calculated by taking the difference between the measured salinity at the bottom of the water column and the measured salinity at the top of the water column. A few tides were selected out of the deployment for these scatter plots: September 13 - 16, 2015, February 22 - 25, 2016, and January 27 - 29, 2017. 75
4.15 Measured salinity at various locations in LSSFB. Dumbarton, CM17 (average of top, middle and bottom), and Coyote are located along-channel in LSSFB while Mowry is across-channel from CM17. Both Coyote and Mowry are located in shallow sloughs at the perimeter. Highlighted areas show salinity recovery after a precipitation event. 77
4.16 Top, middle, and bottom salinity at CM17 and precipitation at Union City during a wet, rainy winter season (December 2015 - January 2016). Highlighted time windows used to observe the salinity recovery rate after the each event. 78
4.17 Average top, middle, and bottom salinity (black line), daily minimum (red dot), with an exponential decay fit ($S(t) = S_* - Ce^{-t/T_d}$) for CM17 in LSSFB during the winter 2015 - 2016 season. Green fit: $S = 30.9$ PSU, $C = 9.91$ PSU , $T_d = 1.24 \times 10^6$ s; Red fit: $S = 26.3$ PSU, $C = 6.08$ PSU , $T_d = 5.91 \times 10^5$ s; Blue fit: $S = 4250$ PSU, $C = 4.23 \times 10^3$ PSU , $T_d = 7.36 \times 10^8$ s. 79
4.18 Average top, middle, and bottom salinity (black line), daily minimum (red dot), with the solution to the heat initial value problem with Heaviside initial conditions ($S(x,t) = S_0 + C \times erf(\frac{19{,}270}{\sqrt{4Kt}})$) for CM17 in LSSFB during the winter 2015 - 2016 season. Green fit: $S_0 = 33.8$ PSU, $C = -12.4$ PSU, $K = 261\ m^2/s$; Red fit: $S_0 = 28.2$ PSU, $C = -7.96$ PSU, $K = 624\ m^2/s$; Blue fit: $S_0 = 29.9$ PSU, $C = -10.4$ PSU, $K = 295\ m^2/s$. 80

5.1 Top panel is a sketch of LSSFB over an ebb tide. Note: After the end of a flood tide, the lateral density gradient can reverse due to differential advection meaning the channel is more saline than the shoals. The bottom panel describes the characteristics in the tidal creation and destruction of stratification. 83
5.2 Snapshots of lateral cross-sections in LSSFB over a tidal cycle. The figure should be read in a clockwise direction. 84

List of Tables

2.1 Mooring detailed locations and water depths. Each CTD measures depth below the water surface. Here we display the average depth that the CTDs measured throughout the deployment. The column labeled NAVD88 provides the referenced depths from a Lower South Bay bathymetry dataset collected by the San Francisco Estuary Institute (SFEI) available on their ERDDAP website. The water depth at each mooring is estimated by taking the difference of the MSL at Alameda (0.98 m from NOAA Tides and Currents [38]) from the NAVD88 bathymetry. 13

3.1 Equations used to calculate thermal heating where H values are in units of $[\frac{W}{m^2}]$, C_S is the coefficient for wind stress variability [-], ρ_A is the air density $[\frac{kg}{m^3}]$, C_P is the specific heat of air $[\frac{J}{kg^\circ C}]$, U is the wind speed at 10 m $[\frac{m}{s}]$, T_0 is the water surface temperature $[^\circ C]$, and T is the air temperature at 10 m $[^\circ C]$, C_L is the coefficient for wind stress variability [-], L_W is the latent heat of evaporation $[\frac{J}{kg}]$, Q_0 is the saturation specific humidity [kg of water moisture/kg of air-water moisture], and Q is the specific humidity at 10 m. 41
3.2 Corresponding residence times to values of $K_{D,1}$ and $K_{D,2}$. Calculated by equations 3.13 and 3.14. 47

4.1 Deployment overview at channel marker 17 (CM17) (*37.47798, -122.07658*). Note: Temperature, depth, and velocity data is available from the start of each deployment to the start of the following deployment with a small data gap due to the recovery and redeployment time. These sensors were not affected by biofouling like the conductivity sensor. 58
4.2 Locations of SFEI nutrients program sensors corresponding with Figure 4.3 [60] 59
4.3 Habitat and water depths of SFEI nutrients program corresponding with Figure 4.3 [60] 60
4.4 Monthly precipitation (inches) at Union City; data from CIMIS [58] 61

Acknowledgments

I am grateful for Mark Stacey whose advising deserves praise and acknowledgement. Over the past 6 and a half years, Mark has been an integral part of the completion of this dissertation. Mark's ability to quickly digest new findings while also offering insight and guidance on how to take those findings to the next step is difficult to find. I benefited greatly from Mark's wit and experience. Mark, thank you for your editorial help, for pushing me when I needed motivation, and for being understanding when I needed to take time to care for myself. I am grateful to have had you as an advisor.

To my fiancé, Gabriel Yip, thank you for being my biggest fan, my day-to-day confidant, and my break when I need to step away from dissertation writing. Thank you for your willingness to drive from the Sunset District to East Bay to work next to me in my favorite cafes and to share meals with me. Thank you for helping me keep proper perspective of my purpose and hope in a way that allowed me to, piece by piece, put this document together. Without you, this would not have been as joyful of a process. I appreciate your love and support.

Thank you to my senior colleagues, David Senn, Rusty Holleman, and Lissa MacVean for offering ideas and interpretations. Rusty, your passing comment in a conference lunch line, "why not 3D?" is what drove me to do the three-dimensional deployment which lead to the analysis done in chapter 2.

Thanks to the San Francisco Bay Nutrient Management Strategy and National Science Foundation (NSF) for funding support work. A special thank you to Francis Parchaso and Sarah Pearson at United States Geological Survey (USGS) for the in-kind financial and physical support required to accomplish this field work and analysis. Thank you Rachel Allen at UC Berkeley for the accompaniment and strength required to cycle this deployment over the past year.

Dad, thank you for uprooting your life in Vietnam in search of a better future for our family. Thank you for teaching me the importance of education. Thank you for supporting and encouraging me especially when things in life inevitably didn't go according to plan. I admire your grateful heart, your consistent affirmation of love, your humble demeanor, and your emotional stability. Mom, thank you for your unending willingness to serve your family. Thank you for driving me to all my extracurricular activities as a kid while working a full time job and simultaneously managing to make home cooked meals every day. I honestly have no idea how you do it. I admire your servant heart and intuitive wisdom. Thanks to you both I had a top notch education from Laurel Mountain Elementary School, Canyon Vista Middle School, Westwood High School, the University of Texas, Austin and the University of California, Berkeley. As I grow older, I grow more aware of my educational privilege. I grow prouder of my immigrant family roots. My heart is so grateful.

To my younger sister, Andrea, and younger brother, Nathan, thank you for the daily joys. Thank you for opening my eyes to my own faults and shortcomings out of love and care for me. Thank you for being the constants in my life even as I moved away from Texas. Thank you for celebrating the good and mourning the difficult with me. Your support and

presence in my life has brought me much joy, and I hope you both know how precious you are to me.

Lastly, thank you to my amazing friends who have been through the many ups and downs with me over the past years. To Christine and Vinayak Agarwal, Jonny Chung, Amy Wu Silva, thank you for being my constant friend throughout my graduate studies. It has been a privilege to walk through this season of life with you all.

Data presented in this manuscript are available at https://doi.org/10.6078/D14H5K.

Chapter 1

Introduction

San Francisco Bay lies within a highly dense, urban community. It is surrounded by large cities such as San Francisco, San Jose, and Oakland. Rivers such as the Sacramento River, San Joaquin River, Petaluma River, Napa River, and Guadalupe River feed into the San Francisco Bay. San Francisco Bay is connected to the Pacific Ocean at the Golden Gate Bridge. The estuary is surrounded by wetlands providing habitat for fish, birds, and other wildlife. Estuaries such as San Francisco Bay provide economic benefits for coastal communities. They allow surrounding cities to participate in international commerce, provide recreation, and draw tourism. Maintaining healthy estuaries benefits both the local community as well as provides habitat for wildlife.

In the 1850s, sediment was inputted into the bay through hydraulic mining. Decadal trends reveal the water in San Francisco Bay is becoming less turbid as the sediment is being flushed out [11]. With increasingly clear water columns and dynamic changes in the climate, scientists are beginning to worry about potential algal blooms in Lower South San Francisco Bay. Nutrients from wastewater inputs and agricultural runoff in San Francisco Bay have been considered nonlimiting in terms of nitrate, silicate, phosphate, and ammonium [59]. Previous studies attribute low rates of primary productivity to limited light availability and benthic grazing [11].

Seasonal phytoplankton blooms have been observed after high freshwater flow [11, 29]. Following high freshwater input events, a stratified water column results in ideal conditions for phytoplankton in the surface layer. Stratification can act as a barrier making it more likely that a phytoplankton in the top layer will remain in the photic zone protected from benthic grazing.

There has been little work done in observing seasonal stratification dynamics in South San Francisco Bay. Since Lower South San Francisco Bay (defined as the waterbody south of Dumbarton Narrows) is highly coupled with its surrounding perimeter, studying this specific part of the bay will offer insight on how channels interact with its perimeter in an estuary. As the bay continues to clear and changes in climate result in more extreme precipitation events, it becomes increasingly important to understand the mechanisms driving stratification patterns in San Francisco Bay.

Most literature in the past focuses on either longitudinal or lateral mechanisms responsible for the creation and destruction of stratification on a tidal time scale. Lacy's findings in North San Francisco Bay demonstrate the importance of lateral dynamics in the formation of the vertical salinity structure [25]. In 2001, Stacey found that the variation in stratification at another location in North San Francisco Bay could be described through longitudinal dynamics where stratification developed over the ebb tides and destratification occurred over the flood tides. This dissertation aims to understand how longitudinal and lateral dynamics create and destroy stratification in Lower South San Francisco Bay.

1.1 Estuarine Hydrodynamics

Estuaries are embayments along the coast that have a source of salty, ocean water and a source of buoyant freshwater typically from river discharge or land runoff. There is creation of stratification as freshwater is pulled into the brackish system and deconstruction of stratification from tidal, current, and wind mixing. The balance of these two competing forces has been used to parameterize various estuaries around the world [22]. Understanding the hydrodynamics in estuaries serves as an important building block for understanding nutrient budgets [8], the flushing rate of dissolved contaminants, coastal hypoxia [29] and its connection to the acidification of the ocean [33].

Residence Time

In the past, observations in estuaries have been primarily focused on tidally-averaged terms in order to understand exchange flows and estuarine circulation. Various definitions of transport time scales have been defined for biological, hydrologic, and geochemical applications. Residence time, or flushing time, is conceived as a time quantity that a water-mass is retained within defined boundaries [35]. The retention time of an estuary is the key parameter that controls nutrient budgets [8], longitudinal dispersion of passive tracers such as sediment and biological productivity [19]. In 1997, Bricelj and Lonsdale found that the occurrence of harmful algal blooms was strongly influenced by residence time [9]. However, due to spatial variability of residence time and challenges closing salinity and tracer budgets, each method to estimate estuarine residence time has its own set of assumptions and limitations. Chapter 3 and 4 in this dissertation offer alternative methods to estimate the residence time using observed data in Lower South San Francisco Bay.

Hydrodynamic Forcings

San Francisco Bay is a mesotidal estuary characterized by strong diurnal inequalities that vary with the spring-neap cycle. Flood and ebb tides are caused by gravitational pulls from the sun and moon. Each day there are two flood tides and two ebb tides. During the spring tide, there is an asymmetry between the two flood tides and between the two ebb tides in

a given day. The spring tide occurs when the moon, sun, and earth are aligned. This sync causes higher high tides and lower low tides because the forcing from the sun and the moon are compounded. The neap tide occurs when the line that connects the moon and the earth and the line that connects the sun and the earth are perpendicular to each other creating a less energetic tide and a smaller asymmetry between the tides in a given day. During the neap tide, the lows are higher and the highs are lower creating a more symmetric flood and ebb in a given day [39]. The spring-neap tidal cycle occurs on a two week time scale. San Francisco Bay has a combination of the principal semidiurnal lunar (M2) and solar (S2) tidal constituents. The combination of these two constituents results in a spring-neap cycle.

Estuarine hydrodynamics are also governed by the freshwater input which varies on a range of time scales from the order of minutes for precipitation events, to days for wastewater outputs, to months for seasonal variation, and to several years for weather patterns such as El Niño. Freshwater input in San Francisco Bay is highly dependent on precipitation events. In San Francisco Bay, winter months (November - February) are characterized by large and frequent rainfall events while the summer months (May - September) have little to no rainfall.

Both longitudinal and lateral flows are caused by two types of pressure gradients. These pressures can be derived from the hydrostatic equation which states that pressure increases with depth. By integrating the hydrostatic equation from the surface, h, to a given depth, z, we can get an expression for the pressure at a given depth, z.

$$\frac{\partial P}{\partial z} = -\rho g \tag{1.1}$$

We get the following expressions for the pressure gradient in the longitudinal and lateral directions:

$$\frac{\partial P}{\partial x} = \underbrace{\rho g \frac{\partial h}{\partial x}}_{BAROTROPIC} + \underbrace{\frac{\partial \rho}{\partial x} g(h-z)}_{BAROCLINIC} \tag{1.2}$$

$$\frac{\partial P}{\partial y} = \underbrace{\rho g \frac{\partial h}{\partial y}}_{BAROTROPIC} + \underbrace{\frac{\partial \rho}{\partial y} g(h-z)}_{BAROCLINIC} \tag{1.3}$$

The barotropic pressure gradient causes flow in the longitudinal and lateral directions by varying water surface levels. The baroclinic pressure gradient causes flows in the longitudinal and lateral directions by varying density gradients.

It is difficult to separate out barotropic and baroclinic forcing due to equipment uncertainty and difficulty resolving spatial variations of density gradients. In the past, baroclinic forcing is assumed to create top/bottom flow separation (opposing signs) where as barotropic forcing would not [25, 49]. However, there are barotropic mechanisms that could cause lateral flow separation such as laterally varying bathymetry, tidal rectification of Stoke's drift, and nonlinear advective terms in the momentum equation which proves looking soley at the top and bottom velocity signs to distinguish between barotropic pressure forcing vs baroclinic pressure forcing could be misleading [49].

As buoyant input will vary with changes in climate, baroclinic forcings will be changed which could cause impactful ramifications on the ecosystem. An increase in baroclinic pressure could lead to increased lateral exchange impacting the sediment transport leading to sourcing of the perimeter. In Lower South San Francisco Bay, sediments make up the marshland habitat which is home to endangered wildlife such as the salt marsh harvest mouse and Ridgway's rail, and serves as a nursery areas for young fish such as leopard sharks and steelhead [6].

1.2 Channel versus Shoal

Lower South San Francisco Bay estuary is characterized by a narrow in width, deep in depth channel that runs through the center with broad, shallow shoals on either side. Varying depths in the channel versus shoal cause differential advection, development of frontal features, and exchange between the channel and perimeter [49, 12].

There has been work done both in Lower South San Francisco Bay and in other estuaries that provide insight as to how variations in channel-shoal bathymetry affect the flow. In the York River estuary, a subestuary of the Chesapeake Bay, the largest lateral asymmetry in turbulent mixing occurred at the end of the ebb tide which delayed the onset of the flood tide in the channel where as in the shoal the tidal transition from ebb to flood was more rapid resulting in a lateral asymmetry in stratification in the ebb tide [23]. Scully and Friedrichs also observed that the shoal was generally less stratified than the channel. The biggest lateral stratification occurred in the spring tide because the higher tidal energetics broke down the stratification in the shoal in the spring tide. Chapter 2 will look in detail at how lateral exchanges between channel and shoal affects the observed tidal stratification pattern in Lower South San Francisco Bay.

1.3 Stratification

The rate of change of stratification can be described mathematically by taking the vertical derivative of the advection-diffusion equation for salt. Due to the aspect ratio of the flow, it is typically assumed that the vertical advection term is negligible [36] and we are left with the time variability of stratification, $\frac{\partial}{\partial t}(\frac{\partial S}{\partial z})$, longitudinal straining, $\frac{\partial u}{\partial z}\frac{\partial S}{\partial x}$, longitudinal advection of salinity gradients, $u\frac{\partial S}{\partial z \partial x}$, lateral straining , $\frac{\partial v}{\partial z}\frac{\partial S}{\partial y}$, lateral advection of salinity gradients, $v\frac{\partial S}{\partial z \partial y}$, and vertical mixing, $\frac{\partial^2}{\partial z^2}(K_Z\frac{\partial S}{\partial z})$ where S is salinity and K_Z is the vertical turbulent diffusivity.

$$\frac{\partial}{\partial t}(\frac{\partial S}{\partial z}) + \frac{\partial u}{\partial z}\frac{\partial S}{\partial x} + u\frac{\partial S}{\partial z \partial x} + \frac{\partial v}{\partial z}\frac{\partial S}{\partial y} + v\frac{\partial S}{\partial z \partial y} = \frac{\partial^2}{\partial z^2}(K_Z\frac{\partial S}{\partial z}) \tag{1.4}$$

In estuaries, the water is typically saltiest at the mouth of the estuary and freshest at its perimeters. Since estuaries are enclosed basins, salinity gradients exist in the along-

channel and across-channel directions. Lower South San Francisco Bay has a particularly strong lateral salinity gradient because of the smaller size in which the along-channel length of the estuary is around 5 miles and the width in the across-channel direction is around 3 miles. These proportions allow for significant lateral gradients that could impact the time variability of stratification in the channel.

1.4 Longitudinally Driven Tidal Straining

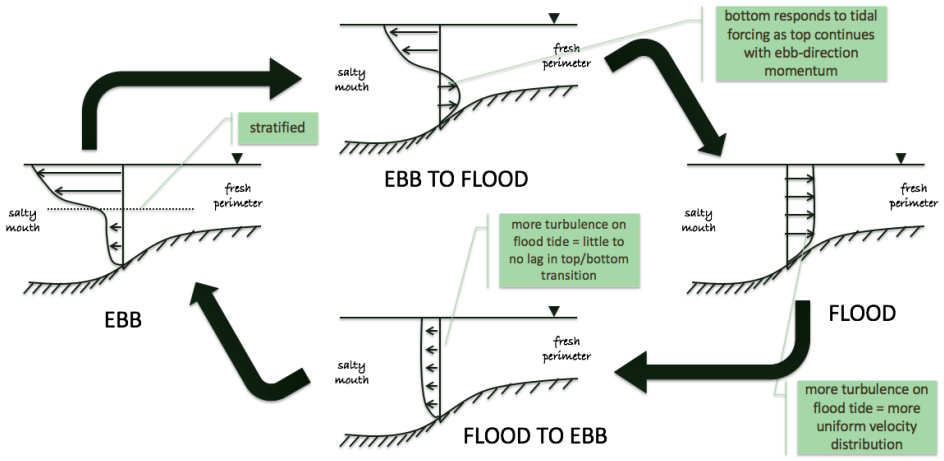

Figure 1.1: Graphic of longitudinally driven tidal straining described by Simpson (1990) [52]

The classical solution used to describe stratification tidal patterns in partially mixed estuaries was developed by Simpson in 1990 [52]. Simpson's strain-induced periodic stratification (SIPS) assumes that the longitudinal tidal straining term is the most dominant with a fixed horizontal density gradient that is spatially uniform and invariant in time. In a longitudinally strained estuary, stratification will develop during the ebb tides as vertical shear causes freshwater to overtop more dense, heavy water. When the tide reverses, more saline water will over top the water column, causing an instability which will mix out over the flood tide.

1.5 Laterally Driven Stratification

Lateral straining and advection has been getting more attention in the past few decades. As models improve and as field equipment allows for more accurate observations, lateral gradients are being studied more. In 2003, Lacy et al. looked at how the lateral density gradient interacted with lateral circulation in a location largely impacted by lateral flows. When turbulence in the channel was high, it acted as a barrier for lateral flows. Therefore, lateral salinity gradients were built up as the velocity in the channel is high. If the creation

of the lateral salinity gradient was strong enough, baroclinic forces caused lateral exchange at tide transitions [25].

In the past, lateral dynamics were largely ignored. However, recent developments have made it clear that lateral dynamics can play an important and even dominant role in the development of stratification in an estuary. Lateral effects on stratification have been observed in North San Francisco Bay [25], the Hudson River estuary [50], and the German Wadden Sea [4]. These observations were found to deviate from the traditionally assumed longitudinally driven tidal straining model developed by Simpson et al. (1990) proving the three-dimensionality of estuarine systems and thus highlighting the importance of understanding lateral transport processes [52].

1.6 Stratification and Turbulent Mixing

Stratification asymmetry also causes tidal asymmetry in turbulent mixing. The last term in the stratification equation (1.4) is the vertical mixing term. The turbulence term in the stratification equation almost always homogenizes the water column, breaking down stratification. Past research has provided significant turbulent observations in North San Francisco Bay [53, 54], the Hudson River estuary [36, 20], the Columbia River estuary [24], and the Chesapeake Bay [49]. Observations prove stratification stifles vertical turbulent mixing. When stratification is present, turbulence is confined to the bottom mixed layer [54]. The presence of stratification suppresses the turbulent length scale and limits turbulence to the bottom layer [20]. The stratification asymmetry between flood and ebb tides poses a challenge for turbulence modeling. Both stratification and shear must be correctly simulated on the tidal timescale in order to correctly model the turbulence asymmetry [53].

In literature, there has been a focus on how stratification, mixing, and shear effects each other. Observations in the lower Hudson River estuary found significant tidal asymmetry in measured eddy viscosity [20]. During the flood tide, the eddy viscosity was twice as large in magnitude than in the ebb tide when there was only a slight difference between spring and neap tides. The interaction between stratification and turbulent mixing is important to understand to get a full picture of the hydrodynamics in any given estuary. In North San Francisco Bay, turbulence observations have been collected to determine how the horizontal Richardson's number, Ri_x, can be used to predict the onset of stratification [34, 54, 53]. Stacey suggests the pulse-like pattern of exchange flow in North San Francisco Bay is created by barotropic forcing and variable stratification can be described by longitudinally-driven tidal straining. When the water column in the channel is stratified, mixing is low, these conditions allow longer lasting exchange flows during the weak ebb tide. During the strong ebb tide, the exchange flow did not develop and Stacey suggests this is because the turbulent mixing is large enough to prevent the development of exchange flows. While turbulence is not directly measured in this dissertation, these concepts are used to interpret the data and patterns throughout all chapters.

1.7 Stratification and Shear

Lastly, stratification and mixing also impact the vertical shear in the water column. Stratification can increase shear because in a stratified water column, the top layer is protected from the turbulence generated at the sea floor. Shear can either create or destroy stratification depending on the salinity gradient that the shear is pulling.

If an estuary were longitudinally driven, there would be a creation of stratification over the ebb tide which would create a larger shear. Jay and Smith (1990) found that during the ebb tide during periods of weak to moderate stratification, there was generally more shear than in the flood tide reinforcing the idea that stratification increases shear [24].

Monthly tidal observations in the Columbia River estuary showed that the vertical velocity had a phase difference at the end of the flood and ebb tide due to the combination of barotropic and baroclinic forcings working together on the flood tide and in opposition in the ebb tide [24]. During the flood tide, barotropic and baroclinic forcings are working in the same direction. When an estuary is primarily longitudinally driven, there is a creation of instability during the flood tide which increases mixing. Due to these factors, we expect a more uniform velocity profile during the flood tide and a more sheared velocity profile in the ebb tide.

To understand the affects of seasonal variation on the hydrodynamics of Lower South San Francisco Bay, salinity, temperature, and velocity observations were collected from September 2015 - February 2017. The original plan was to assume the estuary was longitudinally driven, but after diving into literature and initial looks at field observations in early deployments, it became clear that a three-dimensional mesh of equipment was necessary to understand how both longitudinal and lateral dynamics affected stratification in Lower South San Francisco Bay. The final deployment had 6 lines arrayed in a longitudinal, lateral, and vertical mesh.

This dissertation applies concepts from estuarine literature to a unique data set in attempt to understand present tidal hydrodynamic conditions in Lower South San Francisco Bay (chapter 2), estimate the residence time (chapters 3 and 4), estimate the longitudinal dispersion rate (chapter 4), and determine the estuary's response to seasonal variation (chapter 4).

Chapter 2

Longitudinal versus Lateral Estuarine Dynamics and Their Role in Tidal Stratification Patterns in Lower South San Francisco Bay

Abstract

The dynamics of shoal-channel estuaries require consideration of lateral gradients and transport, which can create significant intratidal variability in stratification and circulation. When the shoal-channel system is strongly coupled by tidal exchange with mudflats, marshes or other habitats, the gradients driving intratidal stratification variations are expected to intensify. To examine this dynamic, hydrodynamic data was collected from January 27, 2017 - February 10, 2017 in Lower South San Francisco Bay, a small subembayment fringed by extensive shallow vegetated habitats. During this deployment, salinity variations were captured through instrumentation of 6 stations (arrayed longitudinally and laterally) allowing for mechanisms of stratification creation and destruction to be calculated directly and compared with observed time variability of stratification at the central station. We present observation-based calculations of longitudinal straining, longitudinal advection, lateral straining, and lateral advection. The time dependence of stratification was observed directly and calculated by summing measured longitudinal and lateral mechanisms.

We found that the stratification dynamics switch between being longitudinally dominated during the middle of ebb and flood tides to being laterally dominated during the tidal transitions. This variability is driven by the interplay between tidally-variable lateral density gradients and turbulent mixing. Relatively constant along-estuary density gradients are differentially advected during flood and ebb tides, resulting in maximal lateral density gradients around tidal transitions. Simultaneous decrease in turbulent mixing at slack tides allows lateral density-driven exchange to stratify the estuary channel at the slack after flood.

At the end of ebb, barotropic forcing drives negatively buoyant shoal waters towards the channel.

2.1 Introduction

The dynamics of estuaries are governed by the interaction of freshwater buoyancy inputs, tides, and turbulent mixing produced by the tidal forcing [19]. The balance between these processes establish the strength and variability of vertical mixing, stratification, lateral circulation and transport. Each of these physical components influences the estuarine ecosystem, by defining vertical and lateral fluxes that exchange phytoplankton, oxygen, and nutrients between pelagic and near-benthic regions [29]. When the shoal-channel system is bounded by shallow vegetated perimeter habitats, both physical and biological variability in the system may be enhanced by the proximity of habitat variations.

Starting with Simpson (1990), the estuarine community has established the importance of longitudinal straining to the creation and destruction of stratification and estuarine circulation [24, 36, 20, 50]. Longitudinal gradients of salinity, usually created by buoyancy inputs from specific freshwater sources, but also potentially from direct precipitation into perimeter habitats and evaporation, are established and maintained to become key physical drivers for local longitudinal circulation. The buoyant forcing in estuaries works to create stratification and is opposed by turbulent mixing which works to homogenize the water column. Simpson's goal was to create a simple model that predicted the onset and break down of stratification for regions with significant freshwater input. A simple longitudinal balance to describe the competition between straining and mixing can be framed as:

$$\frac{\partial}{\partial t}\frac{\partial S}{\partial z} + \underbrace{\boxed{\frac{\partial u}{\partial z}\frac{\partial S}{\partial x}}}_{\text{Longitudinal Straining}} = \underbrace{\boxed{\frac{\partial}{\partial z}K(\frac{\partial^2 S}{\partial z^2})}}_{\text{Turbulent Mixing}} \tag{2.1}$$

During the ebb tide, if longitudinal gradients are sufficiently strong, straining overcomes turbulent mixing to create stable stratification. Any stratification that exists at the end of the ebb tide is gradually eliminated by the reversed straining during the flood tide, potentially leading to unstratified conditions and "over-straining" to produce convective instabilities [36]. The strain induced periodic stratification (SIPS) is asymmetric between ebb and flood tides due to the contribution of turbulent mixing (right side of (1)), which is always acting to reduce stratification. This asymmetry in stratification also feeds back into the turbulence and strengthens the ebb-flood asymmetry in mixing, with a more constrained near-bottom turbulent boundary layer on ebbs and more energetic and extensive mixing on the floods.

A scaling of this competition between straining and mixing, which determines the degree to which periodic stratification can develop, results in the Simpson number:

$$Si = \frac{g\beta\frac{\partial S}{\partial x}H^2}{u_*^2} \tag{2.2}$$

where β is the coefficient of saline contractivity, H represents the local depth, and u_* is a friction velocity based on tidal flows and forcing. For small values of Si, the longitudinal density gradient is not strong enough to overcome turbulent mixing and the water column remains unstratified throughout the tidal cycle; as Si increases, conditions will transition to periodic, and eventually persistent, stratification of increasing magnitude.

The role of longitudinal straining in setting estuarine stratification and circulation is now widely established, but recent work has expanded consideration to the role of lateral dynamics in defining estuarine stratification. Lateral effects on stratification have been observed on a tidal time scale in North San Francisco Bay [25], the Hudson River estuary [50], and the German Wadden Sea [4]. These observations were found to deviate from the traditionally assumed longitudinally driven tidal straining model developed by Simpson et al. 1990 proving the three-dimensionality of estuarine systems and thus highlighting the importance of understanding lateral transport processes [52]. Observations in Northern San Francisco Bay found deviations in stratification patterns from the classically explained longitudinally-strained SIPS conditions occurred during low tidal energy periods when the tide transitioned. During tidal phases with the largest tidal velocities in the channel, turbulence created a barrier preventing lateral exchanges between the shoal and the channel [25]. When the turbulence decreased, lateral exchange was able to form, driven by baroclinic forcing.

The lateral velocity, v, is typically an order of magnitude smaller than the longitudinal velocity, u [26], and was therefore frequently neglected in analysis of estuarine stratification dynamics. However, if the lateral salinity gradient is large, lateral straining could become a significant contributor to the tidal pattern of stratification.

$$\frac{\partial}{\partial t}\frac{\partial S}{\partial z} + \underbrace{\boxed{\frac{\partial u}{\partial z}\frac{\partial S}{\partial x}}}_{\text{Longitudinal Straining}} + \underbrace{\boxed{\frac{\partial v}{\partial z}\frac{\partial S}{\partial y}}}_{\text{Lateral Straining}} = \underbrace{\boxed{\frac{\partial}{\partial z}K(\frac{\partial^2 S}{\partial z^2})}}_{\text{Turbulent Mixing}} \tag{2.3}$$

Dynamically, we consider the structure and magnitude of the lateral density-driven flow based on a balance between the baroclinic pressure gradient and the vertical stress divergence, parameterized with a constant vertical viscosity. Including a constraint of mass conservation, and an associated compensating barotropic pressure gradient, this balance results in a bi-directional lateral velocity profile described by the following equation:

$$v(z) = \frac{1}{\nu_T} g\beta \frac{\partial S}{\partial y}(\frac{Hz^2}{2} - \frac{z^3}{6} + constant) \tag{2.4}$$

where v is the lateral velocity at a given depth, z, ν_T is the turbulent viscosity that is scaled with the tidal velocity, g is the acceleration due to gravity, and y is in the lateral, cross-channel direction. As shown (4), when the turbulent viscosity is large, it inhibits the development of lateral exchange [25]. Therefore, lateral exchange is more likely to occur at the transition periods between the tides when the tidal velocity and turbulent mixing are at a minimum.

Lateral density gradients that drive lateral circulation could be created by direct perimeter inputs of freshwater or by differential advection of the longitudinal salinity gradient. Considering a single tidal component, the depth-averaged (tidal) velocity in the channel and shoal can be represented as:

$$u_{channel} = A\sin(\omega t),\ u_{shoal} = a\sin(\omega t + \phi) \tag{2.5}$$

where A is the amplitude of the tidal velocity in the channel, a is the amplitude of the tidal velocity in the shoal and, based on the depth-difference, $A > a$ [23, 26]. To leading order, the tidal variability of depth-averaged salinity at a location is set by tidal advection of the longitudinal salinity gradient ($\frac{\partial S}{\partial t} = -u\frac{\partial S}{\partial x}$) such that we arrive at the following expression for the time variability of the lateral salinity gradient:

$$\frac{\partial S}{\partial y} = \frac{S_{shoal} - S_{channel}}{L_y} = \frac{\partial S}{\partial x}\frac{1}{\omega L_y} cos(\omega t)(a - A) \tag{2.6}$$

where L_y is a representative lateral distance (width of the transition between channel and shoal).

The lateral shear in the longitudinal velocity causes lateral density gradients to be created over both the ebb and flood tides, but with opposite signs on each tidal phase. By the end of the ebb tide, the lateral shear in the longitudinal velocity results in a lateral density gradient in which the shoal density is greater than the density in the channel. During the flood tide, the reverse density gradient is created in which the shoals are fresher than the channel. This sets up a lateral density gradient that can drive a baroclinic lateral exchange [26]. The goal of this paper is to determine the role of longitudinal and lateral dynamics in regulating vertical stratification dynamics in Lower South San Francisco Bay, a partially stratified estuary which has significant lateral density gradients. With observations of salinity gradients in the lateral and longitudinal direction, we will decompose tidal variability of the physical dynamics that creates and destroys stratification.

2.2 Methods

Site Description

San Francisco Bay is a meso-tidal estuary characterized by strong diurnal inequalities that vary with the spring-neap cycle. This paper focuses on a sub-estuary of San Francisco Bay, Lower South San Francisco Bay, which extends roughly 10 km landward from the Dumbarton Narrows to the head of the estuary in Coyote Creek. Figure 2.1 shows how the bathymetry consists of a central channel with broad shoals on either side extending to perimeter marshes that are connected to the Bay through tidal sloughs. Freshwater from rainfall is typically observed from November to April with little to no rainfall inputs from May to October.

Observations were collected in Lower South San Francisco Bay (LSSFB) in order to observe how stratification is created or destroyed in an estuary that is strongly coupled with

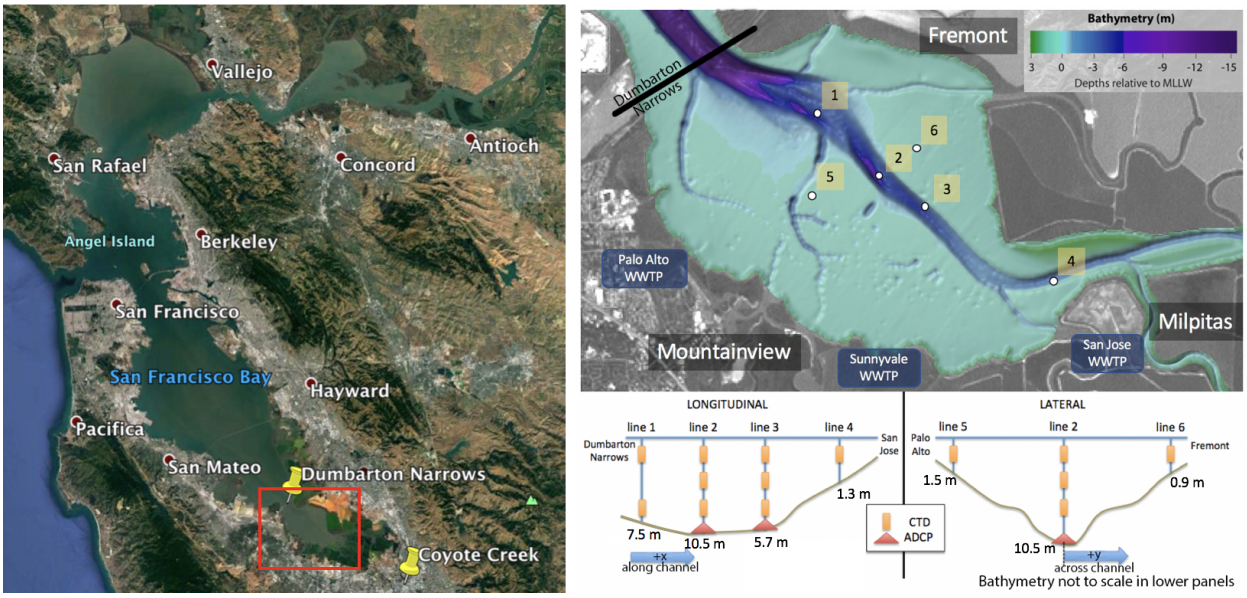

Figure 2.1: Bathymetry in Lower South San Francisco Bay consisting of a deeper, center channel in the Northwest to Southeast direction with broad, shallow shoals. White dots show where lines of CTD and ADCPs were placed for field deployment. Shades of purple correspond to -15 m MLLW, dark blue -6 m MLLW, light blue 0 m MLLW, and green 3 m MLLW. Positive x is defined in the southeast direction. Positive y is defined in the northeast direction. Line 2 is centrally located and lies at $y = 0$. See more details on mooring water depths in Table 2.1. Bathymetry from 2005 Hydrographic Survey of South San Francisco Bay, California [16]

marsh habitats around its perimeter. Lower South San Francisco Bay sits within the urbanized and densely populated San Francisco Bay Area, and most of the freshwater flow into LSSFB is from wastewater returns, which bring with them high nutrient concentrations. Risks to future ecosystem conditions, and the role that nutrients may play in limiting or facilitating a transition to eutrophic conditions, have motivated a reconsideration of the dynamics of stratification in LSSFB. Recent evidence of decreasing turbidity reinforces concerns about threshold-like transitions in the system, particularly if stratification were to increase in strength or duration under future climate forcing [11, 47]. The proximity of these shallow perimeter habitats to the central channel emphasizes the importance of both lateral and longitudinal gradients in velocity and salinity. The bathymetry of the embayment, and the structure of the perimeter habitats, means the embayment has a tidal excursion on the same order of magnitude as the length of the estuary so that the center of the estuary will experience an influence from the perimeter within each tidal cycle, as well as from the Dumbarton Narrows to the north, which serves as the "mouth" for this sub-estuary.

			Average Depth Below Surface [m]			NAVD88	Water Depth
Line	Latitude	Longitude	Top CTD	Middle CTD	Bottom CTD	[m]	[m]
1	37.48775	-122.08939	2.4	-	7.3	-6.52	7.50
2	37.47754	-122.07643	2.7	6.7	9.8	-9.48	10.46
3	37.472	-122.06679	1.0	4.1	6.0	-4.68	5.66
4	37.45979	-122.03996	0.5	-	-	-0.35	1.33
5	37.47415	-122.09045	1.0	-	-	-0.47	1.45
6	37.48185	-122.06825	0.6	-	-	0.12	0.86

Table 2.1: Mooring detailed locations and water depths. Each CTD measures depth below the water surface. Here we display the average depth that the CTDs measured throughout the deployment. The column labeled NAVD88 provides the referenced depths from a Lower South Bay bathymetry dataset collected by the San Francisco Estuary Institute (SFEI) available on their ERDDAP website. The water depth at each mooring is estimated by taking the difference of the MSL at Alameda (0.98 m from NOAA Tides and Currents [38]) from the NAVD88 bathymetry.

Equipment Deployed

In order to measure salinity gradients in the longitudinal, lateral, and vertical directions, a mesh of nine Ruskin RBR XR-420 CTDs and two Seabird SBE-37's were placed in various positions in all three dimensions. Locations of the lines are shown in Figure 2.1. Lines 1, 2, 3, and 4 were placed in the channel. Lines 5 and 6 were placed in the shallows, lateral to line 2. Line 1 has two CTD's attached at the top and bottom of the water column. Lines 2 and 3 have a top, middle, and bottom CTD. Line 4 has one CTD located near the surface of the water column. Lines 5 and 6 each have a Seabird attached at the surface of the water column. The RBRs and Seabirds measured conductivity, pressure (depth), and temperature, and calculated salinity, at one minute intervals. The RBR XR-420 CTDs (Seabird SBE 37s) have a temperature accuracy of $\pm 0.002°C$ ($\pm 0.002°C$) and pressure accuracy of 0.05% (0.1%) [45, 48].

Two Teledyne RD Instruments (RDI) 1200 kHz Workhorse Monitor Acoustic Doppler Current Profilers (ADCP) were deployed at locations 2 and 3, and were tethered to the CTD lines by a bottom cable. The moored ADCPs were programmed to measure over a 12 meter water column with a vertical resolution of 0.25 meters with the first bin located 0.81 meters from the sea floor. The ADCPs, like the RBRs and Seabirds, collect ensemble averages every minute.

2.3 Overview of Conditions

Salinity and Stratification

Line 2 is the central line containing a top, middle, bottom CTD along with a moored ADCP. The deployment was slightly northeast of the center of the channel placing it closer to the

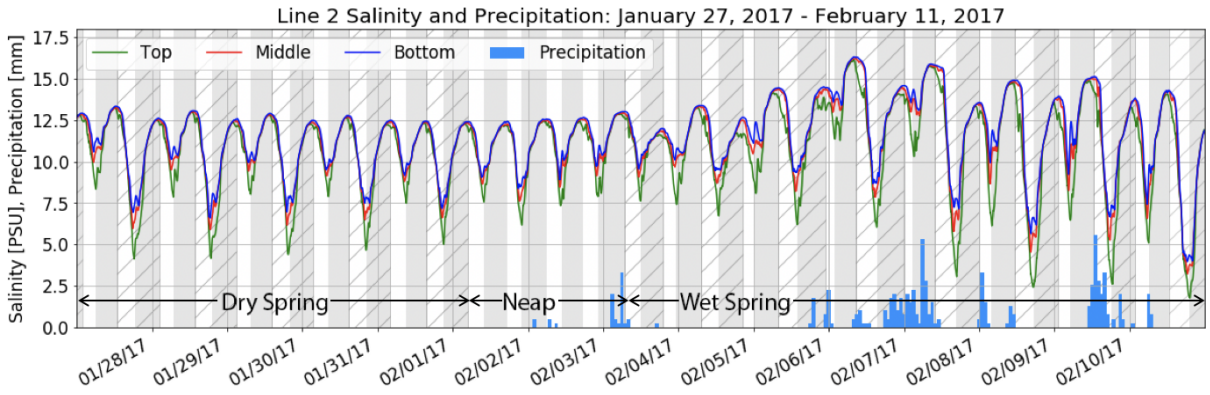

Figure 2.2: Salinity [PSU] and precipitation [mm] plot. Precipitation data from the California Irrigation Management Information System (CIMIS) station in Union City [58]. Note: Flood tides correspond to gray shading. Ebb tides correspond to white shading. Hatching refers to larger flood/ebb tides when there is a diurnal asymmetry. See Figure 2.6 for the longitudinal velocity time series clarifying shading and hatching periods.

east shoal, but protected from ship and fishing traffic.

Figure 2.2 displays the salinity measured from the top, middle, and bottom CTDs. The depth-averaged longitudinal velocity data from ADCP measurements were used to determine the start and end of each flood and ebb tide along with diurnal tidal asymmetries shown by hatching. Hatched regions are larger flood-ebb tides when the diurnal inequality is significant. Gray shaded regions are flood tides and white shaded regions are ebb tides. The precipitation in millimeters is shown at the bottom of Figure 2.2. Precipitation data was collected and distributed online by the California Irrigation Management Information System (CIMIS) [58]. There is no variation in temperature in the water column, and there is minimal temperature variation over the time frame of the deployment. As a result, and in addition because of the smaller relative effect of temperature compared to salinity, density dependence on temperature is weaker than the dependence on salinity. The closest station to Lower South San Francisco Bay is located in Union City which is located about 13 kilometers from Line 2. There are three distinct conditions captured in the deployment. The first window, from January 27, 2017 to February 1, 2017 is a tidally energetic spring tide with distinct diurnal tidal asymmetry and limited precipitation. From February 1-3, 2017 is a neap tide with no tidal asymmetry and little to no precipitation. Finally, the last window from February 3-11, 2017 is another spring tide but with a series of significant precipitation events. Throughout the entire record, the typical tidal advective pattern is evident, with the water column freshening on ebbs and becoming more saline on floods. The range of salinity seen in a tidal cycle is roughly proportional to the magnitude of velocity in a particular tidal phase, which suggests that the dominant factor in the bulk variation of salinity is longitudinal tidal advection (Figure 2.2, 2.4a).

The vertical stratification of salinity (Figure 2.3) has more complex tidal variability. In

Figure 2.3 we see stratification beginning to develop before the tidal transition from ebb to flood, which is consistent with SIPS [52, 24, 36, 20, 50]. As a result, when the tide begins to turn at the end of the ebb tide, the water column is stratified, creating a vertical time lag in the reversal of the tidal flows. This results in strong water column shear during the transition from ebb to flood that causes the stratification to continue to intensify during this period. While this dynamic is, in general terms, consistent with dominance by longitudinal straining, the details of the intra-tidal variability of stratification show much more structure and variability than would be expected purely from SIPS. Specifically, stratification events associated with each slack tide are evident throughout most of the study period. At the end of each flood tide, the surface (top sensor) salinity drops, creating a short period of stratification (Figures 2.2 and 2.3). At the end of each ebb tide and into the beginning of the flood tide, there is another disruption in the typical longitudinally driven salinity pattern, this one is characterized by an increase in the salinities at all sensors, but with a time lag at the surface relative to the other sensors (Figure 2.2). The magnitude of this salinity feature ranges between 0.5 and 2 PSU. This salinity increase is too abrupt and tied to slack phasing to be longitudinal advection.

There is no asymmetry in the amplitude of the two flood and ebb tides in a given day during the neap tide that occurs around February 1-3, 2017 (Figure 2.6), but the longitudinal salinity gradient remains roughly constant relative to the first spring tide (Figure 2.4). The result is that the minimum salinities within each tidal cycle are different during the neap (6-8 PSU) and the springs (large ebb: 4-6 PSU, small ebb: 8-10 PSU). Nonetheless, the variation of stratification around the slack tides remains qualitatively similar to the first spring tide period: there is still a sudden drop in the top salinity at the end of the flood tide and an increase in the top, middle, and bottom salinities at the end of each ebb tide. During the second spring tide (February 3-11, 2017), precipitation and runoff creates increased salinity variability, although many of the same features that were evident in the stratification during the early parts of the dataset persist. In particular during this period, the top salinity deviates even more from the middle and bottom salinities at the end of the flood tide and into the beginning of the ebb tide.

SIPS based on longitudinal straining predicts the largest stratification at the end of the ebb tide and well-mixed conditions at the end of the flood tide. In Figure 2.3 the general pattern of stratification shares many features with this basic pattern, with well-mixed conditions developing from mid to late flood, and stratification generally increasing through the ebb tides. The larger ebb tides tend to create stronger stratification events in the first weeks shown in Figure 2.3b, but this pattern is not as consistent in the latter part of the data set when there is higher buoyancy input to the system (Figure 2.3c). During most flood tides there is a total break down of the stratification that was developed over the ebb tide. There are a few instances in Figure 2.3c in which stratification is not eliminated during the flood tide creating stratified water columns that persists over one or two days (i.e. February 6, 18:00 and February 8, 9:00). Further, the development of stratification initiates slightly earlier than traditional SIPS would predict, with stable conditions beginning to develop before the turn of the tide. Finally, we note that, in general terms, flood-ebb asymmetry of turbulent

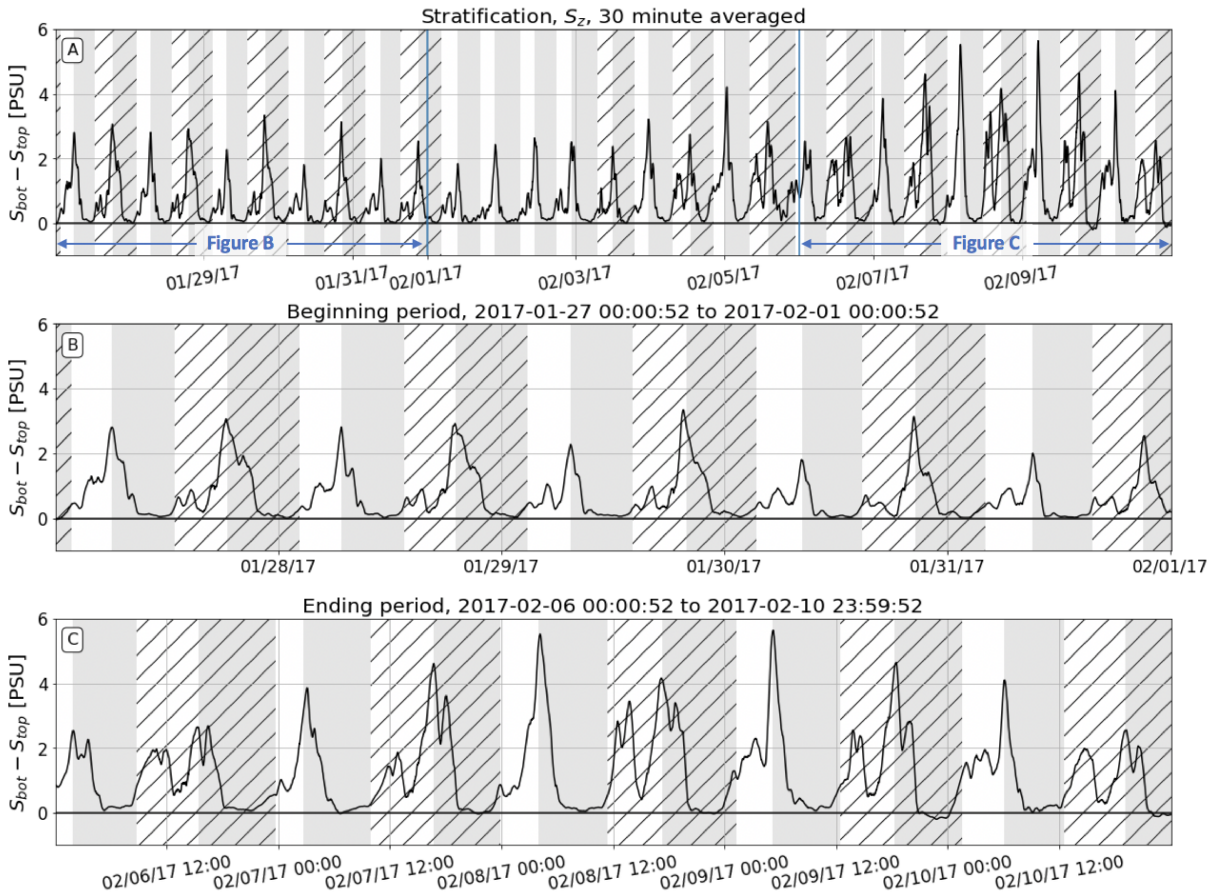

Figure 2.3: Stratification (S_z) shown in units of PSU, is calculated by taking the difference in measured salinities in the bottom and top CTDs on line 2. Note: Flood tides correspond to gray shading. Ebb tides correspond to white shading. Hatching refers to larger flood/ebb tides when there is a diurnal asymmetry.

mixing accelerates destratification early in the flood tide leading to, on average, less stratified flood tides than ebb tides consistent with what's been seen in estuarine literature such as *Scully and Geyer*, 2012, *Geyer et al.*, 2000, *Nepf and Geyer*, 1996 [50, 20, 36]. Additionally, the influence of turbulent mixing is evident during the peak ebb tides, particularly during the wet period at the end of the record (Figure 2.3c), where stratification decreases during the mid-ebb, indicating that turbulent mixing is able to overcome the stabilizing influence of longitudinal straining.

In contrast to traditional SIPS dynamics, during both the dry spring tide and the wet spring tide, stratification begins to develop at the end of the flood tide and continues to grow over the ebb tide. We can also see that the destruction of stratification over the flood tide is not gradual like we would expect if it were longitudinally-driven. The destratification process occurs in two or three separate instances at the beginning of the flood tide and then

the water column is completely destratified by mid-flood. This complexity associated with the turning of the tide from ebb to flood and from flood to ebb suggests higher-dimensional processes than is described by longitudinal SIPS. In order to determine what is driving these features, we must break down how longitudinal advection, longitudinal straining, lateral advection, and lateral straining contribute on the tidal timescale.

Salinity Gradients

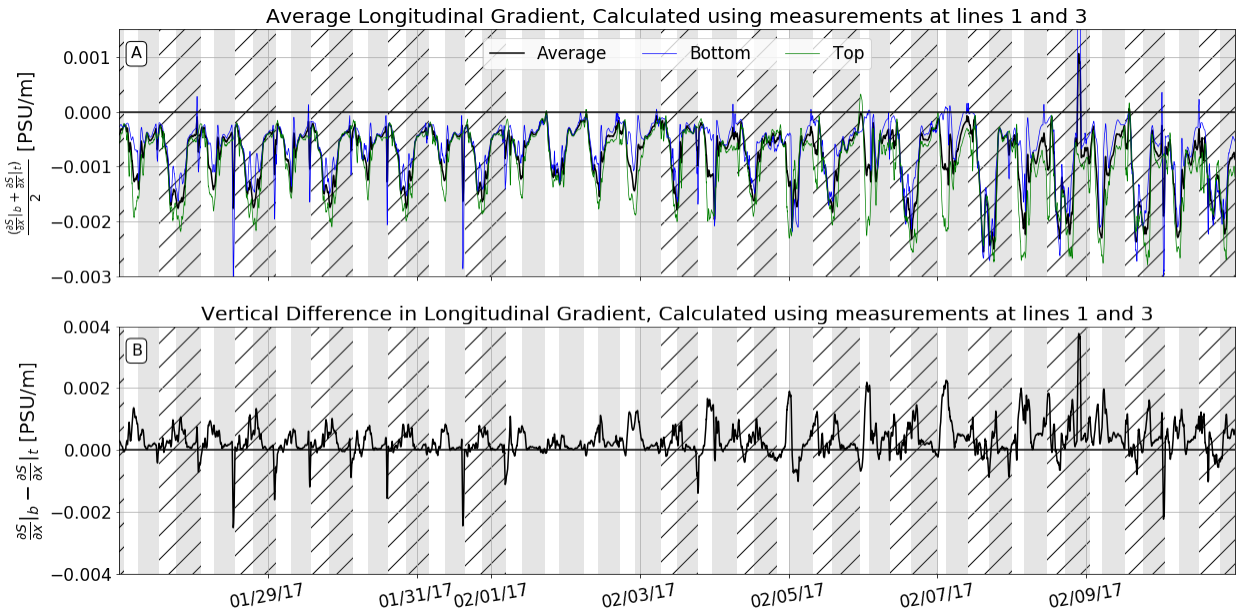

Figure 2.4: Longitudinal salinity Gradient [PSU/m] calculated using instantaneous salinity measurements at lines 1 and 3. Top plot shows the average longitudinal salinity gradient and the bottom plot shows the vertical difference. Note: Flood tides correspond to gray shading. Ebb tides correspond to white shading. Hatching refers to larger flood/ebb tides when there is a diurnal asymmetry.

To define the longitudinal salinity gradient at our central station (line 2), differences between lines 1 and 3 were used. Both lines 1 and 3 also have a top and bottom CTD which allows for comparing longitudinal salinity gradients at the top and at the bottom. x is defined as positive up-estuary (to the southeast), therefore, the longitudinal salinity gradient, $\frac{\partial S}{\partial x}$, is expected to be negative. Figure 2.4a shows that, although the longitudinal salinity gradient is consistently negative throughout the tidal cycle, it becomes more negative during the ebb tide. This tidal variation of $\frac{\partial S}{\partial x}$ indicates the presence of a non-linear salinity gradient, with stronger gradients that develop near the perimeter being advected into our observation site during the ebb tides. The largest magnitude of the longitudinal stratification gradient occurs at the end of the ebb tide and decreases through the flood tide as the influence of the

Dumbarton Narrows is advected into the study site (Figure 2.4b). During the neap tide, the observed longitudinal gradient in stratification reaches zero at the end of the flood tide. The influence of a zero longitudinal stratification gradient shows up in the longitudinal advection term in the dynamic stratification equation indicating the advection of an unstratified water mass from north of the Dumbarton Narrows to the location of line 2. Since the longitudinal stratification gradient decreases in magnitude on flood tides, we hypothesize that higher velocities through the constriction at the Narrows creates turbulent mixing and destratifies the water column that is inputted into the estuary from the mouth. The unstratified water at the Narrows is then advected upstream on the flood tides.

There are a few unexpected signals in the tidal signal of the longitudinal gradient at the end of the ebb tide and at the end of the flood tide. At the end of each ebb tide there is a decrease in the magnitude of the longitudinal gradient that persists for only an hour or two and appears to be due to a pulse of saline waters evident at the middle and bottom up-estuary CTDs that is not shown in the down-estuary CTDs causing the salinities in the two locations to converge at the end of the ebb tide. This could be explained by lateral circulation bringing saltier water to the bottom of the up-estuary location at the end of the ebb or the longitudinal advection of a salt wedge. At the end of the flood tide, we see a large, sudden increase in the magnitude of the average longitudinal gradient. This is due to a pulse of freshwater at the up-estuary station, creating the increase in the longitudinal salinity gradient.

The vertical variation of longitudinal stratification ($\frac{\partial^2 S}{\partial z \partial x}$, Figure 2.4b) tends to be positive, indicating stronger stratification up-estuary. The advection of this gradient is responsible, in part, for the observed tidal variation of stratification, and is strongly shaped by specific features of the embayment. During the ebb tide, $\frac{\partial S}{\partial z}$ increases as a stratified water mass from up-estuary is advected into our observation site (Figure 2.3). On floods, mixing at the Dumbarton Narrows likely homogenizes the water column, so that during the flood tide, increasingly destratified conditions are advected into the study site. This dynamic is intensified during the last half of the observation period, as buoyancy input (precipitation and runoff) intensifies the density gradients, but not sufficient to overcome the flood tide mixing.

The lateral salinity gradient was calculated using salinity measurements at line 2 and line 6. This pattern at line 5 was similar to that at line 6, but consistently weaker. Due to the timing of the deployment with the water level, we were unable to get line 5 closer to the perimeter. If we were able to get line 5 closer to the western perimeter, we would have a stronger lateral salinity gradient measurement between lines 2 and 5. For clarity, we only use the lateral salinity gradient that is measured between lines 2 and 6. Line 6 only has one top salinity measurement, so it was necessary to assume there is no stratification in the shoals [49]. Figure 2.5 shows the measured lateral salinity gradient, $\frac{\partial S}{\partial y}$, using only the top salinity measurements at lines 2 and 6 (dashed) and then by using a depth-averaged salinity at line 2 and the salinity measurement at line 6 (solid line). The average lateral gradient is negative most of the time, indicating that the shoals are persistently fresher than

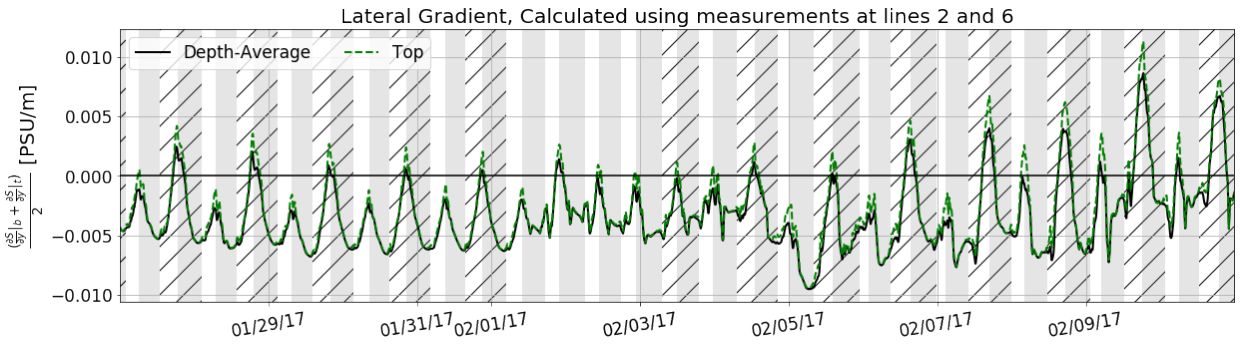

Figure 2.5: The lateral salinity gradient [PSU/m] was calculated using instantaneous salinity measurements at lines 2 and 6. The average lateral salinity gradient was calculated using the top and bottom salinity measurements at line 2 and the top salinity measurement at line 6. Due to limitations in field measurements it is assumed that the water in the shoal is well-mixed at line 6 allowing us to use the top salinity measurement for the entire water column. The top lateral salinity gradient (dashed) is calculated by using only the measurements at the top of lines 2 and 6 which reveals a reversal sign by the end of the ebb tide meaning the shoal is saltier than the channel through differential advection.

the channel. However, at the end of many ebb tides, the gradient switches signs, meaning the shoals are more saline than the channel at these times. This tidal variability of the lateral salinity gradient is consistent with differential tidal advection, where $\frac{\partial S}{\partial t} \approx -U\frac{\partial S}{\partial x}$. Differential tidal advection tells us that the tidal reach in the channel is greater than the tidal reach in the shoal. Therefore, over the ebb tide, both the channel and the shoals are getting fresher, but the channel is getting fresher at a faster rate than the shoals. As we can see in Figure 2.5, differential advection creates a reverse gradient by the end of the ebb tide meaning the channel is fresher than the shoal.

Velocity

Velocity measurements were taken throughout the water column in 25 cm bins using a Teledyne ADCP at line 2. The velocity measurements were then rotated to fit the along-channel, longitudinal direction as u and the across-channel, lateral direction as v. The along-channel or longitudinal orientation was determined by fitting a best fit line to the scatter of measured east velocity and measured north velocity. The depth-averaged longitudinal velocity, $\bar{u}$, was then used to define the start and end of each flood and ebb tide shown in shading in each plot. The coordinate system was defined as flood in the positive x-direction and ebb in the negative x-direction; the y-direction is positive to the northeast. In order to calculate water column averaged vertical shear in velocity, the measured velocities in the top 2 meters from the water surface were averaged to get u_{top} and the bottom 2 meters of measured velocity were averaged to get u_{bottom}, and the longitudinal shear velocity was calculated as $u_{bottom} - u_{top}$.

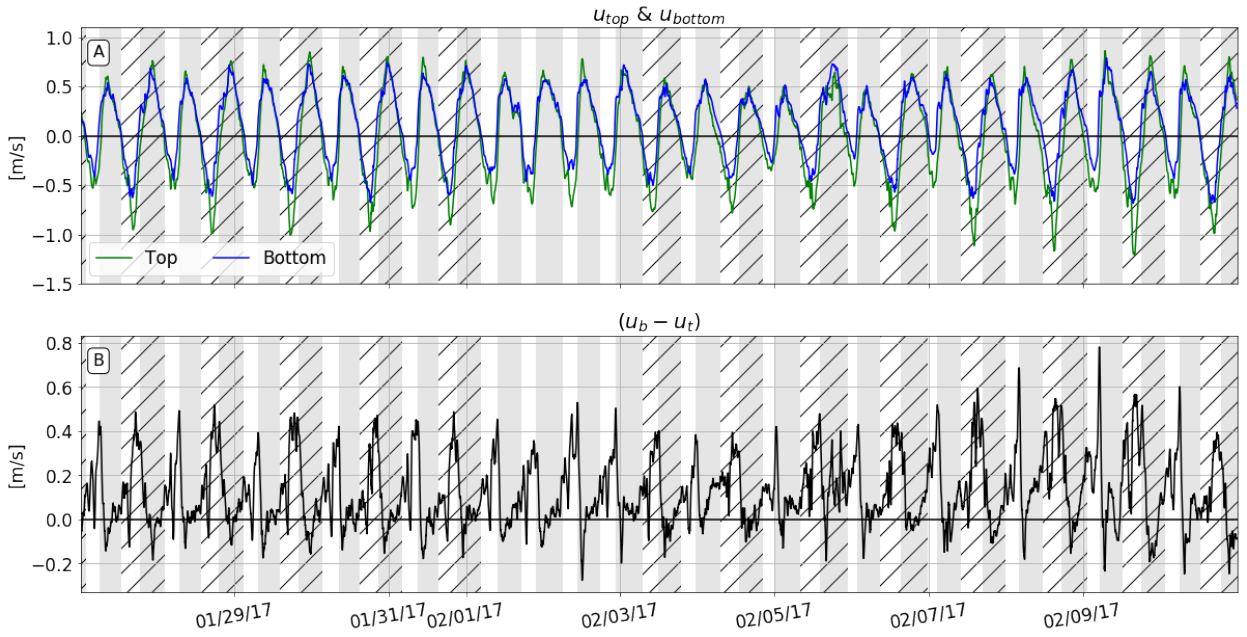

Figure 2.6: Top and bottom longitudinal velocities [m/s] were calculated by averaging the longitudinal velocities in the top 2 m and the bottom 2 m of the water column. Tidal asymmetries were defined visually by the amplitude of the top longitudinal velocity. (A) shows the time variation of top and bottom longitudinal velocity and (B) shows the shear. Note: Flood tides correspond to gray shading. Ebb tides correspond to white shading. Hatching refers to larger flood/ebb tides when there is a diurnal asymmetry.

Figure 2.6a shows the top and bottom longitudinal velocities. The tidal asymmetries are clear during the spring tides, and the larger of the diurnal tides are marked with hatching. The start and end of each tide is defined by the zero crossing of the depth-averaged longitudinal velocity. The depth-averaged shear, $u_b - u_t$, is expected to be positive on ebb tides and negative on flood tides. However, Figure 2.6b shows that the difference between the bottom and top longitudinal velocities at a given time is mostly positive for both tides. The small, slightly positive shear in the flood is due to the longitudinal salinity gradient and well-mixed conditions producing a fairly uniform velocity profile where the magnitude of the top velocity is marginally smaller than the bottom velocity.

A second mechanism that alters the expected tidal variability of water column-averaged shear is the vertical lag in the reversal of the tides during the transition from ebb to flood. In the transition from flood to ebb, the water column reverses direction together, with very little phase lag. In the transition from ebb to flood, however, the near-bed velocities reverse as much as an hour or two before the upper water column, leading to periods of inverted shear and, as a result, straining in the direction favoring stratification. Similarly, observations in the York River estuary showed that the ebb in the channel was consistently longer than the ebb in the shoal because there was more friction in the shoal which reversed the tide quicker

than in the channel where the momentum from the previous tide could continue longer [49].

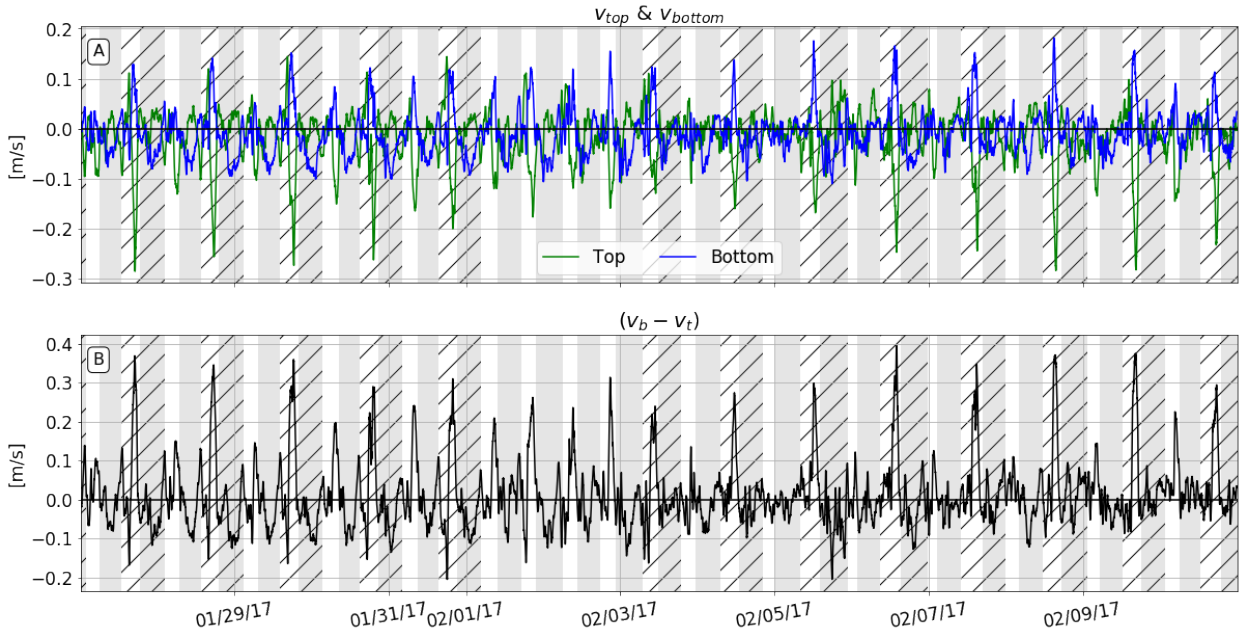

Figure 2.7: Top and bottom lateral velocities [m/s] were calculated by averaging the lateral velocities in the top 2 m and the bottom 2 m of the water column. (A) shows the time variation of top and bottom lateral velocity and (B) shows the shear. Large shear events consistently occur at the end of the ebb tide in both the spring and neap. Persistent lateral exchange, but small magnitude, occurs over the flood tide. Note: Flood tides correspond to gray shading. Ebb tides correspond to white shading. Hatching refers to larger flood/ebb tides when there is a diurnal asymmetry.

Lateral flow in a shoal-channel estuary results from barotropic (tidal) forcing, wind forcing, or baroclinic (density) forcing. Tidal variability will occur in both the barotropic (directly) and baroclinic (through differential advection as discussed above) components and we will focus on those forcing mechanisms here. The approach we took to defining the coordinate axis for the barotropic tides leaves some lateral flow due to variation in the alignment of the bathymetry with our coordinate axes. As shown in Figure 2.1, line 2 is located on the edge of a local deeper part of the channel which causes the primary axis to be at a sharper angle from the larger channel. We highlight that since line 2 lies on the northeast side of the deepest part of the channel, positive lateral velocities are flows from the channel towards the shoals and negative lateral velocities are flows from the shoals towards the channel.

The reversing sign of the lateral density gradient in Figure 2.5b suggests that the exchange between the channel and shoal should itself reverse signs tidally, with a positive near surface flow (and negative near-bottom flow) during one slack tide and the reverse during the other. Figure 2.7a confirms that there are many instances where the lateral velocity is directed in

opposite directions at the top and the bottom, between 10 and 20 cm/s. During mid-flood the bottom lateral velocity is negative, or in the southwest direction, and the top lateral velocity is smaller in magnitude, but in the positive, or northeast direction. We hypothesize that this shear represents the influence of baroclinic pressure gradients. Then at the end of each ebb tide, there is a short, but large magnitude lateral shearing event as shown by abrupt, positive peaks in Figure 2.7b.

2.4 Analysis

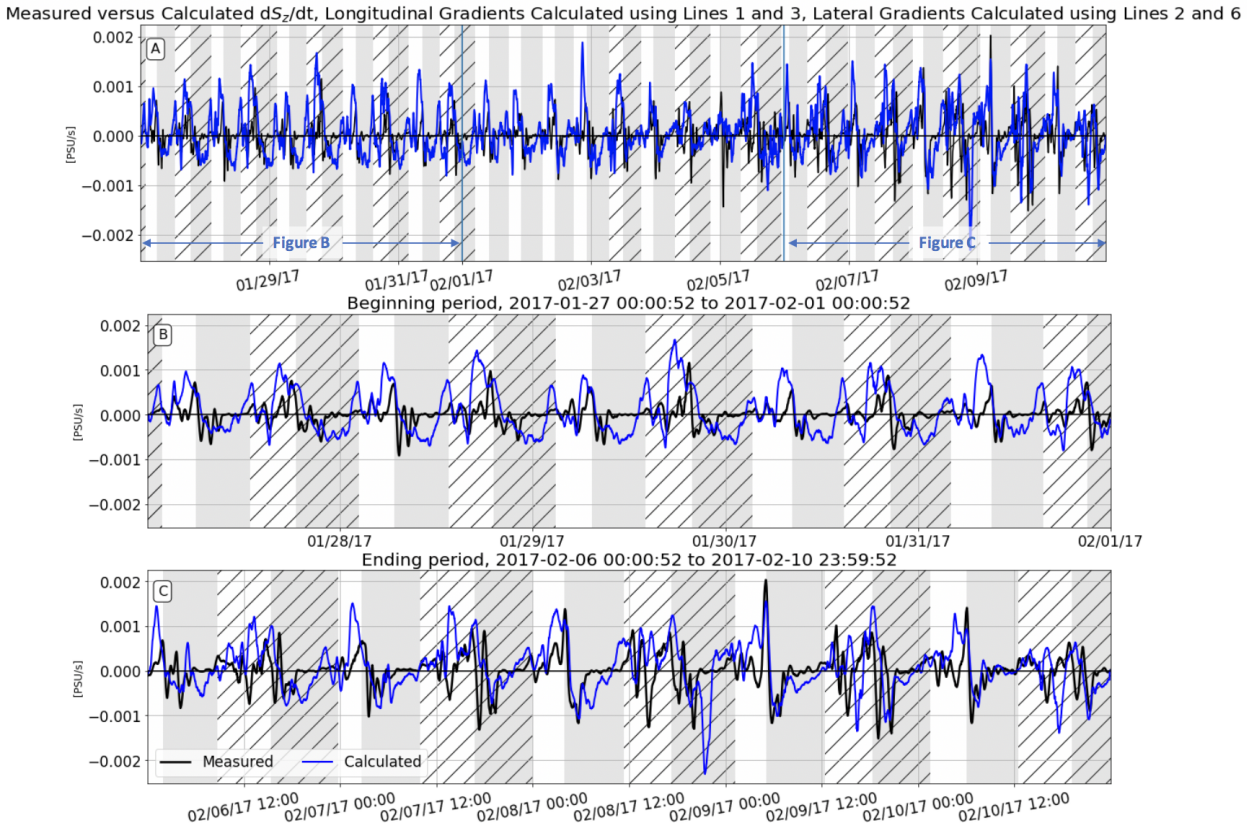

Figure 2.8: The measured rate of change of stratification (black), $\frac{\partial S_z}{\partial t}$ $[\frac{PSU}{s}]$, was calculated by taking the time derivative of the bottom-top salinity difference at line 2 and with a rolling-average window of 30 minutes. The calculated rate of stratification (blue), was calculated by taking the sum of observed values of longitudinal straining, longitudinal advection, lateral straining, and lateral advection. (A) Entire time series, (B) First, dry spring tide, (C) Second, wet spring tide. Note: Flood tides correspond to gray shading. Ebb tides correspond to white shading. Hatching refers to larger flood/ebb tides when there is a diurnal asymmetry.

We now turn to an analysis of the mechanisms responsible for the creation and destruction

of stratification. The stratification, $S_z = S_{bottom} - S_{top}$, at line 2 shows variability at tidal and spring-neap timescales, as well as in response to precipitation events (Figure 2.8). The framework we will use to evaluate changes in stratification starts with the standard Reynolds-averaged, advection-diffusion equation with constant eddy diffusivity for salt in the estuary:

$$\frac{\partial S}{\partial t} + u\frac{\partial S}{\partial x} + v\frac{\partial S}{\partial y} + w\frac{\partial S}{\partial z} = K(\frac{\partial^2 S}{\partial x^2} + \frac{\partial^2 S}{\partial y^2} + \frac{\partial^2 S}{\partial z^2}) \tag{2.7}$$

Taking the vertical derivative of this equation and rearranging, we arrive at:

$$\frac{\partial}{\partial t}\frac{\partial S}{\partial z} + \frac{\partial u}{\partial z}\frac{\partial S}{\partial x} + u\frac{\partial^2 S}{\partial z \partial x} + \frac{\partial v}{\partial z}\frac{\partial S}{\partial y} + v\frac{\partial^2 S}{\partial z \partial y} + \frac{\partial w}{\partial z}\frac{\partial S}{\partial z} + w\frac{\partial^2 S}{\partial z^2} = \frac{\partial}{\partial z}K(\frac{\partial^2 S}{\partial x^2} + \frac{\partial^2 S}{\partial y^2} + \frac{\partial^2 S}{\partial z^2}) \tag{2.8}$$

Assuming turbulent mixing in the horizontal dimensions is small compared to the vertical dimension (i.e., the depth is much smaller than the length scales associated with horizontal gradients) and that vertical advection can be neglected, equation (8) is reduced to unsteadiness, the next four terms on the left hand side and the last term on the right. Moving all of these terms to the right hand side makes for a consistent sign convention (positive means creating stratification, negative means destratifying). These five terms are:

1. Longitudinal straining, $-\frac{\partial u}{\partial z}\frac{\partial S}{\partial x}$
2. Longitudinal advection, $-u\frac{\partial^2 S}{\partial z \partial x}$
3. Lateral straining, $-\frac{\partial v}{\partial z}\frac{\partial S}{\partial y}$
4. Lateral advection, $-v\frac{\partial^2 S}{\partial z \partial y}$
5. Mixing, $K\frac{\partial^3 S}{\partial z^3}$

From the data, we can directly calculate the time variability of the stratification (first term in equation 2.8) using a central differencing scheme to approximate the time derivative of the difference between top and bottom sensors at line 2, the vertical stratification, as plotted in Figure 2.8a). In this figure, it is evident that stratification variations are strongest (largest magnitude) at the end of the ebb tide and the beginning of the flood tide. Generally, we see negative changes in stratification (destratification) in two distinct events at the beginning of the flood tide. These two peaks cause the stair-step change in stratification that was seen in Figure 2.3. Generally, the rates of change of stratification were greater during the period with precipitation (Figure 2.8c) than during dry period (Figure 2.8b), but the qualitative patterns are similar: the creation of stratification is most prominent at the end of the ebb tide, and the destruction of that stratification in two or three peaks at the beginning of the flood tide.

To evaluate the forcing mechanism responsible for changes in stratification, we approximate the vertical derivatives using a layered model and aggregate the data into near-bottom

and near-top layers. For salinity, the bottom and top sensors are assumed to represent layer averages; for the velocity data, we bin-average over the bottom or top 2 meters to define each layer. With subscripts b and t denoting the bottom and top layers, respectively, we approximate each of the terms as:

1. Longitudinal straining, $-(u_b - u_t)(\frac{\frac{\partial S}{\partial x}|_b + \frac{\partial S}{\partial x}|_t}{2})$
2. Longitudinal advection, $-\frac{u_b+u_t}{2}(\frac{\partial S}{\partial x}|_b - \frac{\partial S}{\partial x}|_t)$
3. Lateral straining, $-(v_b - v_t)(\frac{\frac{\partial S}{\partial y}|_b + \frac{\partial S}{\partial y}|_t}{2})$
4. Lateral advection, $-\frac{v_b+v_t}{2}(\frac{\partial S}{\partial y}|_b - \frac{\partial S}{\partial y}|_t)$

Longitudinal Straining

Longitudinal straining creates and destroys stratification through the straining of the longitudinal salinity gradient by a vertical velocity gradient. Tidally, this terms is expected to be positive on ebb and negative on flood, with peak values associated with peak longitudinal shear. Variations from this would be due to tidal changes in the longitudinal salinity gradient, or asymmetries in the vertical shear, which would follow from the feedback through stratification and resulting decreases in mixing.

As shown in Figure 2.9, the longitudinal straining term is generally positive, indicating a source of stratification, with some negative values (destratification) during the flood tides. This ebb-flood asymmetry in the influence of straining is due to differences in the shear ($\frac{\partial u}{\partial z}$), not the longitudinal salinity gradient (Figures 2.4 & 2.6), with the ebbs considerably more sheared than the floods. A notable feature in the longitudinal straining term is the large positive peak at the transition from ebb to flood, which is due to the vertical phase lag in the reversal of the tide [53].

In the last portion of the data set, when there is an increase in buoyancy via rainfall (Figure 2.9c), longitudinal straining continues to have the same ebb-flood pattern and asymmetry, but with a larger magnitude. The highest rate of stratification occurs from mid to late ebb, and there is a small creation of stratification at the transition into the flood tide, but the contribution of this term is small through the remainder of the flood tide.

Longitudinal Advection

The longitudinal advection term is the translation of salinity gradients in the x-direction. This term is calculated by taking the product of the depth-averaged longitudinal velocity and the second order salinity gradient in the x- and z-directions. Positive (negative) values of this term means the upstream (downstream) stratification is greater than the local or downstream (upstream) stratification. If the portions of the estuary adjacent to perimeter habitats are more stratified than the "mouth" at the Dumbarton narrows, we would expect this term to be negative on the flood tide and positive on the ebb tide.

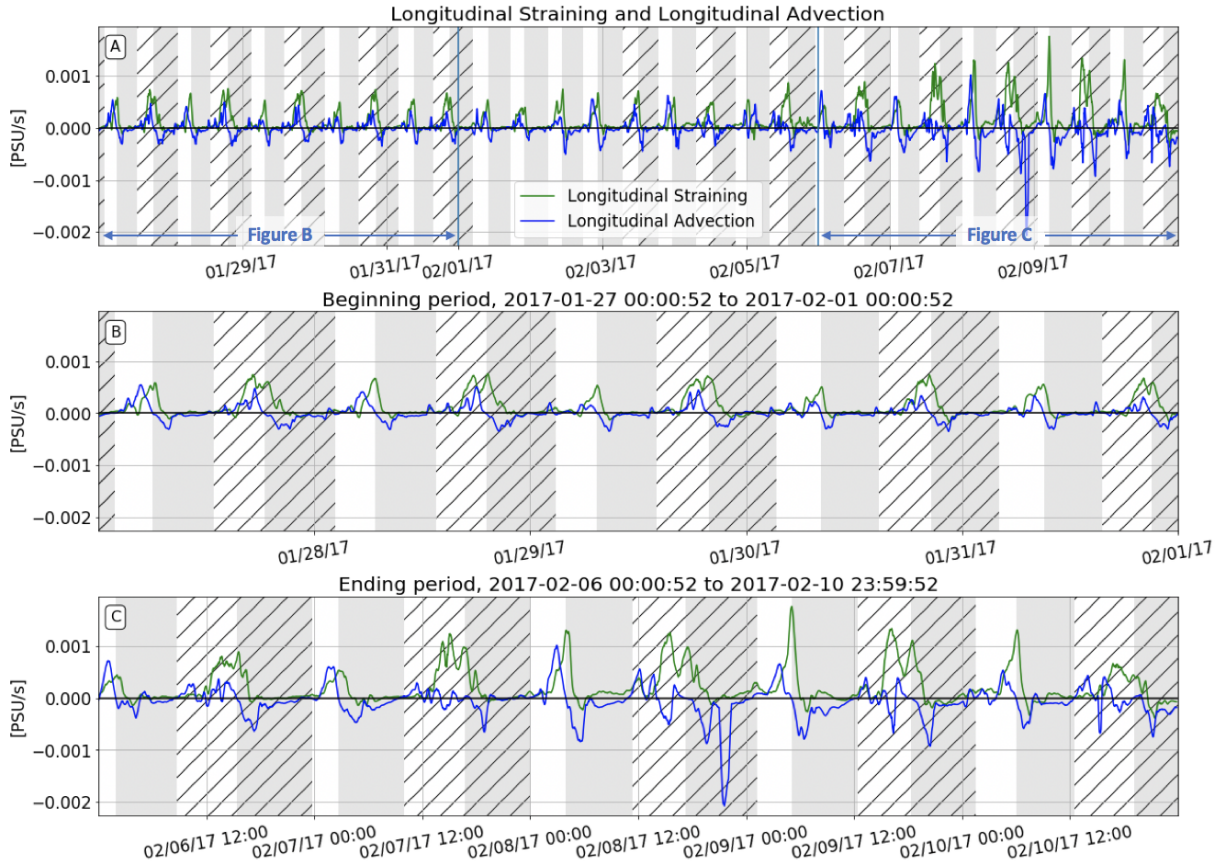

Figure 2.9: Longitudinal straining and longitudinal advection in [PSU/s]. Longitudinal salinity gradients were calculated using lines 1 and 3. (A) Entire time series, (B) First, dry spring tide, (C) Second, wet spring tide. Note: Flood tides correspond to gray shading. Ebb tides correspond to white shading. Hatching refers to larger flood/ebb tides when there is a diurnal asymmetry.

The blue line in Figure 2.9a shows a persistent translation of stratification to our central site on ebbs due to longitudinal advection and the reverse on floods due to longitudinal advection. This tidal pattern is consistent with the expectation that the water column is well-mixed at the Dumbarton Narrows and more stratified near the perimeter. Positive values of longitudinal advection during the ebb tide translate to more stratified water near the perimeter advecting to the center of the estuary and reaching a maximum at the end of the ebb. During the flood tide, this term is negative as it translates the well-mixed waters from the mouth to the center of the estuary. This result highlights the importance of localized mixing (at a specific location like the Narrows) in the stratification dynamics of adjacent embayments. When there is an increase in buoyant input, the magnitude of longitudinal advection is greater, which is likely due to the fact that the stratification difference between the mouth of the estuary and near the perimeter of the estuary is increased when there is

more freshwater input (Figure 2.9c).

Lateral Straining

Lateral straining is the creation or destruction of stratification due to the lateral straining of the lateral density gradients. The lateral salinity gradient is almost always negative (Figure 2.5a) as the water in the shoals are fresher than the water in the channel except at the end of the ebb tide when differential advection causes the channel to be fresher than the shoals. While the lateral circulation is expected to be driven by the lateral density gradient, we use the observed bottom-top velocity difference ($v_b - v_t$, Figure 2.7b) to determine a negative $v_b - v_t$ persists through much of the flood tides, but this shear reverses briefly at the end of each ebb tide, coincident with the reversal of the lateral density gradient. It is difficult to see clear signals of lateral exchange from the lateral velocity and lateral salinity observations as even when the lateral salinity gradient remains negative during the small ebb tides, we still observe increases in salinity. This could be due to the location that the shoal salinity is measured.

As a result of the correlation between lateral shear and lateral density gradients, the contribution of lateral straining to stratification in the channel is expected to be positive (stratifying); since density driven flow can only be stratifying, any negative contributions to stratification indicate that the forcing of the lateral circulation must come from other mechanisms such as bathymetric effects on the tides (channel curvature or the effects of broad shoals and storage), Coriolis, and wind. Reinforcing the density-driven mechanism for the lateral circulation, there is a recurring positive peak at the end of the flood tide, when the lateral density gradient and circulation are strongest. This peak is created by the interaction of differential advection building up the lateral density gradient throughout the flood tide until the reduction in turbulent mixing at the end of the flood tide allows lateral exchange flow to develop.

In the first couple of tidal cycles in Figure 2.10b, during the ebb tide, the lateral straining term is variable, with sign changing between positive and negative throughout the ebb. Although highly variable, this pattern is consistent over the ebb tides in the dry spring. During the flood tides (gray shading), the lateral straining term is negative mid-flood tide, then increases to a maximum positive value by the end of the flood tide. The ebb-to-flood transition does not show a significant contribution from lateral straining, which is consistent with the fact that the lateral density gradients are quite small at this time.

At each mid-flood tide, lateral straining contributes negatively to stratification, but during a period when the water column is already well-mixed entirely (Figure 2.3). In order for lateral straining to contribute to destratification, the orientation of the straining must be the opposite of expected under only density forcing. We are seeing here the lateral equivalent to overstraining [36] and therefore lateral straining is contributing to turbulent mixing during the flood tides. To be clear, we hypothesize that this is really just a directional shear that is created by the interaction of the tides with the shoal-channel transition, and not a

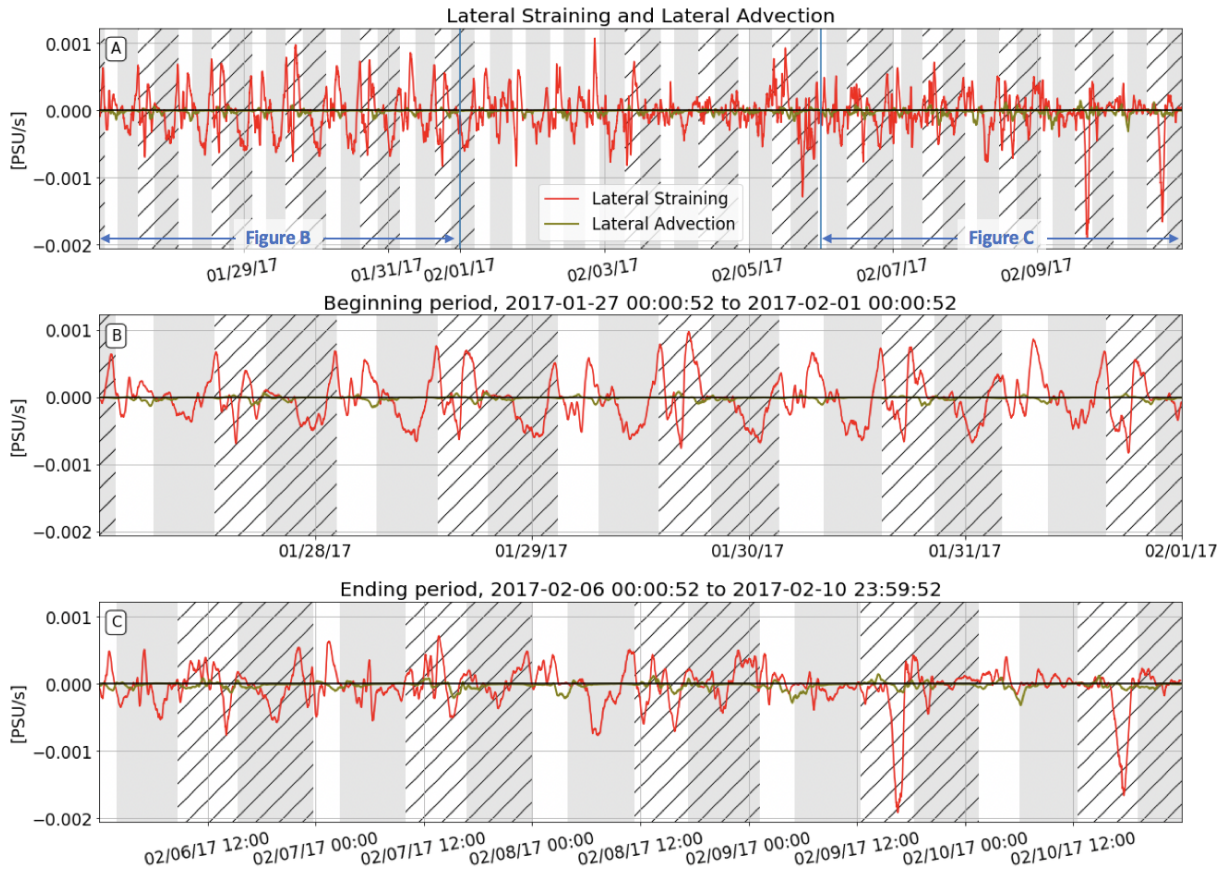

Figure 2.10: Lateral straining and lateral advection in [PSU/s]. Lateral salinity gradients were calculated using lines 2 and 6. (A) Entire time series, (B) First, dry spring tide, (C) Second, wet spring tide. Note: Flood tides correspond to gray shading. Ebb tides correspond to white shading. Hatching refers to larger flood/ebb tides when there is a diurnal asymmetry.

new lateral mechanism. However, it indicates that estimates of straining based purely on longitudinal gradients and shear would underestimate the magnitude of overstraining.

Lateral Advection

The final term that can be directly calculated is small throughout the tidal cycle due to the fact that the depth-averaged lateral velocity is small. Deviations from zero occur during periods of time when the depth-averaged velocity does not align with the primary tidal axis, which was used to define the rotation of the coordinate axis. The only period of time when the term contributes is near the end of the ebb tide, when barotropic forcing draws unstratified water from the shoals into the stratified channel, thus contributing to destratification in the channel.

2.5 Discussion

Summary of Tidal Variability

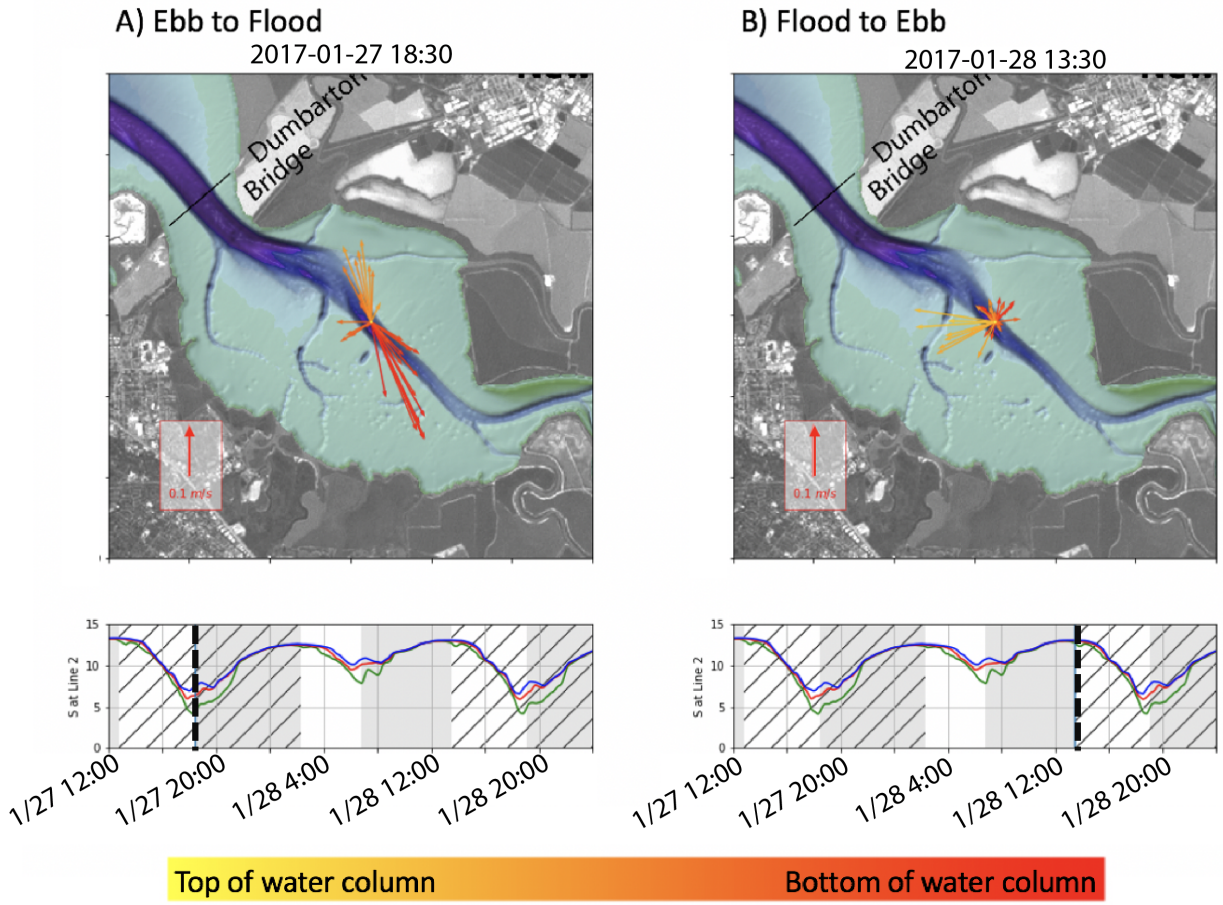

Figure 2.11: Velocity vectors at line 2 shows differences in lateral exchange flow patterns in the ebb to flood versus the flood to ebb tide transitions. Red arrows represent the bottom depth flows and the yellow arrows represent the top flow directions. (A) At the ebb to flood transition we see a pulse of lateral flow from the near bed shoal to the mid-column channel. Note the pictured longitudinal shear that occurs during this tidal transition. As the tide transitions from ebb to flood, the bottom reverses sign before the top. (B) At the flood to ebb transition we see a two-layer lateral exchange flow where the bottom is directed from the channel to the shoal and the flow at the top of the water column is directed from the shoal to the channel. Ebb tides correspond to white shading. Hatching refers to larger flood/ebb tides when there is a diurnal asymmetry.

The analysis of the previous section defines the tidal variability and relative magnitude

of the various mechanisms responsible for stratification and destratification. Three terms, in addition to turbulent mixing, are important contributors: longitudinal straining, longitudinal advection and lateral straining (Figure 2.13). Longitudinal straining varies as would be expected under SIPS, in addition to a strong peak at the ebb-flood transition due to vertical phase lag in the tidal reversal. Longitudinal advection is important at this site due to the close proximity between the "mouth" at the Dumbarton Narrows and the shallow marsh perimeter. Energetic mixing at the Narrows creates strong along-axis gradients in stratification, with less stratified conditions down estuary that are tidally-advected along the estuarine channel, contributing strongly to the variability of stratification in the channel. Finally, lateral straining is an important contributor to channel stratification dynamics, but with a complex tidal variability created by the interplay between differential advection, which creates lateral density gradients, and turbulent mixing, which inhibits the development of lateral circulation. This last element is similar to the conditions studied by Lacy et al. [25], and just as in that case, the lateral straining produces stratification late in the flood tide that would never be predicted by traditional SIPS frameworks.

Figure 2.11 illustrates the difference in lateral exchange at the ebb to flood versus the flood to ebb transitions. The lateral exchange at the ebb to flood transition is much smaller in magnitude, occurring in the middle of the water column, and has limited lateral shear. At line 2, the lateral flows are all in one direction, from the shoals towards the channel. There is also a vertical lag in the reversal of longitudinal flow at the transition from ebb to flood. In contrast, on the flood to ebb transition, the lateral exchange has high shear with the bottom lateral velocities traveling from the channel towards the shoal and the top lateral velocities at higher magnitude going from the shoal towards the channel. The two-layer lateral profile is expected for lateral flows that are baroclinically driven. The differences in the lateral flows can also be seen in the salinity signature at each tide transition (Figure 2, e.g.). In the ebb to flood salinity time series, there is an increase in salinity at all sensors due to the more saline waters in the shoal being barotropically pushed into the channel. In the flood to ebb transition, the fresher shoal water is being transferred to the top of the channel, resulting in the freshening of the top sensor at line 2.

The longitudinal and lateral Simpson numbers shown in Figure 2.12. The longitudinal Simpson number was calculated using equation 2.2 where u_*^2 is calculated as $0.0025u_{avg}^2$. The lateral Simpson number is calculated using the following equation,

$$Si_y = \frac{g\beta\frac{\partial S}{\partial y}H^2}{u_*^2} \tag{2.9}$$

During the small ebbs (unhatched, white sections) we see the most potential for stratification. The small ebbs do not have as much breakdown of stratification (remains above 0.2) whereas the large ebbs drop below 0.2 in the mid-late ebb. These instances where we see the Simpson number drop below 0.2 in the mid-late ebb corresponds to the times we observed mid-ebb destratification in Figure 2.3. When approaching the slack tide, there is a drop in turbulent mixing (scaled by $\frac{1}{0.0025u_{avg}^2}$). The large Simpson number during slack tides indicates likely

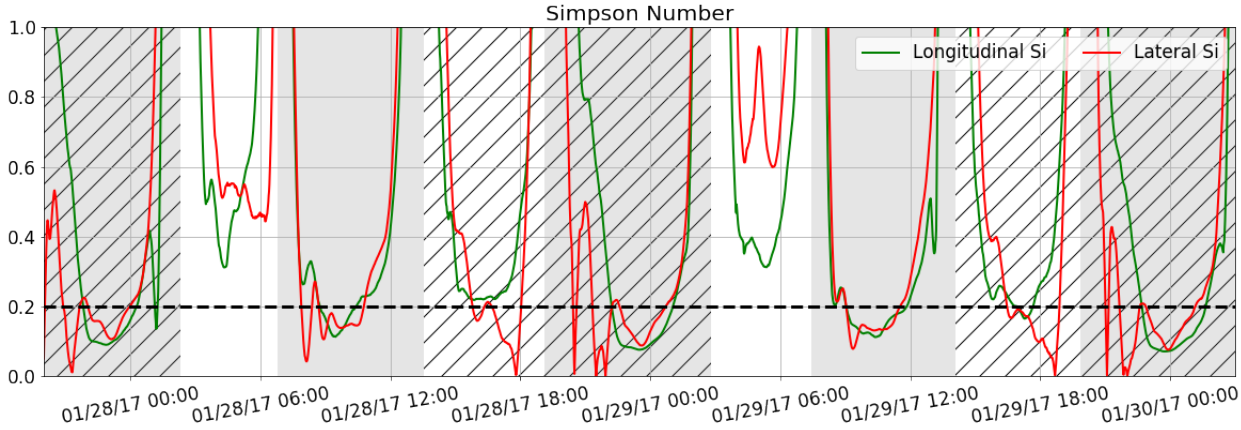

Figure 2.12: Longitudinal (green) and lateral (red) Simpson Numbers at line 2 [26]. The larger the value of the Simpson number, the more likely the water column is to stratify. Note: Flood tides correspond to gray shading. Ebb tides correspond to white shading. Hatching refers to large flood/ebb tides when there is a diurnal asymmetry.

stratification. Therefore, small ebbs and slack tides are more likely to stratify. The lateral Simpson number has a similar pattern and magnitude to the longitudinal Simpson number which emphasizes the importance of lateral density forcing. There are even times, such as the small ebb tide on January 29, 2017, where the lateral Simpson number exceeds the longitudinal Simpson number by a factor of 2.

The aggregation of longitudinal straining, longitudinal advection, lateral straining, and lateral advection are shown in Figure 2.8, including a comparison with the measured $\frac{\partial S_z}{\partial t}$. The creation of stratification over the ebb tides is captured well in time and magnitude. In contrast, the two negative destratification peaks at the beginning of the flood are not captured by the calculated $\frac{\partial S_z}{\partial t}$. Longitudinal advection does produce a significant destratification early in the flood, but occurs later in the flood tide and is more dispersed than the directly observed destratification. The most likely explanation of this difference is the presence of two frontal features that each reduce the stratification as they advect past the station. By using differences to estimate the longitudinal gradient, we underestimate the gradient, resulting in a more dispersed advective feature.

Totaling all the terms confirms overstraining is occurring in the late flood tides. Figure 2.13 shows that longitudinal straining and lateral straining are mostly responsible for the creation of stratification at the end of the ebb tide, and longitudinal advection and lateral straining are responsible for the destratification over the flood tide.

Details of Tidal Dynamics

Ebb Tide

At the beginning of the ebb tide, salinity begins to drop and there is a sheared velocity

profile. Progressing to the middle of the ebb tide, there is a creation of stratification with a quick breakdown of stratification when the tidal velocity is at a maximum. This breakdown is likely due to turbulent mixing. Over the ebb tide, longitudinal advection tightens isohaline lines, advecting a more stratified water column from the perimeter to the central site. From the middle of the ebb tide until the end of the ebb tide, longitudinal straining contributes to the creation of stratification. As shown in Figure 2.14, it appears longitudinal advection, longitudinal straining and lateral straining are activated at the same time. The shear in the lateral velocity (Figure 2.7) reaches a maximum in the mid-ebb tide resulting in a large contribution of lateral straining. This lateral strain occurs before the lateral salinity gradient has reversed meaning the shoal water that is brought into the channel is fresher than the channel adding to the creation of stratification in mid-ebb. At the same time, longitudinal straining also contributed to the creation of stratification from mid-late ebb. Even though longitudinal straining is overall dominant in creating stratification over the ebb tide, the contribution of lateral straining is significant at the very beginning of the ebb tide and over mid-late ebb.

Ebb to Flood Transition

As the tide transitions from late-ebb to early-flood, salinity increases in the top, middle, and bottom of the water column. Longitudinal straining causes further development of stratification during this transition as the bottom velocity continues in the ebb direction and the top of the water column reverses to the flood direction resulting in maximum longitudinal shear. Differential advection causes the channel to be fresher than the shoal explaining why there are increases in salinity in the water column at ebb to flood transitions. This increase in salinity also corresponds to increase in stratification. It should be noted that the strength of lateral circulation does not correspond with the strength of the lateral density gradient. The lateral density gradient is greatest at the end of the flood tide and the maximum measured lateral circulation was found at the end of the ebb tide. Maximum lateral circulation at the end of the ebb tide is due to decreasing turbulence due to reduced tidal velocity magnitudes and ambient stratification. During this tide transition, lateral baroclinic pressure gradients are small. Therefore, the lateral exchange at the transitions are driven by different forcings.

Flood Tide

Over the flood tide, salinity begins to increase. There is a more uniform longitudinal velocity. Stratification is broken down in two distinct instances. The first destratification event was not captured in measurements suggesting it is due to a frontal feature that is not spatially resolved. The second destratification event is due to longitudinal advection bringing more well-mixed water from the narrows. As the flood tide persists, there is little longitudinal or lateral shear. From mid-late flood, lateral straining contributes to overstraining which results in increased mixing.

Flood to Ebb Transition

At the end of the flood tide, stratification begins to develop. Although the measured lateral velocity is low, at the end of the flood tide, lateral salinity gradient is at a maximum. At this time, the shoal is fresher than the channel (opposite from the lateral salinity gradient at the end of the ebb tide). Looking at the salinity pattern in the top, middle, and bottom of

the water column in Figure 2.2, at each flood to ebb transition, there is a pulse of freshwater at the surface sensor. Right at the beginning of this pulse, there is a two-layer lateral velocity profile with the bottom of the water column pulling channel water towards the shoal and the top of the water column pulling shoal water towards the channel. The deviation of the top salinity from the bottom salinity results in the creation of stratification at the flood to ebb transition.

2.6 Concluding Remarks

Observations in Lower South San Francisco Bay illustrated the tidal variations of stratification, including an evaluation of the responsible mechanisms. The most significant stratification event occurs at the ebb-flood transition due to a combination of longitudinal straining and longitudinal advection. Further stratification was developed at the beginning of the flood tide due to a vertical shear created by a phase lag in the tidal velocities. The most important destratification period is the early flood tide, during which a sequence of mechanisms is found to be responsible. First, a pulse of saline water is received in the top, middle, and bottom of the channel water column. Next, longitudinal advection carries progressively less stratified water masses into the observed water column, and the observations seem to indicate passage of two strong frontal transitions during this period. Finally, throughout the flood tide, longitudinal straining works to reduce the stratification; once the water column is destratified, it produces turbulent mixing through overstraining.

Stratification dynamics switch between being longitudinally dominated during the middle of ebb and flood tides to being laterally dominated during the tidal transitions. Differential advection along with lateral exchange at tide transitions resulted in more saline water transported from the shoals to the channel at the end of each ebb tide from barotropic forcing and less saline water transported from the shoals to the top of the channel at the end of the flood tide from baroclinic forcing. Lastly, estimates of the impact of lateral advection on the creation or destruction of stratification were found to be insignificant compared to longitudinal mechanisms and lateral straining except briefly at the end of the ebb tide.

The variation of the lateral density gradient is not symmetric between ebb and flood, and the lateral density gradient is much smaller in magnitude at the end of the ebb tide than it is at the end of the flood. At the end of the flood tide, fresh water in the shoals exchange with a saline channel, which produce pulses of near-surface waters into the channel from the density-driven lateral exchange. At the end of the ebb tide, this structure is not reversed, and the lateral density gradients are quite small. The salinity structure shown at the central location suggests that the lateral exchange is driven by a cross-channel barotropic forcing at the end of the ebb tide which is difficult to see in the limited lateral velocity data in the shoals.

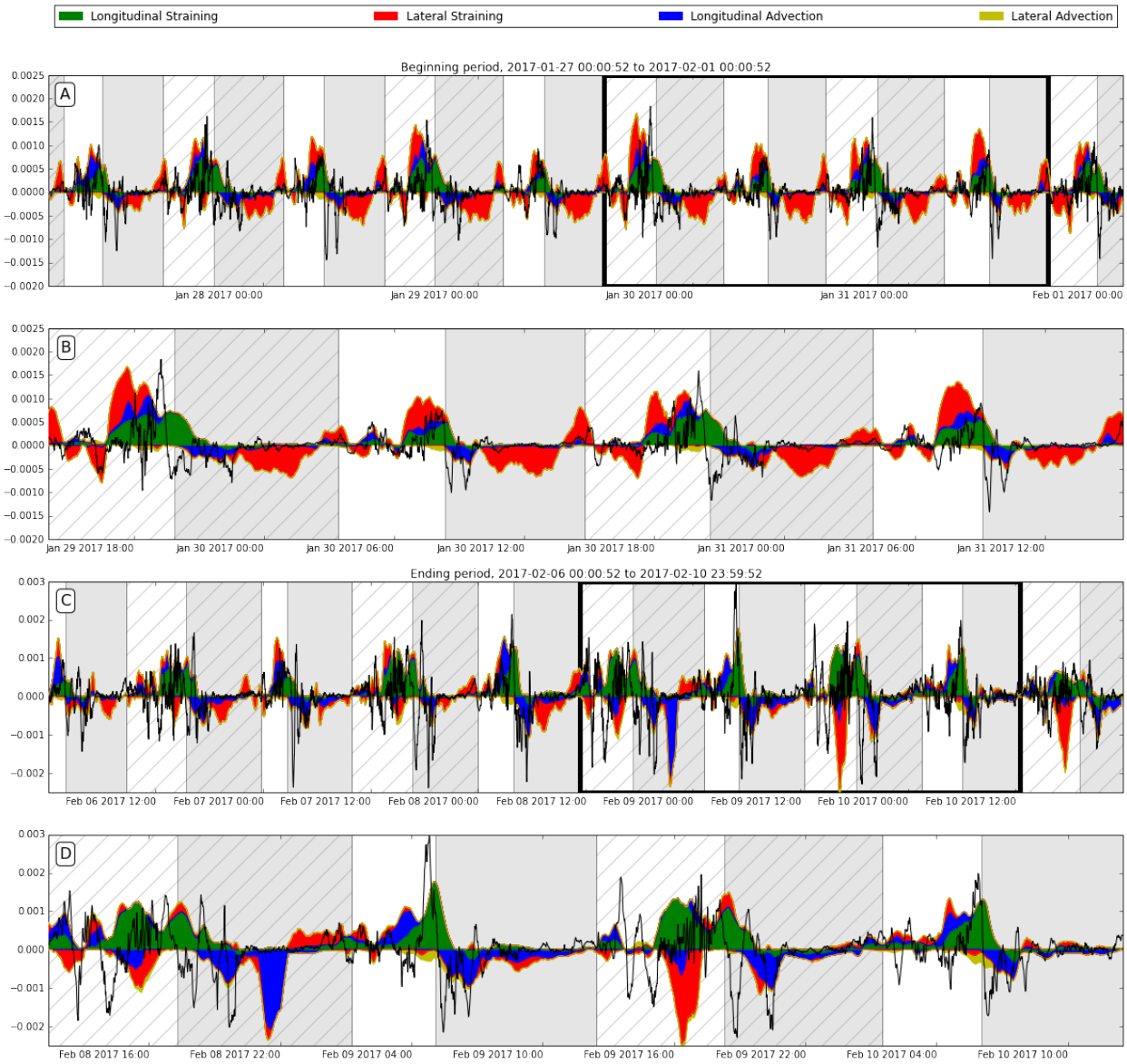

Figure 2.13: Fill plot of measured versus calculated $\frac{\partial S_z}{\partial t}$ $[\frac{PSU}{s}]$. Note the vertical distance shown for each color is the contribution of that term. The areas are not overlaid, so the magnitude of lateral straining is added onto the area of longitudinal straining, not behind. The positive area has not had the negative area subtracted from it. By adding the positive area and the negative area at each time step, you would get the blue lines shown in Figure 2.8. The measured value of $\frac{\partial S_z}{\partial t}$ is plotted in black. (A) Shows the first, dry spring tide. (B) Zooms into 4 tidal cycles outlined by the black box in subplot A. (C) Shows the second, wet spring tide. (D) Zooms into 4 tidal cycles outlined by the black box in subplot C.

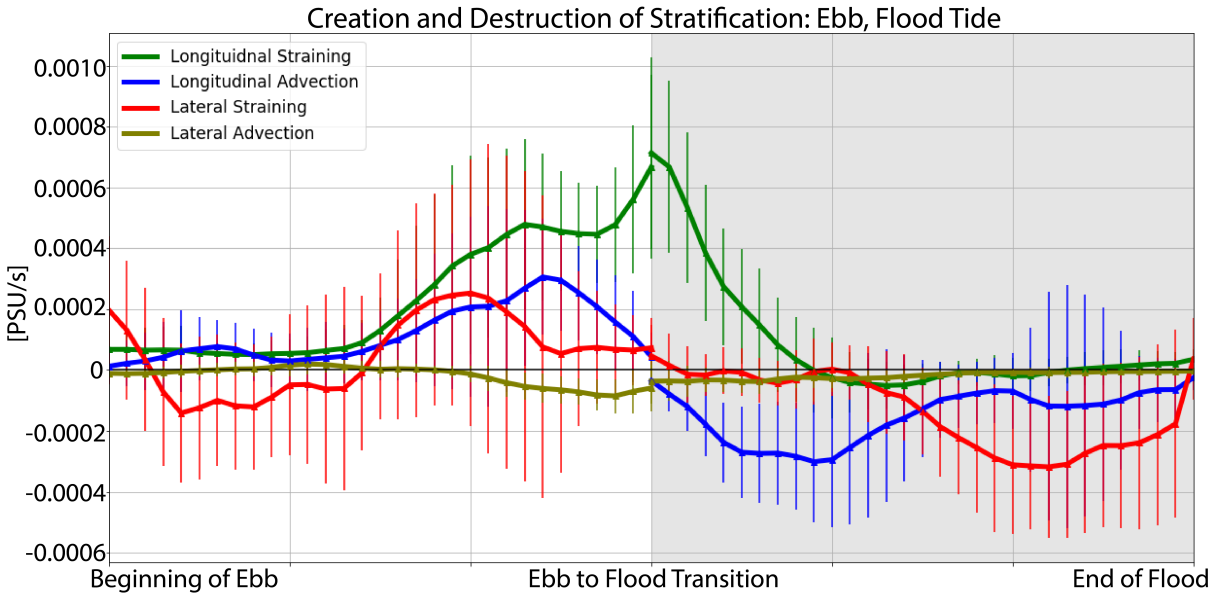

Figure 2.14: Tidal phase averaged calculated longitudinal straining, longitudinal advection, lateral straining, and lateral advection. Longitudinal gradients were calculated using lines 1 and 3 to estimate and lateral gradients using lines 2 and 6 . The first half shows tidally-averaged values over the ebb tide, and the second half in gray shows tidally-averaged values over the flood tide. Longitudinal straining works to create stratification from mid-ebb until mid-flood. Longitudinal advection creates stratification at the end of the ebb tide and then works to destratify at the beginning of the flood tide. Lateral straining becomes important at the end of the ebb tide and the end of the flood tide. At the end of the ebb tide, lateral straining creates stratification and over mid to late-flood lateral straining overstrains the water column inputting turbulent energy maintaining a homogeneous vertical salinity structure in the channel.

Chapter 3

Using Eulerian Temperature Measurements to Estimate Residence Time in Lower South San Francisco Bay

3.1 Introduction

In estuaries, buoyant input through rivers and precipitation pushes seaward while denser ocean water pushes landward resulting in estuarine circulation. Defining bulk characteristics such as exchange flow is motivated by a number of hydrological, biological, and geochemical applications [35]. Residence time or flushing time is the first-order description of transport in a water body. One may think of the residence time as a measure of how long a water parcel remains within a defined water body [13]. Estimates of residence times are used to determine mass balances [8], the variability of dissolved nutrient concentrations [1], dissolved organic carbon concentration [10], plankton abundance in rivers [3], the occurrence of harmful algal blooms [9], the distribution of pelagic bacteria [43], the export of copepod life stages [41], and the partitioning of primary production between macroalgae and phytoplankton [57].

An estuary's circulation is dependent on multiple factors including freshwater input via rivers, tides and currents, wind, and turbulent mixing. Observations over 17 years in Chesapeake Bay revealed effective horizontal dispersion was inversely proportional to the cross sectional area of the estuary, and had an inverse dependence of dispersion and freshwater flux [2]. Spatial and temporal variations caused the dispersion coefficient to vary between 200 and 1000 m^2/s [2].

Knudsen 1900 relations integrate water and salt budgets resulting in net tidally averaged salt flux in through the estuary mouth equaling the flux out through that section in steady state. It is often found that the tidal salt flux can be comparable to the exchange flow, so estuarine literature has been focused on resolving salt gradients and fluxes [30]. In order to

understand salinity budgets, researchers simplify the system into a small number of "boxes". By assuming a steady state, tidally-averaged salinity field and salinity observations at varying depths and along-channel locations, one may fit data to estimate the time-mean advection and diffusion of salinity through the sides of the boxes [32]. By using this box method, one can directly apply observed estuary data to estimate residence times, but by simplifying the estuarine salinity field into Eulerian boxes, physical processes within each box remain unresolved [32].

There are differing idealized cases that are used each with its own limitations due to underlying assumptions. One idealized definition of flushing time, T_f, is defined as the ratio of the mass of a scalar in a reservoir to the rate of renewal of the scalar [20]. This ratio can be determined using the volume of water in a defined system or the mass of a scalar in the domain by equations 3.1 and 3.2 where V is the volume of water in a defined system, Q is the volumetric flow rate through a system, M is the mass of a scalar in the domain, and F is the flux of the scalar through the domain.

$$T_f = \frac{V}{Q} \tag{3.1}$$

$$T_f = \frac{M}{F} \tag{3.2}$$

Calculating the flushing time with this ratio does not allow users to identify the spatial distribution of physical properties that are important in the variation of the final T_f of a system [35]. Often times V or M and Q or F are unknown, so computations of T_f are made with various assumptions. To reduce the number of unknowns, a common assumption made is to view the water body as a continuously stirred tank reactor (CSTR). In a CSTR any mass introduced to the system is instantly and evenly mixed throughout the domain, making the concentration of a constituent exiting the domain equal to the concentration everywhere inside the CSTR [35]. Assuming an initial constituent concentration, C_0, added to the CSTR at time $t = 0$ and there is no further constituent mass added after that time, for a given, constant flow rate Q, the concentration inside of the CSTR can be defined by equation 3.3 [56]. This method underestimates the flushing time because of the well-mixed assumption.

$$C(t) = C_0 e^{-(Q/V)t} = C_0 e^{-t/T_f} \tag{3.3}$$

Solving this equation results in an exponential decay of the concentration that asymptotically approaches 0. The CSTR flushing time calculated using this model is a representation of the average amount of time that mass spends in the system.

Another approach to solve the time when V or M and Q or F are unknown is the tidal prism method [14]. This method is useful when the basin geometry and tidal range are known for a given system. Flushing time is approximated using equation 3.4 where P is the tidal prism or the domain between the high and low tide marks, V is the mean basin volume which can be estimated by multiplying the tidal range with the surface area, T is

the tidal period, and b is the return flow factor or the fraction of effluent water returning to the domain each flood tide.

$$T_f = \frac{VT}{(1-b)P} \tag{3.4}$$

For this method it is assumed that the system is well mixed, compared to the tidal flow, the river flow is small, the system is at a steady state with a sinusoidal tidal signal, and the receiving water is large enough to dilute the water exiting the basin so that the receiving water does not change or affect the effluent [46]. The tidal prism method tends to underestimate the flushing time because of the well mixed assumption [14, 46, 42]). The choice of b can also create highly variable calculations of flushing time. This method cannot allow for variations in wet or dry seasons or unsteadiness, making it difficult to practically apply to many tidal water bodies [35].

Each of these methods have assumptions and limitations. Additional methods to estimate the residence time of a system can serve as a way to check sensitivity or to get another estimate of the estuarine circulation. In this chapter, the difference in perimeter and channel water temperature is used to estimate an exchange rate between two subsystems within an estuary domain. The previous methods to calculate exchange rate or flushing time are limited in terms of spatial resolution within the defined boundaries of the water system. Therefore, this analysis will help understand the exchange between the perimeter and channel. To accomplish this we look at field data in Lower South San Francisco Bay that is readily available and accessible to the public through online databases from the California Irrigation Management Information System (CIMIS) and the San Francisco Estuary Institute (SFEI).

3.2 Data Sources and Box Model

Lower South San Francisco Bay

Lower South San Francisco Bay (LSSFB) sits within the urbanized and densely populated Bay Area. Freshwater flow in the estuary from wastewater effluent brings high nutrient concentrations. Risks to future ecosystem conditions, and the role that nutrients may play in limiting or facilitating a transition to eutrophic conditions, have motivated a reconsideration of the dynamics of stratification in LSSFB. Recent evidence of decreasing turbidity reinforces concerns about threshold-like transitions in the system, particularly if stratification were to increase in strength or duration under future climate forcing [11, 47]. Due to potential future eutrophic conditions, it is important to understand bulk characteristics such as the estuarine flushing rate and exchange rate between the perimeter and channel.

Location	Box	Latitude	Longitude
San Mateo Bridge	Ocean	37.584446	-122.24889
Lower South San Francisco Bay	Estuary	37.47798	-122.07658
Alviso Slough	Perimeter	37.44	-121.99834

Figure 3.1: Locations of observed temperatures. Water temperature at San Mateo Bridge and Alviso Slough were collected by the San Francisco Estuary Institute's (SFEI) moored sensors program. Water temperature at LSSFB is an original data set collected by UC Berkeley.

Data Sources

Three data sources were used in the calibration of this model. The first from a University of California, Berkeley deployment which collected temperature at the top, middle, and bottom of the water column at a central location in the channel of LSSFB from September 2015 to February 2017 previously named channel marker 17 (CM17) by the United States Geological Survey (USGS) (Figure 3.1). The second data source came from San Francisco Estuary Institute's moored sensors program available on their open source ERDDAP data server. The moored sensors provided 15-minute water temperatures in the perimeter of LSSFB (Alviso Slough) and 15-minute water temperatures at the San Mateo bridge. For the rest of the paper reference to "perimeter" water corresponds to the water at Alviso Slough and "ocean" water with the water at San Mateo bridge. Finally, external conditions such as solar radiation, precipitation, air temperature, relative humidity were collected every hour by the California Irrigation Management Information System (CIMIS).

Box Model

A simple three box model with two diffusion coefficients is used to represent the tidally-averaged exchange between water outside of LSSFB (ocean), in the estuary, and in the marsh perimeter. The coefficient $K_{D,1}$ represents diffusion between the perimeter and estuary and $K_{D,2}$ represents diffusion between the ocean and estuary. There are two potential flux input locations into the estuary control volume, the ocean and perimeter boxes. Heating from the atmosphere is considered in the estuary and perimeter control volumes whereas the ocean temperature remains constant.

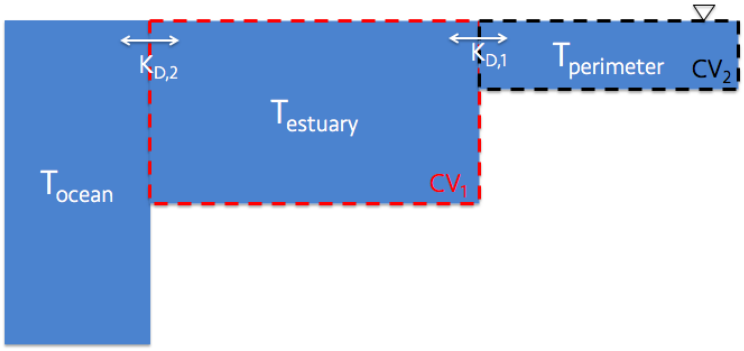

Figure 3.2: Control volumes used to represent the ocean, estuary, and perimeter for the temperature exchange model where $K_{D,1}$ represents the diffusive flux between the estuary and perimeter surface area and $K_{D,2}$ represents the diffusive flux between the estuary and ocean surface area.

The diffusion equation for a passive tracer in the estuary, C_e, in our three box system shown in Figure 3.2 is described by the following equation:

$$V_e \frac{\partial C_e}{\partial t} = \frac{K_{D,1}}{L_1}(C_p - C_e)A_1 + \frac{K_{D,2}}{L_2}(C_o - C_e)A_2 \tag{3.5}$$

where V_e is the volume of the estuary, $K_{D,1}$ is the diffusive coefficient at the perimeter-estuary interface and $K_{D,2}$ is the diffusive coefficient at the ocean-estuary interface, L_1 is the distance between the center of the estuary control volume and the center of the perimeter control volume, L_2 is the distance between the center of the ocean control volume and the center of the estuary control volume, A_1 is the effective cross-section between the perimeter and estuary control volumes, and A_2 is the effective cross-section between the estuary and ocean control volumes.

The volume of the estuary is defined by the multiple of the length, height, and width of the estuary box, $V_e = L_e H_e W$. L_1 is calculated as an average of the length of the perimeter and estuary, $L_1 = \frac{1}{2}(L_e + L_p)$, and L_2 is the average of the estuary and ocean length, $L_2 = \frac{1}{2}(L_o + L_e)$. And finally A_1 and A_2 are calculated using the average water depths as the cross-sectional depth multiplied with the width, $A_1 = \frac{1}{2}(H_e + H_p)W$ and $A_2 = \frac{1}{2}(H_o + H_e)W$.

Using these definitions, the time rate of change for a passive tracer in the estuary control volume can be expressed as,

$$\frac{\partial C_e}{\partial t} = [\frac{K_{D,1}(H_e + H_p)}{(L_e + L_p)(L_e H_e)}](C_p - C_e) + [\frac{K_{D,2}(H_o + H_e)}{(L_o + L_e)(L_e H_e)}](C_o - C_e) \tag{3.6}$$

For the perimeter control volume

$$\frac{\partial C_p}{\partial t} = \frac{K_{D,1}(H_e + H_p)}{(L_e + L_p)(L_p H_p)}(C_e - C_p) \tag{3.7}$$

This framework can now be applied to the time rate of change of water temperature in the estuary and perimeter control volumes by the following two equations where the volumetric ratios are defined by β values. β values are defined in equations 3.10, 3.11, and 3.12:

$$\frac{\partial T_e}{\partial t} = \alpha_e \widetilde{H}_{atm} + K_{D,1}\beta_1(T_p - T_e) + K_{D,2}\beta_2(T_o - T_e) \tag{3.8}$$

$$\frac{\partial T_p}{\partial t} = \alpha_p \widetilde{H}_{atm} + K_{D,1}\beta_3(T_e - T_p) \tag{3.9}$$

T_o is the water temperature in the ocean, T_e is the water temperature in the estuary, and T_p is the water temperature in the perimeter. The $\alpha_e \widetilde{H}_{atm}$ and $\alpha_p \widetilde{H}_{atm}$ terms describe changes in the estuary or perimeter due to atmospheric heating or cooling. In the model, values for T_o, $T_{e,0}$, $T_{p,0}$, $\alpha_e \widetilde{H}_{atm}$, $\alpha_p \widetilde{H}_{atm}$ are assigned. $K_{D,1}$ and $K_{D,2}$ are fitting parameters. β_1, β_2, and β_3 are ratios to account for volumetric differences in the control volumes.

$$\beta_1 = \frac{(H_e + H_p)}{(L_e + L_p)(L_e H_e)} \tag{3.10}$$

$$\beta_2 = \frac{(H_o + H_e)}{(L_o + L_e)(L_e H_e)} \tag{3.11}$$

$$\beta_3 = \frac{(H_e + H_p)}{(L_e + L_p)(L_p H_p)} \tag{3.12}$$

The associated diffusive time can be scaled as $T_{dif} \sim \frac{L^2}{K_D}$. Through this scaling, equation 3.13 estimates the amount of time a water parcel remains in the perimeter before it is exchanged into the estuary, $T_{perimeter}$, and equation 3.14 gives an estimate of how long a water parcel remains in the estuary before it is exchanged into the ocean, $T_{estuary}$.

$$T_{perimeter} = \frac{(\frac{1}{2}(L_e + L_p))^2}{K_{D,1}} \tag{3.13}$$

$$T_{estuary} = \frac{(\frac{1}{2}(L_e + L_o))^2}{K_{D,2}} \tag{3.14}$$

The water temperature in the estuary, T_e, is governed by equation 3.8 and the perimeter water temperature, T_p, is governed by equation 3.9. In order to avoid numerical instabilities, an implicit scheme is used. Equation 3.15 is used to calculate the estuary water temperature and equation 3.16 to calculate the perimeter temperature time series.

$$T_e^n = \frac{T_e^{n-1} + \Delta t \alpha_e \widetilde{H}_{atm}^n + \Delta t K_{D,2} \beta_2 T_o^n + (\frac{\Delta t K_{D,1} \beta_1}{1+\Delta t K_{D,1} \beta_3}) T_p^{n-1}}{1 + \Delta t K_{D,1} \beta_1 + \Delta t K_{D,2} \beta_2 - \frac{(\Delta t K_{D,1})^2 \beta_1 \beta_3}{1+\Delta t K_{D,1} \beta_3}} \tag{3.15}$$

$$T_p^n = \frac{T_p^{n-1} + \Delta t \alpha_p \widetilde{H}_{atm}^n + \Delta t (K_{D,1} \beta_3 T_e^n)}{1 + \Delta t K_{D,1} \beta_3} \tag{3.16}$$

Variable	**Equation**
Sensible heat transfer	$H_S = C_S \rho_A C_P U (T_0 - T)$
Heat loss due to evaporation	$H_L = C_L \rho_A L_W U (Q_0 - Q)$
Long wave radiation	$H_1 = -5.18 \times 10^{-13} (1 + 0.17 C^2)(273 + T)^6$
Back radiation from water surface	$H_2 = 5.23 \times 10^{-8} (273 + T_0)^4$
Short wave radiation	Directly measured (CIMIS)

Table 3.1: Equations used to calculate thermal heating where H values are in units of $[\frac{W}{m^2}]$, C_S is the coefficient for wind stress variability [-], ρ_A is the air density $[\frac{kg}{m^3}]$, C_P is the specific heat of air $[\frac{J}{kg°C}]$, U is the wind speed at 10 m $[\frac{m}{s}]$, T_0 is the water surface temperature $[°C]$, and T is the air temperature at 10 m $[°C]$, C_L is the coefficient for wind stress variability [-], L_W is the latent heat of evaporation $[\frac{J}{kg}]$, Q_0 is the saturation specific humidity [kg of water moisture/kg of air-water moisture], and Q is the specific humidity at 10 m.

The change in temperature in the estuary and perimeter control volumes due to heat flux for a given day was calculated using equations from "Mixing in Inland and Coastal Waters" by Fischer et al. Table 3.1 [15]. The following constant values were used to calculate H_S and H_L: $C_S = C_L = 1.45 \times 10^{-3}$, $\rho_A = 1.2\ kg/m^3$, $C_P = 1012\ \frac{J}{kg°C}$, $L_W = 2.4 \times 10^6\ \frac{J}{kg}$, $Q_0 = 1.9 \times 10^{-2}$. The wind speed at 10 m, U, was extrapolated for each hour in the time window of April 1, 2016 - August 31, 2016 from CIMIS. The water temperature at the surface, T_0, was taken for each hour using measured temperature from the CTD at channel marker 17. The air temperature at 10 m, T, came from from the CIMIS dataset. Q was calculated using the relative humidity from the CIMIS dataset. C is the fraction of the sky covered by cloud and T is the air temperature at 10 m. It was assumed that the sky was cloudless ($C = 0$) which is a valid assumption for South Bay in the summer. The air temperature at 10 m, T, was measured by CIMIS. Finally, the short wave radiation, H_{SW}, was directly measured by CIMIS in $\frac{W}{m^2}$.

The saturation specific humidity, Q_0, is the maximum amount of water vapor that can exist in the air for a given temperature and pressure. At sea level and $20°C$, $Q_0 = 0.015\ g/g$ and at $25°C$, $Q_0 = 0.02\ g/g$ [40]. Therefore, $Q_0 = 0.019\ g/g$ was selected and is used throughout

all model analyses completed in this chapter. The air saturation, Q, was calculated using the following equation:

$$Q = RH \times Q_0 = 0.019\ g/g \times RH \tag{3.17}$$

After getting values for H_{SW}, H_L, H_S, $H_1 + H_2$ for each hour of each day, the trapezoidal method is used to integrate total short wave energy for a given day using 24 data points for each hour in the day in $\frac{J}{m^2}$. Daily change in water temperature is calculated using the specific heat formula and the measured energy,

$$\Delta T = \frac{-H}{C_{P,H2O}\rho_{H2O}\Delta z} \tag{3.18}$$

where H is the measured energy for the given day, $C_{P,H2O}$ is the specific heat of water $[\frac{J}{kg°C}]$, ρ_{H2O} is the density of water $[\frac{kg}{m^3}]$, and Δz is the water depth $[m]$. The water depth in the perimeter was estimated to be a constant 2 meters and the water depth in the estuary was varied from 1 to 10 meters during model calibration.

Current Conditions

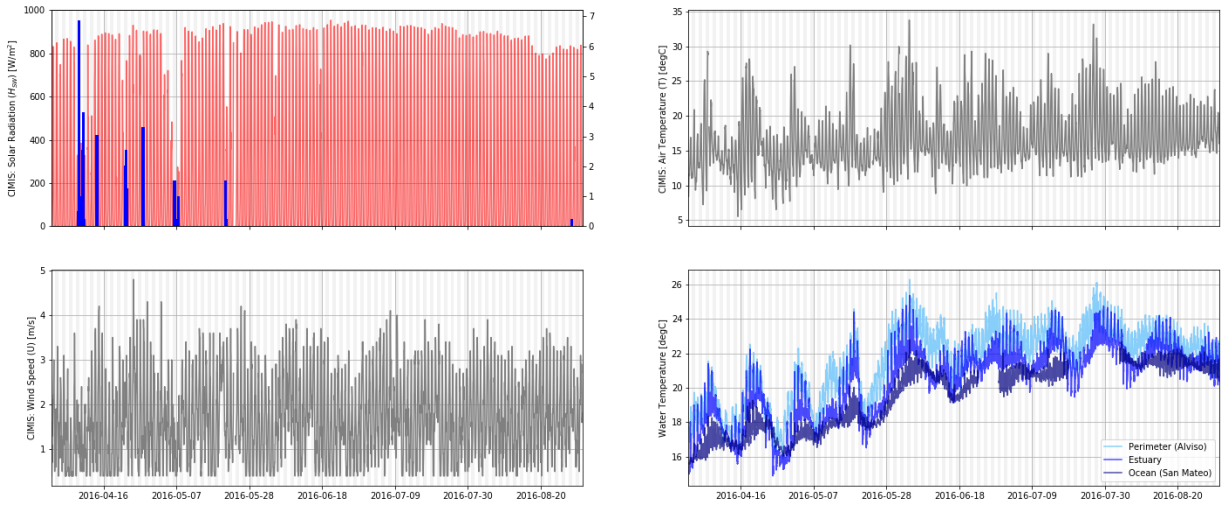

Figure 3.3: Measured conditions for the time window of interest. Top left figure shows measured solar radiation in $\frac{W}{m^2}$ along with hourly precipitation. Top right figure shows measured air temperature in degrees Celsius. Bottom left figure displays wind speed in $\frac{m}{s}$. Lastly, the bottom right figure shows measured water temperatures for the perimeter, estuary, and ocean control volumes. The perimeter water temperature is measured at Alviso and the ocean water temperature is measured at San Mateo. Refer to Figure 3.1 for a map of these locations.

Various measured atmospheric conditions are needed to estimate heating and cooling in a given water column with equations listed in Table 3.1. A summary of the solar radiation,

wind speed, and air temperature can be found in Figure 3.3. During the time windows studied in this analysis, there are drops in short wave radiation during storm events (Figure 3.3). Consistent wind speeds persist throughout the period of interest. Air temperature has a cyclic pattern in April and May 2016 most likely due to precipitation events.

The last panel in Figure 3.3 shows the measured temperatures for the ocean, estuary, and perimeter boxes that are to be modeled. Water temperatures warm in April and May with distinct cooling events that are perhaps triggered by precipitation. In June - August there are more consistent forcing conditions. The measured solar radiation and wind speed are constant during these months, however, there is still cyclical warming and cooling that occurs every 14 days. As expected, there is more variation in measured water temperature in the perimeter than the estuary, and there is more variation in the estuary than in the ocean. During cooling phases, the ocean temperatures can be warmer than the estuary and perimeter temperatures.

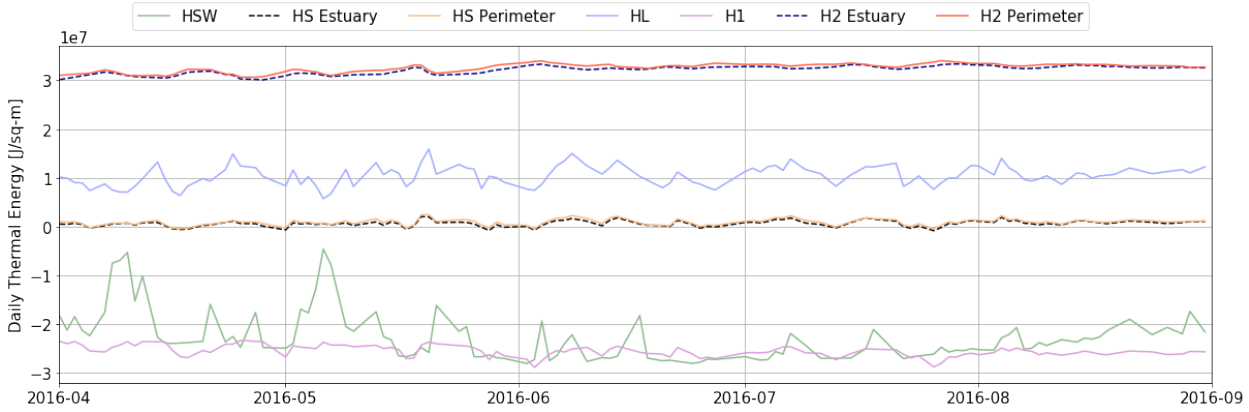

Figure 3.4: Thermal heating and cooling contributions from each variable in Table 3.1 where H_S is the sensible heat transfer, H_L is the heat loss due to evaporation, H_1 is the long wave radiation, H_2 is the back radiation from the water surface and H_{SW} is the short wave radiation that is directly measured from CIMIS. Variables H_S and H_2 are dependent on water surface temperature which varies for the estuary and perimeter. Estuary values of H_S and H_2 are shown by dashed lines. The values displayed in this figure show the daily thermal energy contributed to the estuary or perimeter control volumes from each H contributor. H in $\frac{W}{m^2}$ is converted to thermal energy in $\frac{J}{m^2}$ by integrating hourly calculations/observations of H-values over the entire day.

Real time water surface temperature is needed as an input to calculate change in water temperature due to sensible heat transfer, H_S, and back radiation from water surface, H_2. Since the measured current water temperature (T_0 in Table 3.1) is used for these variables, the model used in this chapter not entirely predictive. However breaking down the change in water temperature due to each component reveals H_S is not a major contributor to the change in water temperature, and H_2 is not very sensitive to varying values of T_0. Figure 3.4 shows that values of H_2 both in the estuary and perimeter are fairly constant throughout

this analysis meaning the variations in water surface temperature during this time window does not greatly change the magnitude of heating from the H_2 term. Selecting a constant value of water surface temperature, T_0, could have been used with similar results. Another option would be to use the water surface temperature in the previous time-step.

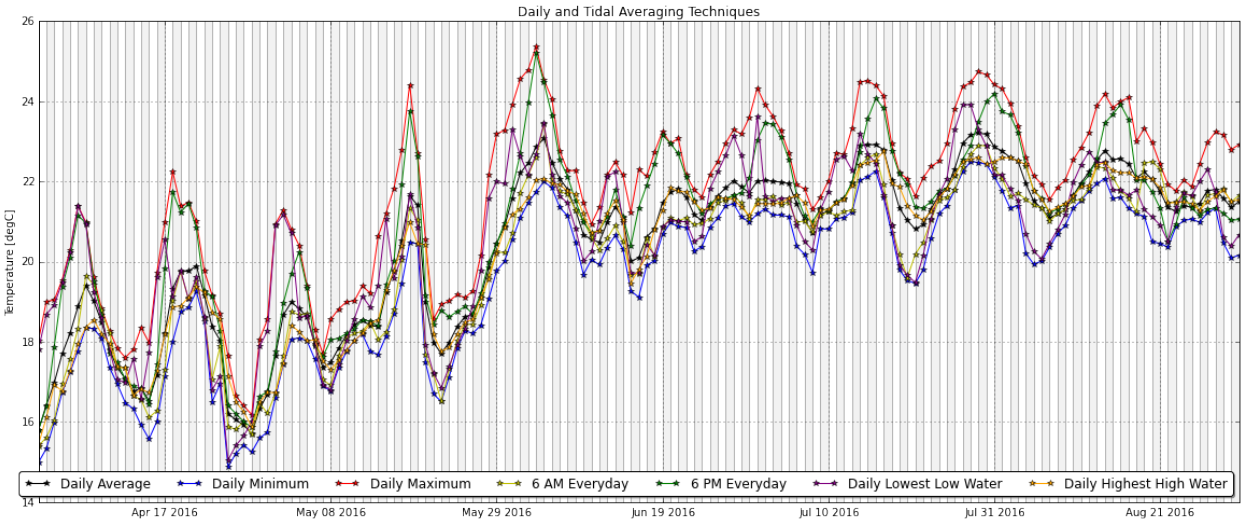

Figure 3.5: Varying techniques used to look at a single value to represent the daily temperature in the estuary. Time and tidal schemes were used including taking the daily average, taking the daily minimum, taking the daily maximum, taking the temperature that occurred at 6 AM on each day, taking the temperature that occurred at 6 PM on each day, taking temperature at the time the daily lowest low water level occurred, and taking the temperature at the time the daily highest high water level occurred.

When determining the measured total change in water temperature due to atmospheric forcing, there are many ways to represent the temperature in each control volume for a given day. With water temperature data on the order of 1-minute and 15-minutes, how do we represent the temperature in an estuary to determine heating and cooling trends? We looked into how different averaging schemes would influence the representative water temperature measurement daily. Figure 3.5 shows the comparison of water temperature time series using 1. daily average, 2. daily minimum temperature, 3. daily maximum temperature, 4. water temperature at 6 AM every day, 5. 6 PM every day, 6. water temperature corresponding to the time of daily lowest low water, and 7. water temperature corresponding to the time of daily highest high water. It was difficult to tease out trends due to tides and diurnal heating/cooling as well as determine if the cyclic variability in water temperature was due to the phasing of tides relative to the diurnal heating. By looking at varying averaging methods, both tidal and on the diurnal heating time scale, all time series of the estuary water temperature showed similar cyclic patterns in June - August, suggesting the cycle is due to fundamental forcing and not due to chosen averaging scheme.

Model Calibration

There are several variables that can be adjusted to fit the model to observed water temperature. The inputs needed for the model are ocean water temperature time series, T_o, initial estuary and perimeter water temperatures, $T_{e,0}$ and $T_{p,0}$, mixing coefficients, k_1 and k_2, and estuary and perimeter water depths.

Temperature Inputs

Initial estuary and perimeter water temperatures were assigned by the first measured temperatures in the estuary and in Alviso (perimeter) shown in Figure 3.3, $T_{e,0} = 15.8°C$ and $T_{p,0} = 17.9°C$. The observed ocean temperature is shown in the bottom right panel of Figure 3.3 (San Mateo). The observed ocean temperature is less variable than the estuary and perimeter temperatures, and seems to follow a step function with a cooler temperature in April and May and a warmer temperature from June - September. Model runs were completed for varying ocean temperature series. The model was first run with a constant ocean temperature of $20°C$ for the entire time. Then the model was run with an ocean temperature that followed a simple step function. The step function assigned an ocean temperature of $17.5°C$ from April 1 - May 31 and then a temperature of $21°C$ from June 1 - August 31. Lastly, the resolution of the ocean temperature was refined even further using a 5-day rolling average of the measured temperature at San Mateo.

When the ocean temperature was defined with a 5-day rolling average, there was little difference in the precision and accuracy of the modeled estuary and perimeter water temperature time series leaving little motivation to refine the ocean water temperature input farther than the step function that varies over the time window of months.

Mixing Coefficients

Diffusion coefficient, $K_{D,1}$, controls the exchange between perimeter and estuary. As $K_{D,1}$ increases, the residence time in the perimeter decreases and there is more exchange between the perimeter and estuary which is shown in time series plots by a decrease in the difference between the modeled estuary water temperature and modeled perimeter water temperature. The second diffusion coefficient, $K_{D,2}$, controls how much exchange occurs between the ocean and estuary. As $K_{D,2}$ is increased, the residence time in the estuary decreases and the estuary begins to act more like the ocean temperature time series. Often this meant the modeled estuary temperatures were brought down. When the ocean temperature was maintained at a constant, cold temperature, increasing $K_{D,2}$ would stifle the variability of the modeled estuary temperature and decrease the overall temperature.

In order to get an understanding of the model's sensitivity to adjustments of $K_{D,1}$ and $K_{D,2}$, a series of 63 runs with $K_{D,1}$ values of 0, 2, 10, 30, 40, 50, 70, 100, and 200 m^2/s and $K_{D,2}$ values of 30, 50, 60, 70, 80, 90, and 100 m^2/s were completed. These values were selected to span a wide range of coefficient values. For lengths of estuary, perimeter, and

RSME Estuary

KD,1→ / ↓KD,2	0	2	10	30	40	50	70	100	200
30	1.089	1.284	1.526	1.525	1.502	1.478	1.435	1.383	1.277
50	0.766	0.631	0.692	0.729	0.732	0.732	0.731	0.729	0.727
60	0.862	0.695	0.692	0.73	0.738	0.744	0.753	0.764	0.786
70	0.966	0.804	0.774	0.806	0.816	0.823	0.836	0.851	0.882
80	1.058	0.91	0.869	0.896	0.906	0.914	0.927	0.943	0.975
90	1.137	1.001	0.958	0.981	0.99	0.997	1.01	1.026	1.057
100	1.203	1.08	1.036	1.056	1.064	1.071	1.083	1.098	1.128

RSME Perimeter

KD,1 → / ↓KD,2	0	2	10	30	40	50	70	100	200
30	43.163	24.642	8.077	3.191	2.535	2.136	1.677	1.337	0.982
50	43.163	24.002	6.973	2.129	1.551	1.246	0.997	0.948	1.102
60	43.163	23.839	6.693	1.874	1.339	1.092	0.963	1.027	1.279
70	43.163	23.721	6.491	1.697	1.206	1.016	0.989	1.124	1.424
80	43.163	23.632	6.339	1.569	1.121	0.984	1.034	1.214	1.541
90	43.163	23.563	6.221	1.473	1.065	0.975	1.083	1.292	1.636
100	43.163	23.508	6.126	1.398	1.028	0.979	1.13	1.359	1.713

RSME Combination

KD,1 → / ↓KD,2	0	2	10	30	40	50	70	100	200
30	11.607	7.123	3.164	1.942	1.76	1.643	1.496	1.371	1.203
50	11.365	6.474	2.262	1.079	0.936	0.86	0.797	0.783	0.821
60	11.437	6.481	2.192	1.016	0.888	0.831	0.806	0.83	0.909
70	11.515	6.533	2.203	1.029	0.913	0.872	0.874	0.919	1.017
80	11.584	6.59	2.237	1.065	0.959	0.931	0.954	1.011	1.117
90	11.643	6.642	2.274	1.104	1.008	0.992	1.029	1.092	1.202
100	11.693	6.687	2.309	1.141	1.055	1.048	1.095	1.163	1.275

Figure 3.6: Root mean square error modeled versus observed for $K_{D,1}$ ranging from 0 to 200 m^2/s and $K_{D,2}$ ranging from 30 to 100 m^2/s. The length of the estuary, perimeter, and ocean is set to 6440 meters, 2250 meters, and 12,870 meters respectively. Depth of the estuary, perimeter, and ocean is 2 meters, 2 meters, and 15 meters. The first table contains RMSE for modeled versus observed temperature time series in the estuary. The second table is for perimeter comparisons. The last table is a weighted average of the estuary, perimeter RMSE values (weight by volume, 75% estuary, 25% perimeter). The model is run from May 29, 2016 to August 1, 2016 with $C_{P,H_2O} = 4186\ \frac{J}{kg\ degC}$, $\rho_{H_2O} = 1000\ \frac{kg}{m^3}$, estuary depth = 2 m, perimeter depth = 2 m.

ocean of 6440 meters, 2250 meters, and 12,870 meters, $K_{D,1}$ and $K_{D,2}$ correspond to flushing times summarized in Table 3.2.

Figure 3.6 shows the root mean square error (RMSE) in the estuary, in the perimeter, and a weighted RMSE. The RMSE represents the difference between the modeled temperature and the observed temperature for a given time. Better fits have smaller RMSE values and

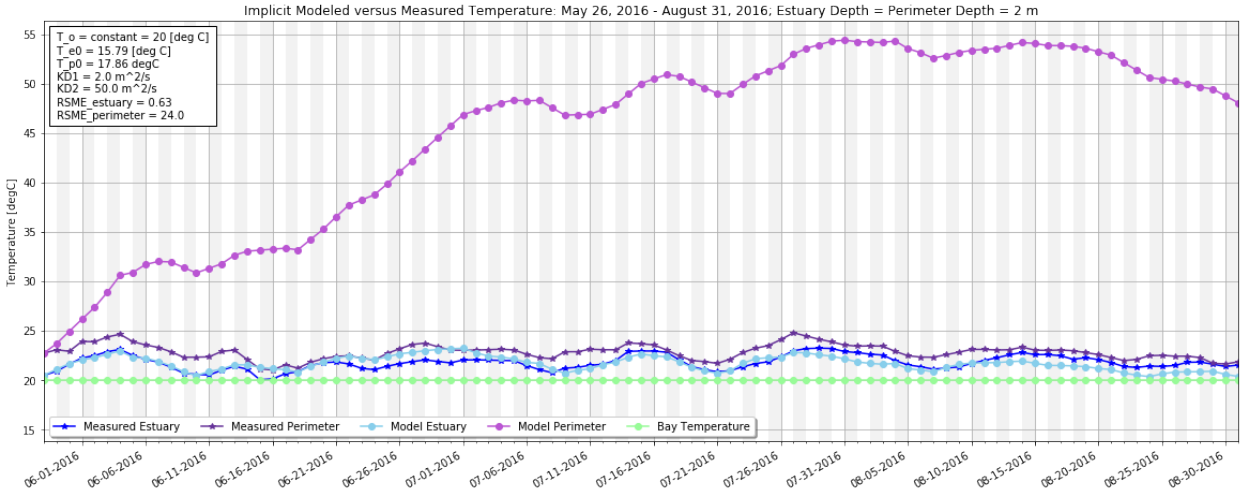

Figure 3.7: Modeled versus measured estuary and perimeter temperatures using $K_{D,1} = 2\ m^2/s$, $K_{D,2} = 50\ m^2/s$. Model was run for temperatures beginning May 26, 2016 and ending August 31, 2016 with an initializing estuarine temperature of 15.8 degrees Celsius, initial perimeter temperature of 17.9 degrees Celsius, and a constant ocean input temperature of 20 degrees Celsius.

$K_{D,1}$	$T_{perimeter}$	$K_{D,2}$	$T_{estuary}$
m^2/s	days	m^2/s	days
0	infinity	30	36
2	109	50	21.6
10	21.85	60	18
30	7.28	70	15.4
40	5.46	80	13.5
50	4.37	90	12
70	312	100	10.79
100	2.19		
200	1.09		

Table 3.2: Corresponding residence times to values of $K_{D,1}$ and $K_{D,2}$. Calculated by equations 3.13 and 3.14.

worse fits will have larger RMSE values. When looking at how well each model captured the temperature time series in the estuary, the best fit occurred when $K_{D,1} = 2\ m^2/s$ ($T_{perimeter} = 109$ days) and $K_{D,2} = 50\ m^2/s$ ($T_{estuary} = 21$ days). However, the perimeter temperature is better modeled when $K_{D,1} = 100\ m^2/s$ ($T_{perimeter} = 2$ days) and $K_{D,2} = 50\ m^2/s$ ($T_{estuary} = 21$ days). Figure 3.7 shows the temperature time series comparison of modeled versus measured when we use the fit with the best match for the estuary, $K_{D,1} = 2\ m^2/s$ ($T_{perimeter} = 109$ days) and $K_{D,2} = 50\ m^2/s$ ($T_{estuary} = 21$ days). While the model

does a good job capturing the fluctuations in the estuary, the modeled perimeter temperature overheats and remains 25-30 degrees Celsius above the measured.

Since the volume of the estuary is greater than the volume of the perimeter, in order to determine a combined RMSE, the estuary RMSE is weighted more heavily than the perimeter RMSE. By using the geometric dimensions defined in Figure 3.6, the volumetric ratio of estuary to perimeter becomes 75:25. The best fit for the combined RMSE is the same $T_{perimeter}$, $T_{estuary}$ combination as the best fit for the perimeter, $T_{perimeter} = 2$ days and $T_{estuary} = 21$ days.

It should also be noted that the success of the model at capturing the estuary temperature time series is more sensitive to changes in $K_{D,2}$ than changes in $K_{D,1}$, or the RMSE increases more drastically to changes in $K_{D,2}$ than in $K_{D,1}$. When keeping $K_{D,2} = 50\ m^2/s$, adjusting $K_{D,1}$ anywhere between 0 to 200 m^2/s varies the RMSE from a minimum of 0.63 degrees Celsius to 0.76 degrees Celsius for the temperature time series in May 29, 2016 through August 1, 2016. Therefore, the RMSE of the observed versus modeled estuary temperature is not very sensitive to changes in $K_{D,1}$ compared to changes in $K_{D,2}$.

Best Fit for April 1 - August 31, 2016

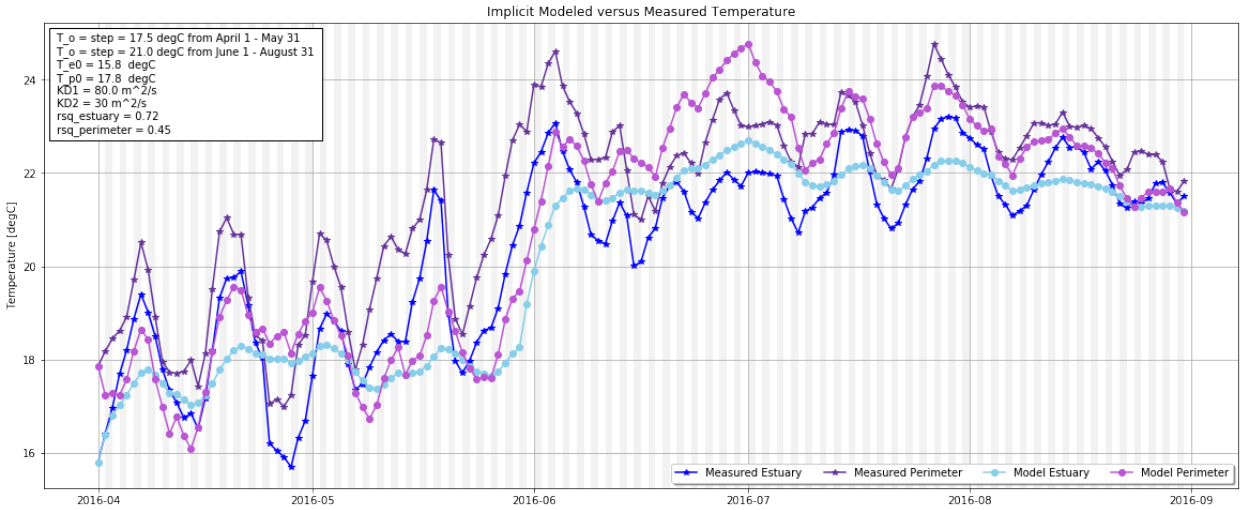

Figure 3.8: Step ocean temperature input where $T_o = 17.5$ deg C April 1 - May 31 and $T_o = 21$ deg C June 1 - August 31, perimeter water depth of 2 meters, estuary water depth of 10 meters. $K_{D,1} = 100\ m^2/s$, $K_{D,2} = 50\ m^2/s$. Model was run for temperatures beginning April 1, 2016 to August 31, 2016. The initial estuary temperature is set to 15.8 deg C and the initial perimeter temperature is set to 17.8 deg C.

Figure 3.8 shows measured and modeled estuary and perimeter temperatures for a step function ocean water temperature input. When $K_{D,1} = 80\ m^2/s$ and $K_{D,2} = 30\ m^2/s$, the modeled estuary and perimeter time series follows the observed time series reasonably well

(R^2 for the estuary is 0.72, R^2 for the perimeter is 0.45). In the months of April and May, there are four distinct cooling events of which the model is able to capture three. When looking closely at the solar radiation during these times, there is a drop in the measured solar radiation during all of these cooling events except for the second, which corresponds to the cooling event not captured by the model, which means the measured solar radiation is incorrect or there is another source of cooling not taken into account by the model. The modeled perimeter and estuary time series have similar differences to the observed and the timing of the warming and cooling is well captured by the model.

Estuary Depth

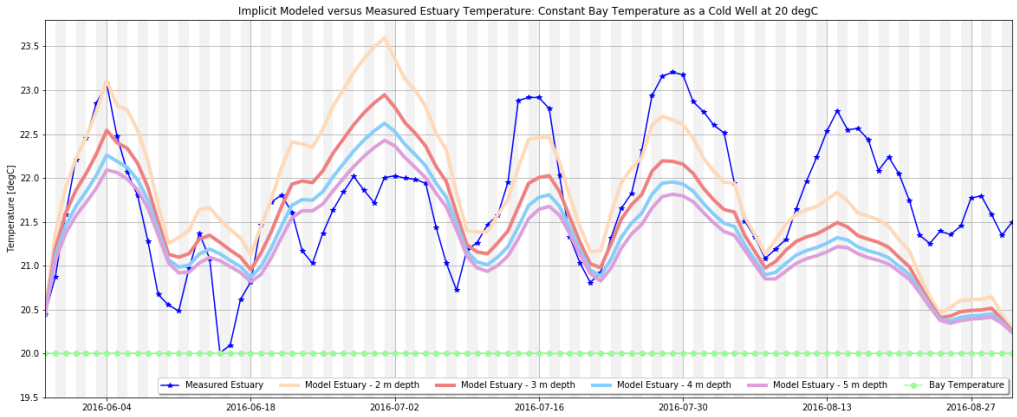

Figure 3.9: Constant ocean temperature input of 20 deg C, perimeter water depth of 2 meters, varying estuary water depth of 2 meters, 3 meters, 4 meters, and 5 meters

Lastly, the estuary and perimeter water depths can vary to adjust the model outputs. Figure 3.9 shows when the estuary depth is decreased, the variability of the modeled estuary temperature increases. When the estuary depth was adjusted to 2 meters, temperature variability was closest to the observed.

Sensitivity to Length and Depth Selection

It is difficult to confidently select one length and depth value to represent each of these systems. Channels within estuaries may curve making a straight length from point A to point B length analysis inaccurate. Depths within each system, the estuary, ocean, and perimeters, may be spatially variable, making it difficult to know what depth to choose to represent the entire volume. To get a better understanding of how adjustments in lengths affect the residence time, a sensitivity analysis was conducted with results summarized in Figure 3.10. For this sensitivity analysis, it is assumed that changes in L_e, H_e, L_p, H_p, L_o,

$T_{perimeter}$, original	2.19 days	$T_{estuary}$, original	21.58 days	
Adjustment			$T_{perimeter}$	$T_{estuary}$
$L_{estuary}$	→	8050 meters	3.06 days	25.3 days
(originally 6440 m)	→	12,870 meters	6.61 days	38.3 days
$L_{perimeter}$	→	480 meters	1.39 days	no change
(originally 2250 m)	→	4500 meters	3.46 days	no change
L_{ocean}	→	6440 meters	no change	9.6 days
(originally 12,870 m)	→	26,000 meters	no change	61 days

Figure 3.10: In order to determine the sensitivity of selected lengths plugged into equations 3.13 and 3.14, this figure shows how adjustments in the length of estuary, length of perimeter, and length of the ocean affects the final residence times for a given $K_{D,1} = 100\ m^2/s$ and $K_{D,2} = 50\ m^2/s$. Only one value was adjusted for each calculation in order to understand the sensitivity of $T_{perimeter}$ and of $T_{estuary}$ to that variable. Original values used to calculate $T_{perimeter,\ original}$ and $T_{estuary,\ original}$ are $L_{estuary} = 6440$ meters, $L_{perimeter} = 2250$ meters, $L_{ocean} = 12,870$ meters.

and H_o will not have a large affect on the best fit $K_{D,1}$, $K_{D,2}$ values. This eliminates the need to redo the analysis completed in Figure 3.6 for every change in L or H. To understand how residence time is affected by changes in L_e, L_p, and L_o, this sensitivity analysis takes the best fit K_D values from Figure 3.6 ($K_{D,1} = 100\ m^2/s$, $K_{D,2} = 50\ m^2/s$).

The original case was taken to be the analysis of residence time from section 3.3 which gave a perimeter residence time of 2.19 days and an estuary residence time of 21.6 days. Adjustment of the length of estuary showed that when the length of the estuary was doubled from 6440 meters to 12,870 meters, the perimeter residence time increases to 6.6 days. Adjustments to the perimeter length did not affect the residence time calculation between the estuary-ocean ($T_{estuary}$) and adjustments to the length of the ocean did not affect the calculated residence time between the perimeter-estuary ($T_{perimeter}$). Even adjustments that double the length of the perimeter keep residence time in the perimeter on the same order of magnitude of a few days. However, when doubling the length of the ocean, the residence time in the estuary goes from an order of 3 weeks to an order of 2 months.

The residence time calculations are most sensitive to the length of the ocean. These differences have implications when determining mass balances, nutrient budgets, and occurrence of harmful algal blooms. Likewise, if the length or depth of the ocean is larger in volume, the residence time in the estuary would increase.

3.3 Results

Exchange Rates

Adjustments on the ocean temperature input, mixing coefficients, and estuary depth were made to capture the magnitude and variability of observed estuary and perimeter water temperatures from May 26, 2016 through August 31, 2016. No amount of adjustment to $K_{D,1}$ and $K_{D,2}$ resulted in resolving the second cooling event that occurs at the end of April and the beginning of May shown in Figure 3.8. In order to remove unaccounted for factors in the model, the second half of the time series (May 26 - August 31) was used to determine exchange rates between the estuary and perimeter. By looking at the second half, the step-input ocean temperature dependency is removed and the unresolved cooling event is not taken into account. Based off of the sensitivity analysis completed, the combination of $K_{D,1}$, $K_{D,2}$ with the lowest combined RMSE was $K_{D,1} = 100\ m^2/s$, $K_{D,2} = 50\ m^2/s$. Figure 3.11 shows the results of the model in comparison to observed.

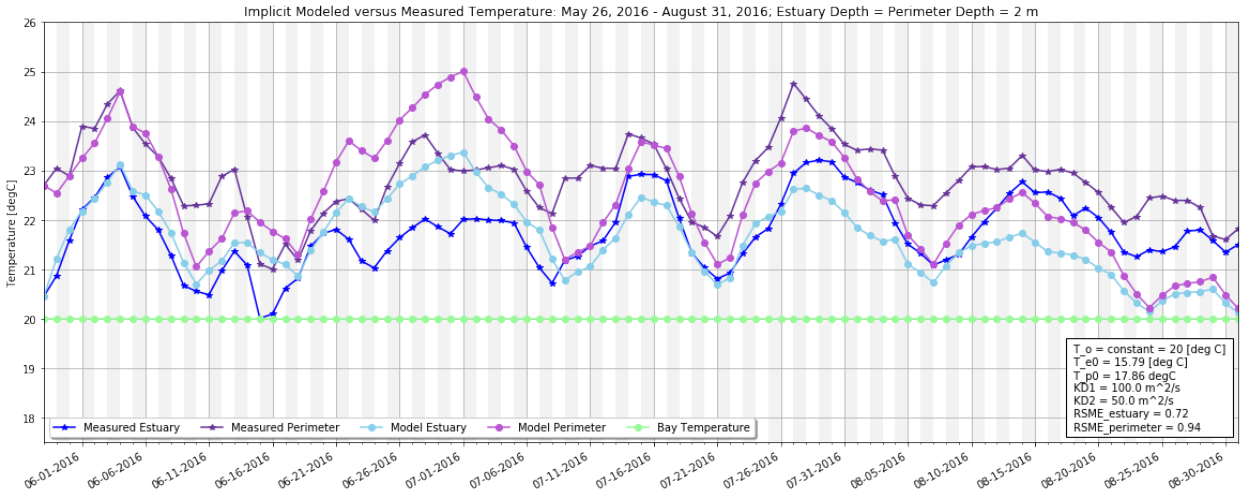

Figure 3.11: Implicit modeled versus measured estuary and perimeter temperature beginning May 26, 2016. Estuary and perimeter depth is set to 2 meters. $K_{D,1}$ is set to 100 m^2/s and $K_{D,2}$ is set to 50 m^2/s .

In order to get an estimate of the residence time in the perimeter and in the estuary for Lower South San Francisco Bay, lengths between each of the measurements were estimated to be 6400 meters, 2200 meters, and 12,870 meters for the lengths of the estuary, perimeter, and ocean respectively by measuring on a map. The water depths were estimated to be 2 meters (to match the depth used for the model), 2 meters (to match the depth used for the model), and 15 meters for the water depth in the estuary, perimeter, and ocean respectively. Using these values, the model diffusion coefficients, $K_{D,1}$ and $K_{D,2}$ can be converted residence times using equations 3.13 and 3.14:

$$T_{perimeter} = \frac{[\frac{1}{2}(6400\ m + 2200\ m)]^2}{K_{D,1}} \rightarrow K_{D,1} = 100\ m^2/s \rightarrow T_{perimeter} = 2.19\ days \quad (3.19)$$

$$T_{estuary} = \frac{[\frac{1}{2}(6400\ m + 12870\ m)]^2}{K_{D,2}} \rightarrow K_{D,2} = 50\ m^2/s \rightarrow T_{estuary} = 21.6\ days \quad (3.20)$$

Therefore, by using the model outputs of mixing coefficients between the estuary control volume with the perimeter and ocean control volumes, we can estimate a residence time for Lower South San Francisco Bay. According to our estimates, the residence time for Lower South San Francisco Bay is on the order of 3 weeks.

A residence time of 2 days in the perimeter and 21 days in the estuary is relatively short when compared to the estimated 120-300 day residence time in the Chesapeake Bay [51]. This means if a pollutant were introduced into LSSFB, it would only remain in the estuary for about 3 weeks. These hydrodynamic factors surely play a significant role in the absence of seasonal phytoplankton blooms [29]. As climate changes, this residence time could increase especially under low river flow conditions with strong upstream winds.

3.4 Discussion

Other methodology used to estimate residence time in estuarine literature

Estimations of residence time or some quantity to describe the time a passive tracer remains in an estuary have been well documented in the literature. Observations and models have been used to estimate residence times in estuaries such as the Mersey estuary, Chesapeake Bay, and the Hudson River estuary [7, 27, 51, 18].

Geyer et al. (2007) used fluoroscein dye in the Hudson River estuary but was confronted with several factors making it difficult to determine the residence time [18]. The fluoroscein dye used has a rapid photo-decay rate making it difficult to capture near-surface fluxes. It is also difficult to recover the total mass of released dye, they underestimated the mass by almost 40% on average. This discrepancy could be due to a systematic calibration error or an incomplete survey of the dye patch [18]. They found that the resulting magnitude of along-estuary dispersion in a shear flow is very sensitive to the vertical extent of the dye. When doing dye experiments in the field, there are difficulties with equipment limitations as well. Typically the deployment is set up with one boat that measures observations in the along-channel and across-channel as it drives by making it difficult to get a single snapshot in time. However, dye-observation based estimates of residence time is relevant because it is directly measured. These experiments allow for spatial and temporal adjustments allowing the deployment designer to see how dispersion rates change when in different tidal phases,

different seasons, different river outputs, etc. Dye may also be released from different inputs into the estuary allowing for further understanding of spatial variation.

Models can serve to fill in data gaps both in space and in time. Models allow users to adjust variables to see how each affects the residence time. The success of estimating residence time from numerical models depends greatly on the hydrodynamic transport model which relies on model calibration and verification based on limited spatial and temporal observational data [51]. In 2007, Shen found that their model of the Chesapeake Bay without wind forcing substantially decreased the age of water [51], therefore emphasizing the importance of capturing the influence of wind in an estuary in order to obtain a correct residence time estimation. In 1997, Geyer found that in a shallow estuary, the residence time can vary by more than a factor of 3 in response to variations in wind [17]. Therefore, sensitivities to variables such as wind may present challenges for locations that have limited observational data to calibrate the model.

Using temperature to estimate residence time

The methodology presented in this chapter uses temperature gradients to estimate residence time in the perimeter and in the estuary. The use of this method is advantageous for estuaries where it is difficult to obtain salinity measurements with proper spatial and temporal resolution to estimate residence time or for estuaries without well-calibrated models. Since water temperature is of interest to a variety of fields, measurements are commonly collected and are publicly available online making this method accessible. It does not require a large start-up time like complex 3-dimensional models or costly oceanographic equipment to take in situ measurements. However, from literature it is clear that residence time has spatial and temporal variability. This method is limited in that it only allows for spatial/temporal variability when splitting time series or with increasing number of boxes. With every additional box added, an additional mixing coefficients must be resolved adding complexity to fit modeled to observed time series. For the box set up used in this chapter, there are only two estimates of exchange for the estuary. If one has temperature measurements in varying locations in the estuary of interest, each probe could be its own control volume with its own diffusion coefficient, K_D, allowing for additional spatial variation.

Typically, salinity has been used in models and from observed data to estimate estuarine exchange. In estuarine environments, mixing is dominated by salinity rather than temperature variance, therefore leading estuarine researchers to use the salinity variance equation for addressing mixing in estuaries [31]. In this chapter, temperature is used to estimate exchange rates leading to a total residence time on the order of 3 weeks in LSSFB. In chapter 4 when the recovery of salinity after a precipitation event was used to estimate residence time, the residence time was found to be on the order of two weeks. In these methods, longitudinal gradients of salinity or temperature are used to infer the dynamics in LSSFB. Salinity gradients are formed through freshwater inputs which tend to be more spatially varying as freshwater inputs come in through point-river sources. Therefore, longitudinal salinity gradients may vary greatly depending on distance to the freshwater input point

source. Temperature gradients are formed through atmospheric heating and cooling and is not as point dependent. Perhaps this differentiation in the spatial variability of the source of buoyancy versus atmospheric heating and cooling causes these tracers to give different residence times for the same estuary.

Residence time is dependent on freshwater input, but if buoyant exchange dominates the up-estuary transport of salt, an increase of freshwater input would decrease the residence time [2]. Since the estimated residence time from chapter 4 has larger precipitation rates, it makes it more difficult to attribute the variation in estimated residence time to the variation of freshwater input.

Figure 3.7 revealed that in order to get the modeled estuary to fit observed using temperature, the perimeter had to be grossly exaggerated providing more heat to the estuary than measured suggesting the model is missing some sort of heat input or an error in the assumptions. One error that could be affecting the error between the model and observed temperatures could be from the CSTR assumption in each box. When separating the estuary into one control volume, spatial variation is lost within that box which could resolve the error. Sensitivity analysis also revealed the dependence on volume choice of each control volume (Figure 3.10). Determining the volume of the ocean control volume is subjective as the ocean is an infinite, constant source of temperature being inputted into the estuary.

3.5 Conclusions

In this chapter, water temperature time series from three locations in Lower South San Francisco Bay is used to model the exchange of water between an ocean, estuary, and perimeter. By using a simple three box model with two mixing coefficients the model captured the magnitude and fluctuation of temperature in LSSFB and its perimeter. Using the model, residence time was found to be on the order of 2 days in the perimeter and on the order of 3 weeks in the estuary. By understanding how much time a water parcel spends in Lower South San Francisco Bay, scientists apply it to mass balances, nutrient budgets, and models of future algal blooms which could lead to future policy decisions. Limitations arise from the assumption that temperatures are homogeneous inside each box of the model. This assumption will likely cause an underestimate of the residence time, but this alternative method of calculating residence time can help provide estimates in water bodies that have limited salinity data. This method can also be used in conjunction with other methods to get another estimate as each method has its own set of limiting assumptions. For future work, this method can be applied to estuaries with estimates of residence time using alternative methods in order to compare this temperature-based method to salinity-based methods.

Chapter 4

Seasonal Variability in Lower South San Francisco Bay

4.1 Introduction

Estuaries are embayments along the coast that have a source of dense ocean water and a source of freshwater typically from river discharge or land runoff. There is constant creation of stratification through input of a buoyant, freshwater source and destruction of stratification from tidal mixing. Estuaries have several time scales that affect the physical dynamics of the system. An estuary experiences a flood and ebb tide which is caused by forcing from the sun and moon. Each day there are two flood tides and two ebb tides, and the spring-neap tidal cycle occurs on a 2 week time scale. Lastly, buoyancy input varies on a seasonal time scale as it is highly dependent on rainy and drought seasons in Mediterranean climates. In San Francisco Bay, the winter months (November - March) are characterized with large and frequent rainfall events and lower air temperatures while the summer months (April - October) have little to no rainfall and higher air temperatures (Figure 4.1).

In summary, five different time scales that contribute to the temperature, salinity, and stratification patterns in an estuary are

1. Tidal (M2 = 12.4 hours): Flood/ebb; hydrodynamic straining/advection
2. Daily: Asymmetry in flood/ebb tides in a given day; heating and cooling cycle in a given day
3. Spring-Neap (twice monthly): Variation in the amplitude of water velocities
4. Seasonal (year): Variation in rainfall and ambient air temperature
5. Decadal: Climate changes

Tidal patterns of stratification result in estuarine circulation with seaward driven shallow waters and landward driven deep waters [22]. There has been interest in the stratification

patterns in Lower South San Francisco Bay due to the high levels of nutrients from wastewater outputs and the decreasing turbidity. Scientists wonder if the changing climate, the clearing bay, and the high levels of measured nitrogen and phosphorous will lead to reoccurring toxic algal blooms. When light is no longer the limiting factor, the phytoplankton can thrive in the upper water column during periods of stratification [29].

We have collected a unique data set of velocity, salinity, and temperature measurements inside the center channel of Lower South San Francisco Bay. The data spans almost a year and a half allowing insight as to how salinity and stratification patterns are affected on a seasonal timescale. Chapter 2 looked in detail how salinity and stratification varied on a tidal timescale. The goal of this chapter is to understand how the salinity, stratification, and temperature in Lower South San Francisco Bay respond to varying precipitation and atmospheric conditions on a seasonal time scale.

4.2 Deployment Site

San Francisco Bay is a meso-tidal estuary characterized by strong diurnal inequalities that vary with the spring-neap cycle. This dissertation focuses on a sub-estuary of San Francisco Bay, Lower South San Francisco Bay (LSSFB), which extends roughly 10 km landward from the Dumbarton Narrows to the head of the estuary in Coyote Creek. In LSSFB, the bathymetry consists of a central, curving channel with broad shoals on either side extending to perimeter marshes that are connected to the Bay through tidal sloughs. Freshwater from rainfall is typically observed from November to March with little to no rainfall inputs from April to October. The goal of this data collection was to observe seasonal salinity patterns along with system responses to rainfall events in LSSFB.

There have been studies on the tidal variation of stratification in LSSFB and in other regions of San Francisco Bay. In 2012, Collignon looked at the frontal features and lateral circulation dynamics in South San Francisco Bay on a tidal time scale [12]. Observational data in the North San Francisco Bay gave insight into how lateral dynamics affect the tidal patterns of vertical density stratification [25]. Chapter 2 looked in detail at the longitudinal versus lateral hydrodynamics that shaped the tidal stratification pattern in LSSFB. This chapter will focus on the observed seasonal variation over the 1.5 year data set.

4.3 Equipment Deployed

In order to study seasonal salinity patterns, Ruskin RBR XR-420 CTDs and Seabird SBE-37's were placed in a central location within a channel in LSSFB. A line containing top, middle, and bottom CTDs was deployed near U.S. Geological Survey's (USGS) channel marker 17 (*37.47798, -122.07658*). The location of this line will be referred to as CM17 throughout this chapter. This line was strategically placed in the channel near the center of LSSFB, equidistant to the mouth of the estuary and to the opposing perimeter. The

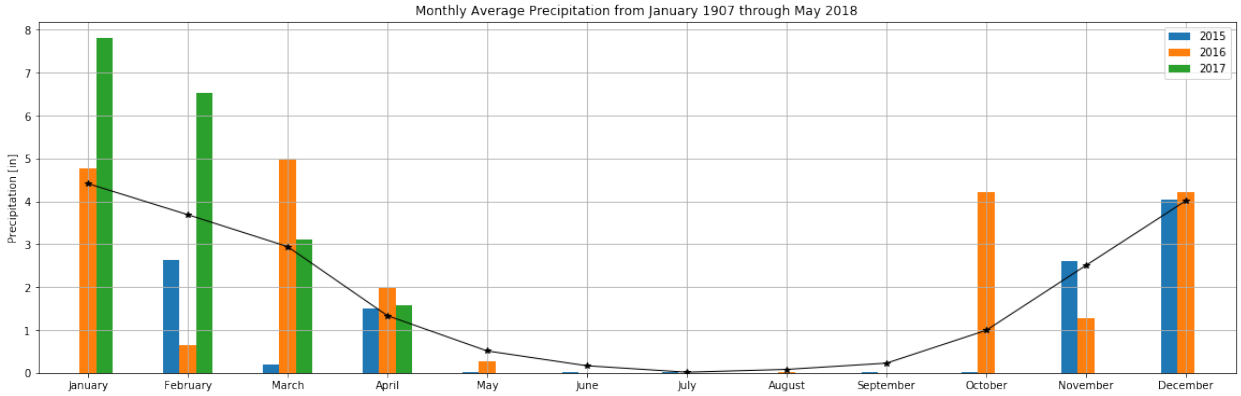

Figure 4.1: Monthly precipitation sums from San Francisco Downtown Station (RG31) Data from 1907 - 2018. Bar graphs display the monthly sum of precipitation in inches at Union City from Table 4.4. Note: Monthly precipitation is available from January 2015 - April 2017.

RBRs and Seabirds measured conductivity, pressure (depth), and temperature, and calculated salinity, at one minute intervals. The RBR XR-420 CTDs (Seabird SBE 37s) have a temperature accuracy of $\pm 0.002°C$ ($\pm 0.002°C$) and pressure accuracy of 0.05% (0.1%) [45, 48].

Teledyne RD Instruments (RDI) 1200 kHz Workhorse Monitor Acoustic Doppler Current Profilers (ADCP) were deployed during three deployments (refer to Table 4.1 for deployment summaries). ADCPs were tethered to the CTD lines by a bottom cable. The moored ADCPs were programmed to measure over a 12 meter water column with a vertical resolution of 0.25 meters with the first bin located 0.81 meters from the sea floor. The ADCPs, like the RBRs and Seabirds, collect ensemble averages every minute.

Table 4.1 shows each deployment's start dates and what equipment was deployed. Conductivity measurements were susceptible to biofouling, so measured conductivity/salinity had to be cut short to truncate unreliable data. Biofouling was recognized in conductivity time series by rapid changes in salinity not tied to tidal or other physical forcings. Conservative end dates of reliable measured conductivity are listed in Table 4.1. Temperature, pressure (depth), and velocity sensors were not affected by biofouling, so these measurements span the entirety of September 9, 2015 to February 15, 2017 with short windows between each deployment for the cycling of lines. Water column velocity profiles were collected by ADCPs in three deployments (September 2015, February 2016, and January 2017).

4.4 CIMIS and SFEI Moored Sensors

Additional data was sourced from California Irrigation Management Information System (CIMIS) and San Francisco Estuary Institute (SFEI) to get a more holistic understanding of the system during the deployment window from September 2015 - February 2017.

Deployment		CTD at CM 17			ADCP
Start Date	**Conductivity End Date**	**Top**	**Middle**	**Bottom**	
September 9, 2015	October 3, 2015	X	X	X	X
December 9, 2015	January 31, 2016	X	X	X	
February 11, 2016	March 12, 2016	X	X	X	X
April 14, 2016	May 2, 2016	X	X	X	
June 10, 2016	June 24, 2016	X	X	X	
August 19, 2016	August 30, 2016	X	X	X	
October 13, 2016	November 10, 2016		X	X	
January 4, 2017	February 14, 2017	X	X	X	X
February 15, 2017	RECOVER ALL				

Table 4.1: Deployment overview at channel marker 17 (CM17) (*37.47798, -122.07658*). Note: Temperature, depth, and velocity data is available from the start of each deployment to the start of the following deployment with a small data gap due to the recovery and redeployment time. These sensors were not affected by biofouling like the conductivity sensor.

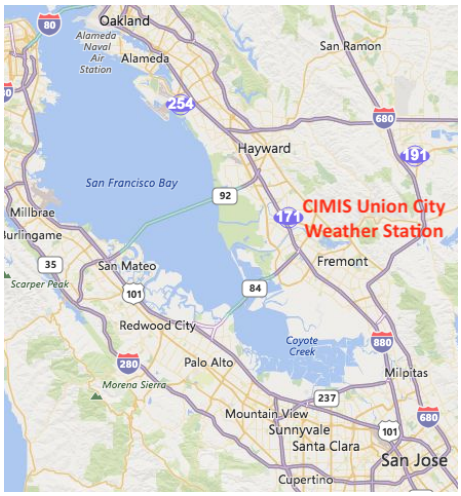

Figure 4.2: CIMIS weather station location: Union City No. 171.

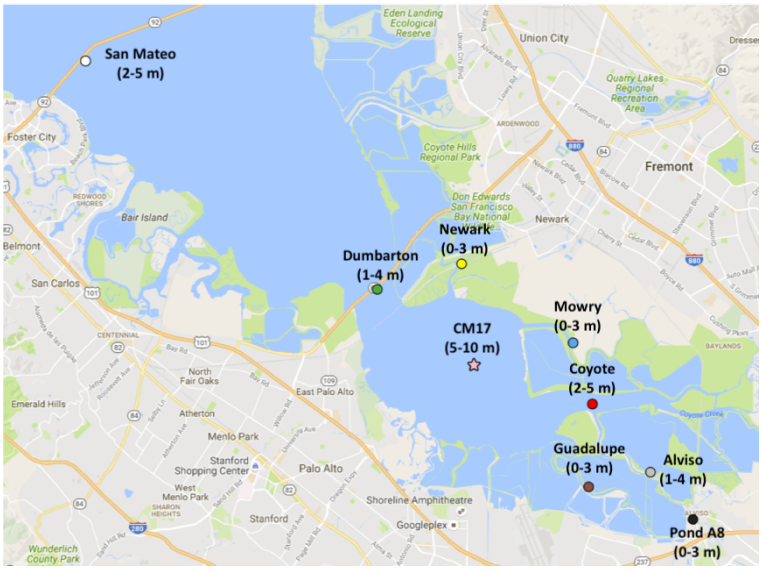

Figure 4.3: SFEI nutrients program deployment locations and depth of sensors

Name	Latitude	Longitude
CM17	37.47798	-122.07658
San Mateo	37.584446	-122.24889
Dumbarton	37.504166	-122.11945
Newark	37.513382	-122.0821
Mowry	37.485355	-122.03274
Guadalupe	37.434673	-122.02575
Coyote	37.463844	-122.02417
Alviso	37.44	-121.99834
Pond A8	37.423477	-121.97954

Table 4.2: Locations of SFEI nutrients program sensors corresponding with Figure 4.3 [60]

CIMIS stations collect weather data on a minute-by-minute basis at various locations in California. Calculated parameters (such as ETo, net radiation, and dew point temperature) and measured parameters (such as solar radiation, air temperature, relative humidity, and wind speed) are recorded online in the CIMIS database for unlimited, free access by registered CIMIS data users [58]. The closest CIMIS weather station to LSSFB is the Union City station No. 171 located at *37.598758, -122.05323* (Figure 4.2). CIMIS data at Union City include timestamps every hour, ETo (mm), precipitation (mm), solar radiation (W/m^2), vapor pressure (kPa), air temperature (degrees Celsius), relative humidity (%), dew point (degrees Celsius), wind speed (m/s), wind direction (degrees), and soil temperature (degrees Celsius).

The National Oceanic and Atmospheric Administration (NOAA) developed the Environ-

Name	Habitat	Depth
CM17	Open Channel	5-10 m
San Mateo	Open Channel	2-5 m
Dumbarton	Open Channel	1-4 m
Newark	Slough	0-3 m
Mowry	Slough	0-3 m
Guadalupe	Slough	0-3 m
Coyote	Creek/Slough Confluence	2-5 m
Alviso	Slough	1-4 m
Pond A8	Constructed channel	0-3 m

Table 4.3: Habitat and water depths of SFEI nutrients program corresponding with Figure 4.3 [60]

mental Research Division Data Access Program (ERDDAP) for oceanographic data. This online database makes it easy to access and download SFEI Nutrients Program's observed data providing additional salinity and temperature data at various locations in the perimeter of LSSFB [37]. Figure 4.3 shows where salinity and temperature measurements were collected at CM17 with a pink star along with additional locations collected by SFEI. The remainder of this section provides site details of each SFEI line [60].

The **San Mateo Bridge** measurements provide conditions of the South Bay open channel. It is the northernmost site at approximately nine miles north of the Dumbarton Bridge. There is a floating SeaBird HCEP pre-October 2016 and a moored line with a SeaBird HCEP 1.9 meters above bed (m.a.b.) post-October 2016. At this location, there are high levels of fouling and rough surface waters. Measurements are collected at depths ranging from 2-5 meters.

The **Dumbarton Bridge** is similar to the San Mateo Bridge in that it is an open channel habitat that experiences high levels of fouling as well as rough surface waters. The Dumbarton Bridge measurements provides insight of the conditions of the water entering Lower South San Francisco Bay. At this location there is one moored YSI EXO2 at 1.2 m.a.b. within the deep channel. Sensor depths range from 1-4 meters.

Newark provides slough data that is not connected to salt ponds nor does it receive publicly owned treatment works input. There is a moored YSI EXO2 at 0.9 m.a.b. post-August 2016 and 1.2 m.a.b. pre-August 2016. Sensor depths range from 0-3 meters.

Mowry is a slough habitat that is located downstream of a confluence of two side channels. There is one YSI EXO2 resting on the seabed in a cage at mid-channel (around 14 meters from either bank). This location has depths that range from 0-3 meters.

Guadalupe is a slough habitat that receives freshwater input from Saratoga Creek, POTW input from Sunnyvale via Moffett Channel, and is connected to restored salt ponds. A single YSI EXO2 is deployed in a cage that rests on the seabed. This location has depths that range from 0-3 meters.

	2015	2016	2017
JANUARY	0	4.76	7.8
FEBRUARY	2.64	0.65	6.53
MARCH	0.2	4.97	3.11
APRIL	1.51	1.99	1.57
MAY	0.02	0.26	
JUNE	0.03	0	
JULY	0.02	0	
AUGUST	0	0.01	
SEPTEMBER	0.02	0	
OCTOBER	0.01	4.22	
NOVEMBER	2.6	1.28	
DECEMBER	4.04	4.21	

Table 4.4: Monthly precipitation (inches) at Union City; data from CIMIS [58]

Coyote is located in the confluence of Coyote Creek and Alviso Slough. It receives freshwater from Coyote Creek and POTW input from the City of San Jose through the Artesian Slough. The moored line is deployed off of a tower and contains a SeaBird HCEP 1.2 m.a.b. Sensor depths range from 2-5 meters.

Alviso Slough receives freshwater from the Guadalupe River and is connected to restored salt ponds upstream and downstream the field deployment location. There is no direct POTW input into Alviso Slough. A mid-channel, seabed-resting cage contains a YSI EXO2 0.5 m.a.b. This location has depths that range from 1-4 meters.

Lastly, we have measurements from the **Pond A8** channel that feeds into the Alviso Slough. This mid-channel, seabed-resting cage contains a YSI EXO2 0.5 m.a.b. This location has depths that range from 0-3 meters. [60]

4.5 Annual Cycle

Precipitation in the Bay Area is highly variable in a given season. Understanding the seasonal variability of salinity, stratification, and temperature can offer insight as to how conditions in LSSFB vary based on precipitation. With a dynamic climate, it is advantageous to understand how climates of prolonged drought or climates of extreme precipitation affect LSSFB. Variations in climate could lead to seasons of runaway stratification leading to harmful algal blooms. This section describes the seasonal variation in LSSFB from September 2015 through February 2017.

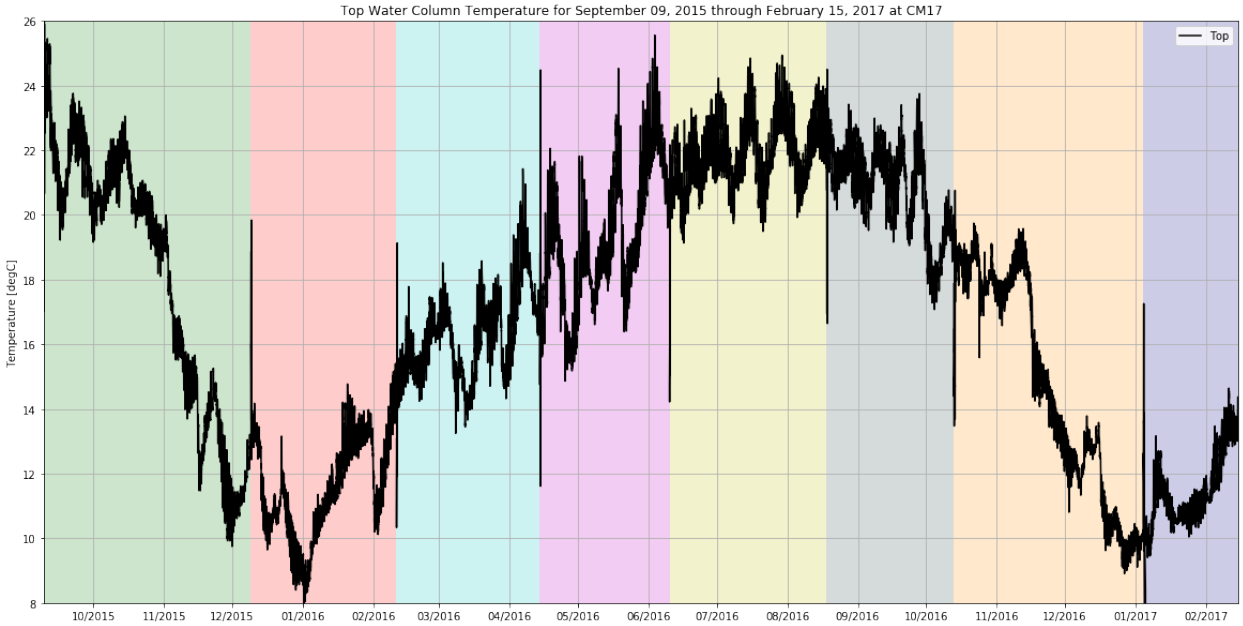

Figure 4.4: Top water temperature at channel marker 17 in degrees Celsius

Rainfall

Table 4.4 shows monthly precipitation in inches at Union City, the closest CIMIS weather station to CM17. The total precipitation increases with time from 2015 to 2016 to 2017. 2015 was a unique season for the Bay Area as it bookended a prolonged drought. In the 2016-2017 rainy season, the Bay Area experienced an El Niño event which drastically increased the precipitation input into the bay. 2017 has almost twice as much precipitation over the January-February months than 2016. Section 4.6 will discuss in more detail how buoyancy input affects salinity and stratification in these two winter seasons.

Temperature

Measured water temperature at the top of the water column at CM17 (Figure 4.4) shows an annual temperature cycle of warming from January to August and cooling from August to January. Within the annual cycle, from March 2016 through October 2016, water temperatures fluctuate not only on a seasonal time scale but also with a two week fluctuation. This two week variation is likely due to the spring-neap cycle which effects the tidal reach of the estuary. This two week temperature fluctuation will be discussed in more detail in section 4.6.

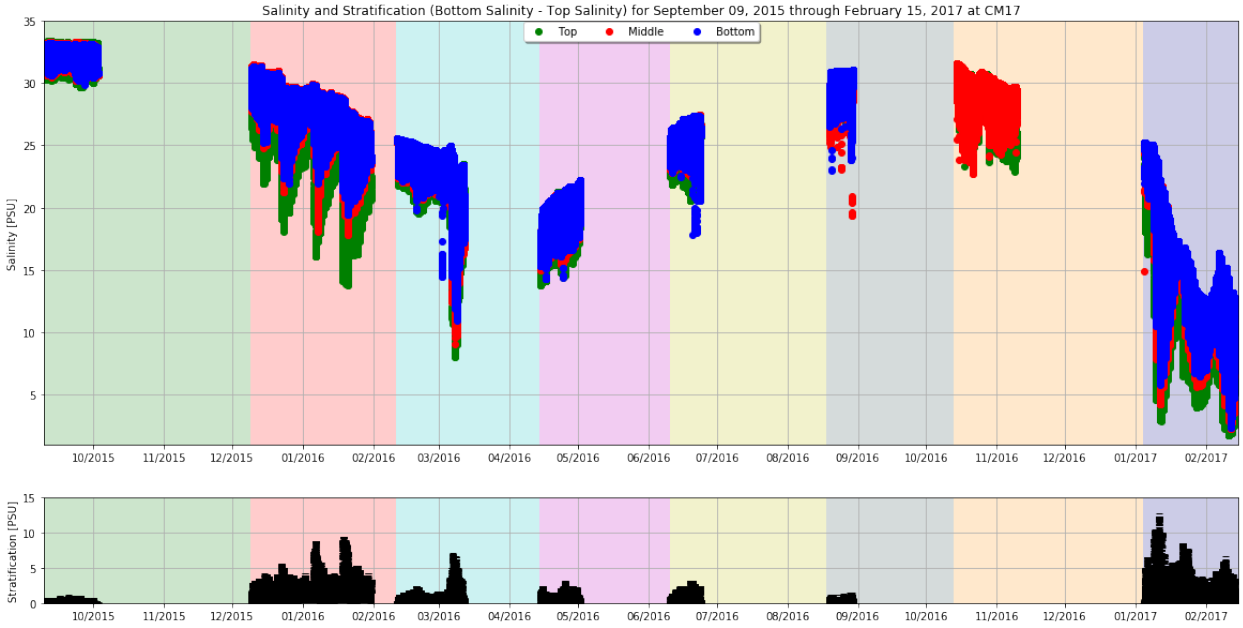

Figure 4.5: Measured seasonal salinity with biofouling removed at channel marker 17. Measured stratification calculated by taking the difference between the measured salinity at the bottom of the water column and the measured salinity at the top of the water column. We were unable to recover the measured salinity from the bottom CTD during the orange deployment (October 2016 - January 2017), so there is no measured stratification during that period.

Salinity

Figure 4.5 plots measured seasonal salinity at CM17 from September 2015 to February 2017. Each salinity time series had to be truncated due to biofouling. Due to high levels of nutrients and available light, biofouling is a nuisance in the center of LSSFB requiring cycling of equipment every few weeks in the summer and every month in the winter. Biofouling occurred most quickly during the summer months, making available data limited for the dry seasons. Unfortunately, cycling of equipment could occur only once every 2 months resulting in gaps in the annual data set.

Salinity varies on a tidal time scale as well as on a seasonal time scale. During rainy seasons, overall salinity decreases throughout the estuary and in the perimeter. There are greater fluctuations in salinity as the longitudinal salinity gradient increases with increasing buoyant input (December 2015 - February 2016 and January 2017 - March 2017). Salinity recovers gradually as rainfall runoff continues to trickle into the perimeter over time.

In LSSFB, there is a large seasonal fluctuation in the average water column salinity. During the dry seasons (May - September), salinity reaches a maximum. As more buoyant input is added to the estuary in wet seasons, the overall salinity decreases. The two winter, rainy seasons that were captured (December 2015 - February 2016 and January 2017 -

February 2017) show how the estuary is influenced by increase of buoyant input. The 2017 winter event has almost double the precipitation total as 2016 (see Table 4.4) causing a significant drop in salinity magnitude in the entire water column. In the second deployment beginning December 2015, there are three sudden drops in salinity due to rainfall events and a similar rate of recovery posing the question: what is affecting the rate of recovery in an estuary? Section 4.7 will look deeper at the recovery of salinity during this deployment. The 2015-2016 winter season sees a more complete recovery between precipitation events than the 2016-2017 winter.

As expected, stratification shown in the bottom panel of Figure 4.5 increases as buoyant input increases. During the drier seasons, stratification is close to zero. As buoyant input increases in the second deployment, stratification also increases. After the initial peak of stratification of each rain event, stratification is mixed out and gradually returns to equilibrium as gradients are destroyed by tidal mixing and as freshwater trickles in from rainfall runoff through the perimeters and eventually to the estuary channel.

4.6 Comparison of Fall 2015, Winter 2015-2016, and Winter 2016-2017 Seasons

Three deployments contain velocity data allowing for the differentiation of flood and ebb tides. In Figures 4.4 and 4.5 the green (September 2015, fall 2015), yellow (February 2016, winter 2015-2016), and purple (January - February 2017, winter 2016-2017) deployments have ADCP measurements. During these three deployments, there is varying buoyant input. Referring to Table 4.4, in September 2015 there was a total of 0.02 inches of precipitation, 4.76 inches of precipitation in January 2016, and 7.8 inches of precipitation in January 2017. Therefore, the fall 2015 deployment has very dry conditions, medium precipitation in winter 2015-2016, and high precipitation in winter 2016-2017. This section will compare the dynamics in LSSFB during these seasons of varying freshwater input.

Winter 2016-2017

In the October 2016 - March 2017 season, the Bay Area received relief from a several-year drought. This El Niño season brought high levels of precipitation. The deployment observed conditions in LSSFB under extremely wet conditions. This wet deployment captured both salinity and velocity measurements from a three-dimensional array of CTDs, Seabirds, and ADCPs. The hydrodynamics of this season were studied closely on the tidal time scale in chapter 2. The large buoyant input revealed which mechanisms are important to the tidal stratification cycle. Chapter 2 explained how stratification dynamics switched between being longitudinally dominated during the middle of ebb and flood tides to being laterally dominated during tide transitions. Differential advection along with lateral exchange at tide transitions resulted in more saline water transported from the shoals to the channel at the

end of each ebb tide from barotropic forcing and less saline water transported from the shoals to the top of the channel at the end of the flood tide from baroclinic forcing.

Salinity, velocity, and temperature measurements were collected from January 27, 2017 through February 11, 2017. This deployment experienced the least amount of biofouling likely due increased mixing, cooler water temperatures, as well as less available light.

Salinity in Winter 2016-2017

The top panel in Figure 4.6 provides a data-rich longitudinal salinity time series of Lower South San Francisco Bay. During this window, there are consistent salinity observations at Dumbarton Narrows and Coyote Creek as well as multiple salinity measurements in the water column at the center of the estuary within the deep channel. During this wet winter, the perimeter (Coyote Creek and Mowry) is always fresher than the channel (CM17). Dumbarton, located down-estuary, is more saline than CM17 until the rainfall events. The rainfall events increase the range of the salinity gradient between Dumbarton Narrows and CM17 as well as some moments of reversing gradient signs (middle panel of Figure 4.6). All locations exhibit freshening over ebb tides and increased salinity over flood tides. The longitudinal salinity gradient between Dumbarton and CM17 is built up over the ebb tide and broken down to zero over the flood tide.

The bottom panel in Figure 4.6 shows salinity at CM17 and salinity at a location on the lateral perimeter (Mowry). Mowry exhibits similar freshening over the ebb tide and increase in salinity over the flood tide like CM17. During tide transitions, salinity changes are more gradual in Mowry than at CM17. This could be due to the habitat. In the sloughs, there is vegetation which allows for gradual inputs of freshwater as runoff must make its way through to the estuary. At CM17, there are sharper transitions from freshening to increasing salinity at the ebb to flood transition. In the Mowry salinity time series, this transition is more gradual. When buoyant input increases in February, the ebb to flood transition in fact shows that the salinity remains consistent for several hours before the salinity increases in the flood tide (02/04 - 02/11 bottom panel of Figure 4.6). Dumbarton and Coyote salinity time series do not show the pulses of freshwater at the flood to ebb transition or increases in salinity at the ebb to flood tides that was observed in detail in Chapter 2.

Temperature in Winter 2016-2017

According to the temperature measurements in Figure 4.7, the temperature in perimeter locations (Mowry and Coyote Creek) is strongly influenced by the rainfall events that occur in the second half of the deployment. Mowry goes from being cooler than CM17 to warmer as soon as rain events happen in the neap tide around February 2, 2017. As the rain continues until the end of the deployment, Mowry and Coyote remain warmer than CM17 and Dumbarton. Consistent with the other deployments, the shallower locations have larger ranges in temperature fluctuations. The change in water temperature in the estuary is dependent on whether the atmosphere is cooling or heating and based on the occurrence

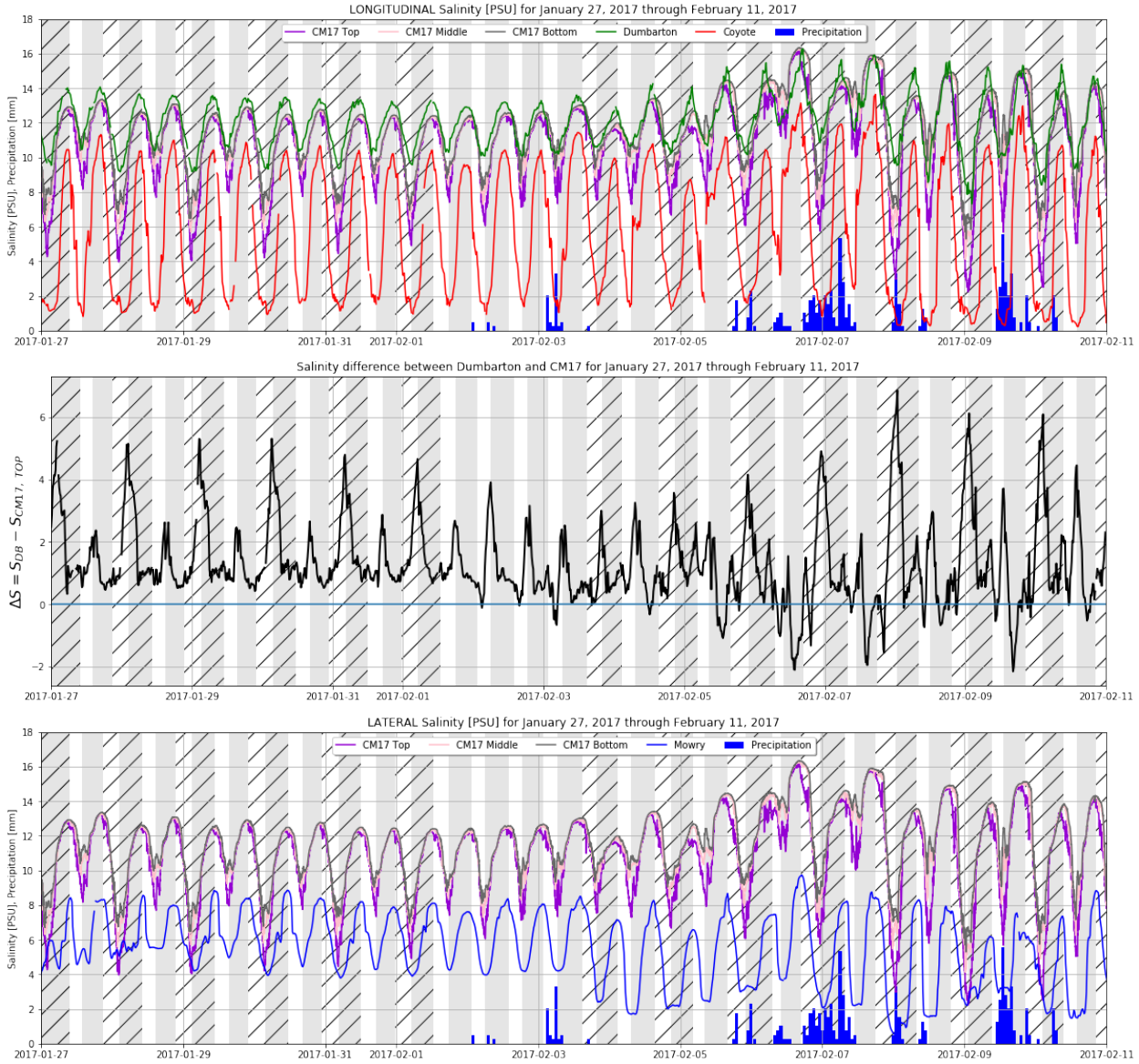

Figure 4.6: Longitudinal (top panel) and lateral (bottom panel) salinity in PSU during wet, winter season (2016-2017). Middle panel is the salinity difference between Dumbarton and CM17. Dumbarton is located down estuary from CM17 while Coyote and Mowry are located up estuary. Precipitation at Union City shown in mm. The middle panel displays the longitudinal salinity difference between Dumbarton and CM17. Note: Flood tides correspond to gray shading. Ebb tides correspond to white shading. Hatching refers to larger flood/ebb tides when there is a diurnal asymmetry. The start of each tide is determined by the vertically averaged longitudinal velocity.

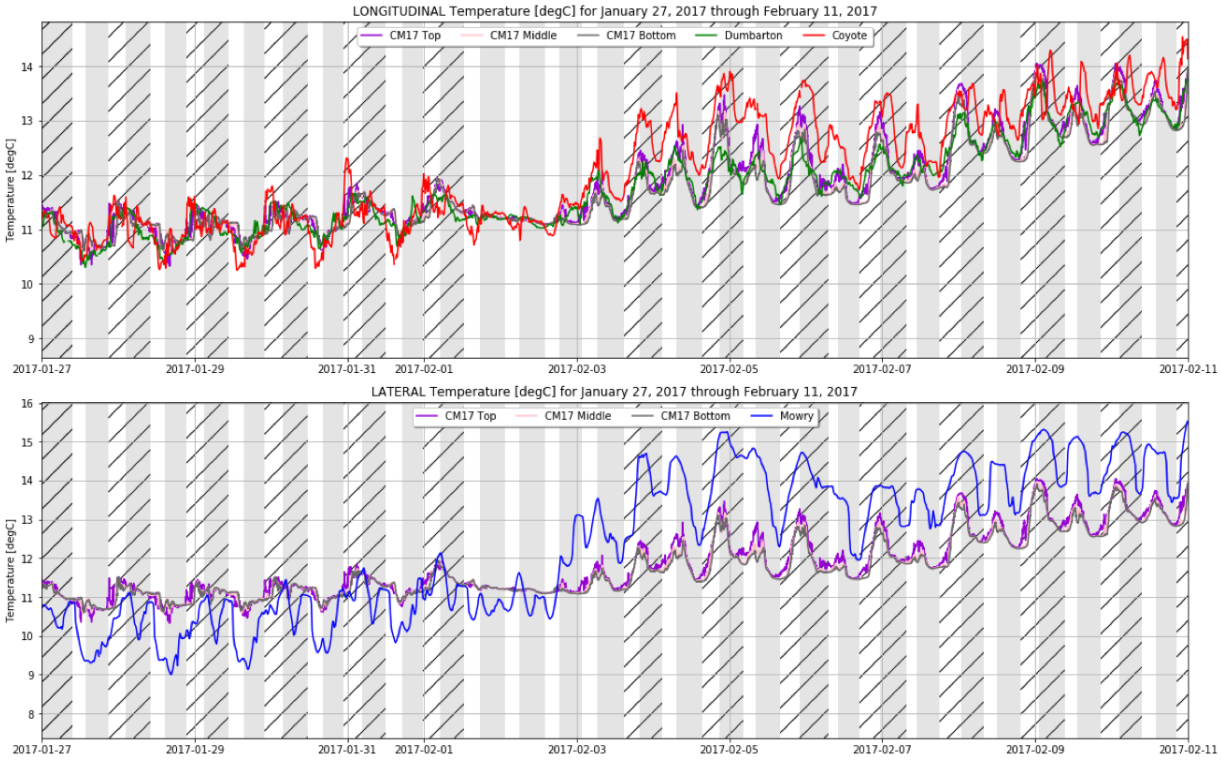

Figure 4.7: Longitudinal and lateral water temperatures during wet, winter season (2016-2017). Dumbarton is located down estuary from CM17 while Coyote and Mowry are located up estuary. Note: Flood tides correspond to gray shading. Ebb tides correspond to white shading. Hatching refers to larger flood/ebb tides when there is a diurnal asymmetry. The start of each tide is determined by the vertically averaged longitudinal velocity.

of rainfall events. Mean water temperature tends to follow the seasonal air temperature warming and cooling as well as the daily warming and cooling. The tide adds another layer of complexity as it transports water either from outside the estuary during the flood tides or water from the perimeters into the estuary during the ebb tides.

Winter 2015-2016

In the December 2015-February 2016 winter, precipitation was moderate compared to the 2016-2017 winter and the 2015 fall. ADCP measurements were collected from February 22, 2016 through March 9, 2016. During this deployment, there was no precipitation from February 22, 2016 until March 4, 2016. From March 4, 2016 to the end of the deployment, two large precipitation events cause freshening of the bay as well as decreased water temperatures. Winter 2015-2016 compared to winter 2016-2017 has less total cumulative precipitation (Table 4.4), but similar water temperatures allowing differences in observations between the two seasons to be likely attributed to precipitation (Figure 4.4). The average

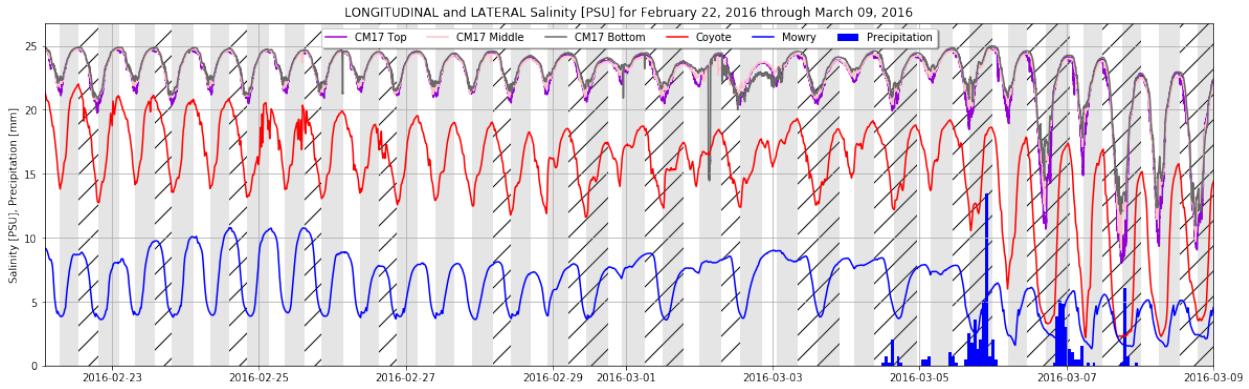

Figure 4.8: Longitudinal and lateral salinity in PSU during winter season (2015-2016). Dumbarton is located down estuary from CM17 while Coyote and Mowry are located up estuary. Note: Flood tides correspond to gray shading. Ebb tides correspond to white shading. Hatching refers to larger flood/ebb tides when there is a diurnal asymmetry. The start of each tide is determined by the vertically averaged longitudinal velocity.

salinity is greater during this winter than the winter of 2016-2017 (Figure 4.5) due to the increased precipitation.

Salinity in Winter 2015-2016

There is no salinity data available at Dumbarton for this time window. In the longitudinal direction, salinity decreases up estuary. With this longitudinal salinity gradient, longitudinal advection results in an increase of salinity over the flood tides and a decrease of salinity over the ebb tides at all locations. Mowry's salinity time series seems strongly coupled with the tide. During this time window, Mowry is always fresher than the channel indicating a consistent sign of the lateral salinity gradient. When it rains in March, there is an overall freshening at CM17, Coyote, and Mowry. Mowry is almost completely freshened to 0 PSU during these rainfall events.

During this winter season, stratification at CM17 develops most strongly at the end of each ebb tide which is consistent with what is expected from a longitudinally-driven estuary. However, stratification develops briefly at the end of each flood tide which continues to develop over the ebb tide maximizing at the end of the ebb. The initialization of stratification before the turn of the tide could be an indication of laterally strained induced stratification which was described in chapter 2. Throughout this season, stratification is broken down in each ebb tide similar to winter 2016-2017.

Temperature in Winter 2015-2016

Figure 4.9 shows the time series of water temperature at various locations in the along- and across-channel directions. There is limited Dumbarton temperature data for this time frame.

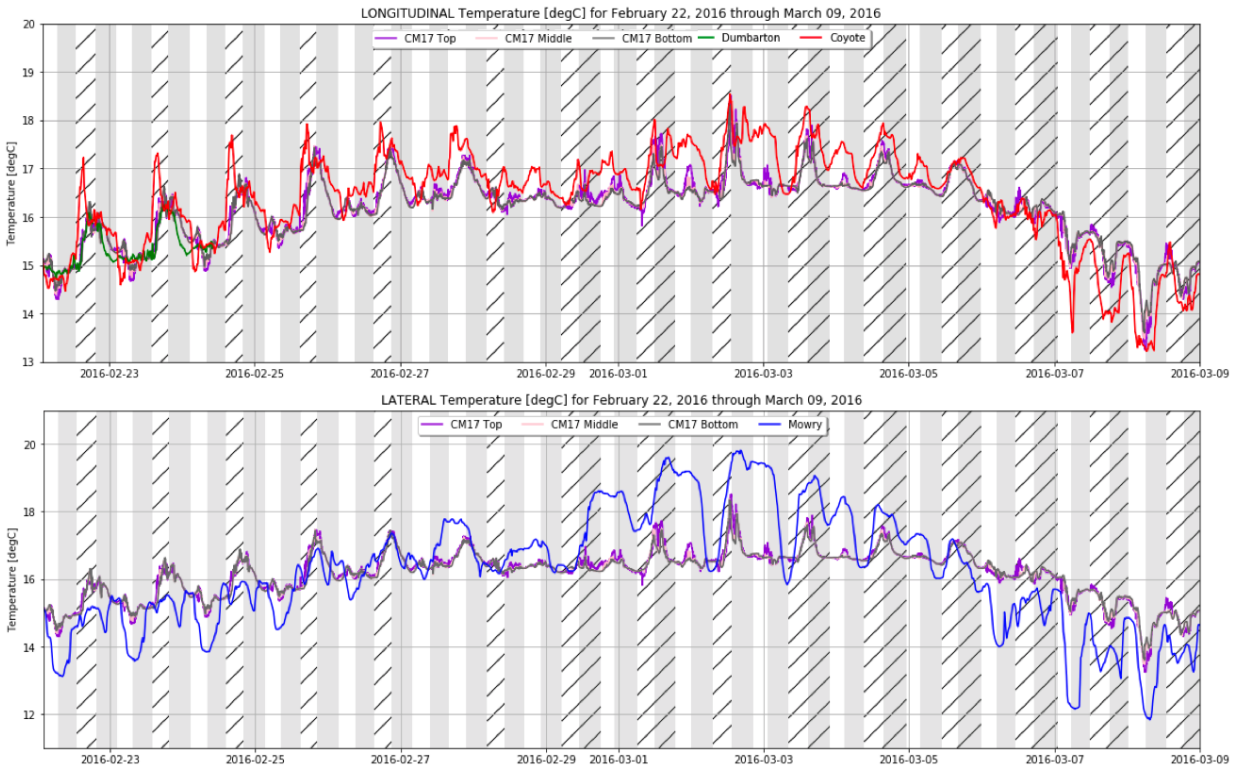

Figure 4.9: Longitudinal and lateral water temperatures during winter season (2015-2016). Dumbarton is located down estuary from CM17 while Coyote and Mowry are located up estuary. Note: Flood tides correspond to gray shading. Ebb tides correspond to white shading. Hatching refers to larger flood/ebb tides when there is a diurnal asymmetry. The start of each tide is determined by the vertically averaged longitudinal velocity.

From the first few days where measurements of temperature at Dumbarton are available, as expected, Dumbarton has a smaller amplitude than CM17 and Coyote Creek. Coyote Creek remains warmer than CM17 as the overall temperatures are increasing, but then cools faster than CM17 after March 5, 2016. Since Coyote Creek is shallower than CM17, it responds more strongly to atmospheric forcing than the deep channel and will feel effects from runoff more quickly. Mowry has a different signal than Coyote. Mowry is cooler than CM17 from February 22, 2016 through February 27, 2016 and then is warmer than CM17 until the rainfall events. After the rainfall events, Mowry is cooler than CM17 similarly to how precipitation caused Coyote Creek to be cooler than the estuary. These varying temperature gradients could also be a result of the magnitude of precipitation input or due to the amount of time it takes for the water column to feel atmospheric temperature shifts. Coyote and Mowry both are shallower than CM17 meaning the water columns in these locations will be completely warmed or completely cooled before the water column of CM17. Based off the second half of both observed winters, it seems precipitation events cause perimeter water columns to be shifted to 12-15 degrees Celsius.

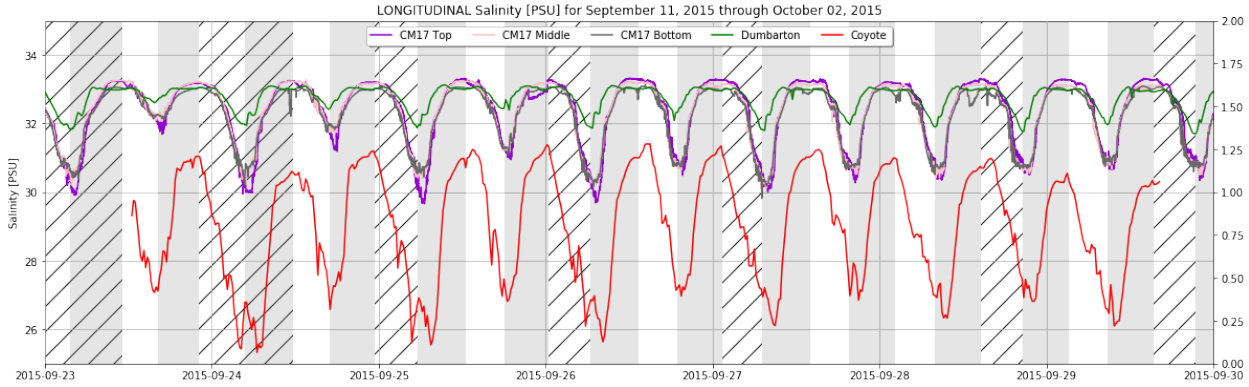

Figure 4.10: Longitudinal salinity in PSU during dry, fall season (2015). Dumbarton is located down estuary from CM17 while Coyote is located up estuary. Note: Flood tides correspond to gray shading. Ebb tides correspond to white shading. Hatching refers to larger flood/ebb tides when there is a diurnal asymmetry. The start of each tide is determined by the vertically averaged longitudinal velocity.

Fall 2015

The first deployment with ADCP data took place in the fall of 2015. During this deployment (September 10, 2015 through October 2, 2015), there was only one rainfall event on September 30, 2015. This deployment captures one of the most extreme dry conditions in the Bay Area. The drought began around 2011 and was not relieved until El Niño brought more normal precipitation in the winter of 2016-2017. Typically, September is among the warmest months of the year with little to no precipitation which is consistent with what the conditions in September 2015.

Salinity in Fall 2015

Figure 4.10 shows the time window during the September 2015 deployment where there is available longitudinal data at the Dumbarton Bridge (green line) and Coyote Creek (red line). The observed salinity at Dumbarton is freshest at the end of the ebb tide and fresher than CM17 at the end of the flood tide. Similar salinity patterns match what is expected from a longitudinally driven salinity pattern with freshening over the flood tide and getting more saline over the ebb tide. During large ebb tides, freshening is greater compared to the freshening that occurs over the smaller ebb tide. These diurnal inequalities in the salinity are seen in all longitudinal locations - Dumbarton, CM17, and in Coyote Creek.

At the end of the flood tide, the salinity at the top of the water column is consistently greater than the middle and bottom of the water column at CM17. The difference between the water temperature at the top of the water column verses the middle and bottom could be great enough such that this difference in salinity is not actually an indicator of density instability. The linearized equation of state is dependent on both the salinity and temperature

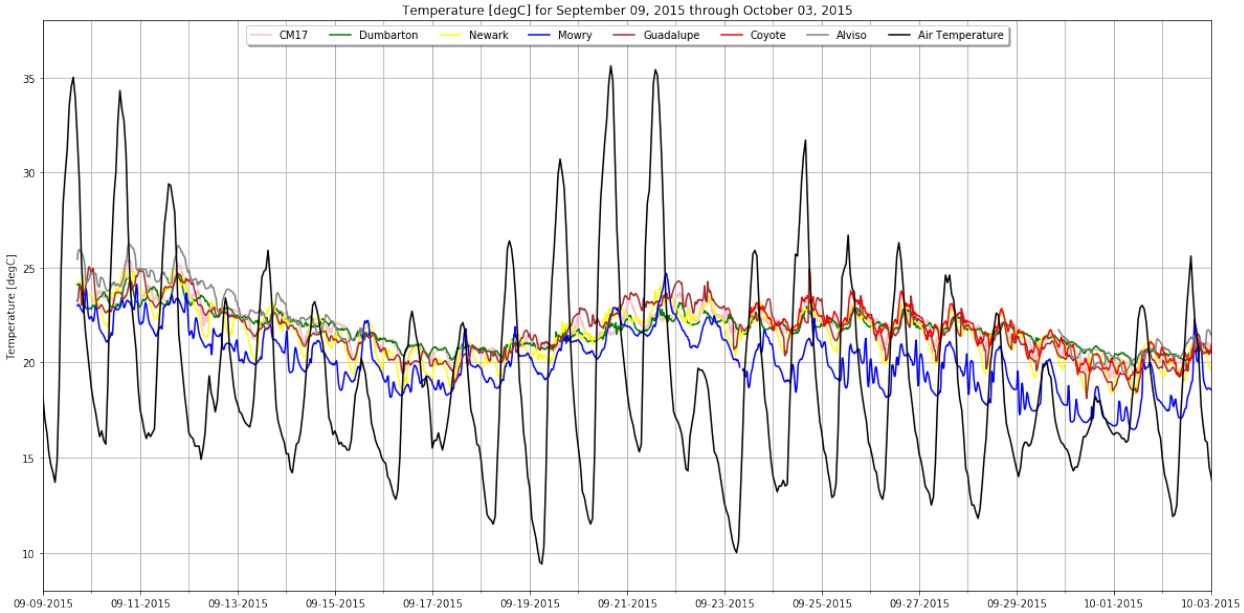

Figure 4.11: Air temperature (black line) and water temperatures (colored lines) in degrees Celsius during dry, fall season (2015)

of the water (Equation 4.1) [55]. For $S_0 = 35$ PSU, $T_0 = 15$ degrees Celsius, and $\sigma_0 = 26$ kg/m^3, coefficients $\alpha_T = 2.1 \times 10^{-4}$ K^{-1} and $\beta_S = 7.5 \times 10^{-4}$ PSU^{-1}. The ratio of α_T and β_S, reveals that a change of 3.6 K (or degrees Celsius) has an equivalent effect on density as a change of salinity by 1 PSU. The measured salinity difference in the top and bottom of the water column has a minimum of around -0.2 PSU (see Figure 2.3) meaning a temperature difference of about 0.72 degrees Celsius could offset this. Throughout the fall season, the top bottom temperature difference did exceed 1 degree Celsius. During this deployment there are moments of temperature differences up to 1.5 degrees Celsius in the water column.

$$\sigma = \sigma_0 + \rho_{ref}[\beta_S(S - S_0) - \alpha_T(T - T_0)] \tag{4.1}$$

Unfortunately, there is no salinity data collected at Mowry for this time frame, therefore there are no lateral salinity gradients observations this fall. In all three salinity time series, the transition from ebb to flood has a sharper change in $\frac{\partial S}{\partial t}$ than the more gradual $\frac{\partial S}{\partial t}$ from flood to ebb. The sharpness is likely due to spatial variation of $\frac{\partial S}{\partial x}$. Since the sloughs and perimeters are relatively fresh, upstream $\frac{\partial S}{\partial x}$ is much greater than $\frac{\partial S}{\partial x}$ in waters north of the Dumbarton. Therefore, at the end of the ebb tide, CM17 sees a stronger gradient because of the advection of fresh water from the margins, while at the end of the flood, the weaker gradient from the open bay has advected to CM17.

Temperature in Fall 2015

Figure 4.11 shows how the water temperature in the estuary follows the ambient air heating and cooling pattern. The depth of sensors for each location (refer to Table 4.3) goes from 0-3 meters at Pond A8, Guadalupe, Mowry, and Newark to 1-4 meters at Alviso and Dumbarton to 2-5 meters at Coyote and San Mateo. Although the depth of the sensors at Dumbarton and San Mateo are shallower than the depth of sensors at CM17, water column depth of Dumbarton and San Mateo are deeper than the water depth at CM17. The range of each location's temperature fluctuations corresponds to the water column depth. When the water column depth is shallow, the temperature fluctuates more. Looking at the peaks in each time series, the warmest water temperatures occur at Alviso, Guadalupe, CM17, and Coyote. The coolest measured water temperatures occur in Mowry and then Newark. These locations are both shallow sloughs located on the south-eastern perimeter in channels that feed into Lower South San Francisco Bay. Water temperatures at each location varies on a tidal time scale as well as an overall seasonal timescale. The mean of the water temperatures follow the mean of the air temperature with a smaller amplitude. Maximum air temperatures occur in the afternoon of each day. The water temperature has a lag in warming which occurs a few hours after the air temperature has warmed.

Assuming daily atmospheric heating and cooling patterns and tidal advection are the biggest influencers of water temperature at a given location in the estuary, there are four phases of heating and cooling in a given day. On the daily timescale, there is atmospheric heating from sunrise to sunset and then cooling from sunset to sunrise. Within a 24-hour period, there are four tides, two flood tides that bring water from north of the Dumbarton Narrows into the estuary and two ebb tides that bring water from the surrounding, shallow perimeters into the estuary.

Figure 4.12 shows water temperature over two days in the dry, fall season to break down these phases. According to timeanddate.com, in San Jose, California, the sun rose at 6:54 AM and set at 7:05 PM on September 21, 2015. Air temperatures ranged from 19 degrees Celsius (66 °F) to 36 degrees Celsius (97 °F) on September 21. The range of air temperature was lower on September 22, 2015 with a low of 63 degrees Fahrenheit and a high of 75 degrees Fahrenheit. The nighttime ebb phase occurs at September 21, 2015 at 0:00 and September 22, 2015 2:00. During this period, atmospheric temperatures are cooling when the sun is set and advection of gradients as the ebb tide brings in water from the perimeter into the estuary. The perimeter locations, Mowry, Coyote, and Newark cool first which is eventually advected to CM17. In summary, during the nighttime ebb, perimeter locations cool first from atmospheric cooling then tidal advection cools CM17 from mid to late ebb.

The next phase is the daytime flood tide which starts September 21, 2015 at 6:30 AM and September 22, 2015 at 7:00 AM. During this phase, there is warming due to the rising sun and cooling from the flood tide bringing in cooler water from north of the Dumbarton. Depending on how strong each of these mechanics are, this phase result in a cooling or warming water column. During these two selected daytime flood examples, the water temperatures have slight warming by the late flood tide. The strongest warming occurs in Mowry and Coyote.

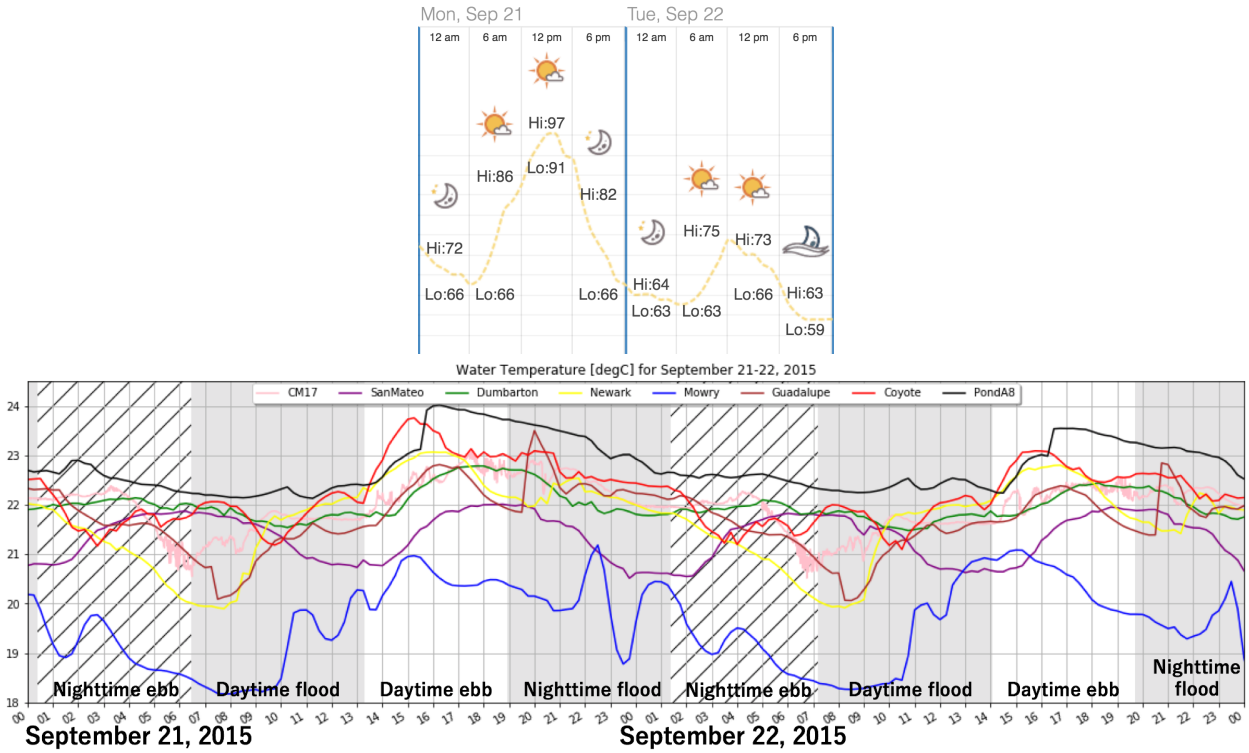

Figure 4.12: Historical sunrise and sunset times from timeanddate.com for San Jose, California in September 2015 and Water temperatures for two days (September 21, 2015 and September 22, 2015) in dry, fall season (2015). The x-axis is the local hour (PDT). Note: Flood tides correspond to gray shading. Ebb tides correspond to white shading. Hatching refers to larger flood/ebb tides when there is a diurnal asymmetry. The start of each tide is determined by the vertically averaged longitudinal velocity.

The third phase is the daytime ebb which starts September 21, 2015 around 1:00 PM and September 22, 2015 at 2:00 PM. During this phase, there is maximum heating due to compounding advection from tidal forcing and daily heating that occurs in the late afternoon. The ebb tide pulls warmer water from the perimeter at locations such as Coyote, Newark, and Pond A8 into the estuary to CM17 and then to Dumbarton.

The fourth and final phase is the nighttime flood which begins September 21, 2015 at 7:00 PM and September 22, 2015 at 8:00 PM. During this phase, cooling occurs due to the compounding cooling from both tidal forcing and atmospheric cooling. During this tide, the cooler water from San Mateo is advected to Dumbarton and then to CM17 and lastly to the perimeter locations.

Daily atmospheric heating and cooling occurs at a 24-hour frequency while tidal advection occurs on an M2 timescale of 12.4 hours. Therefore, there is an offset resulting in a 2-week periodicity for water temperature patterns affected primarily by daily atmospheric heating and cooling and tidal advection. Figure 4.4 showed larger 2-week fluctuations in temperature

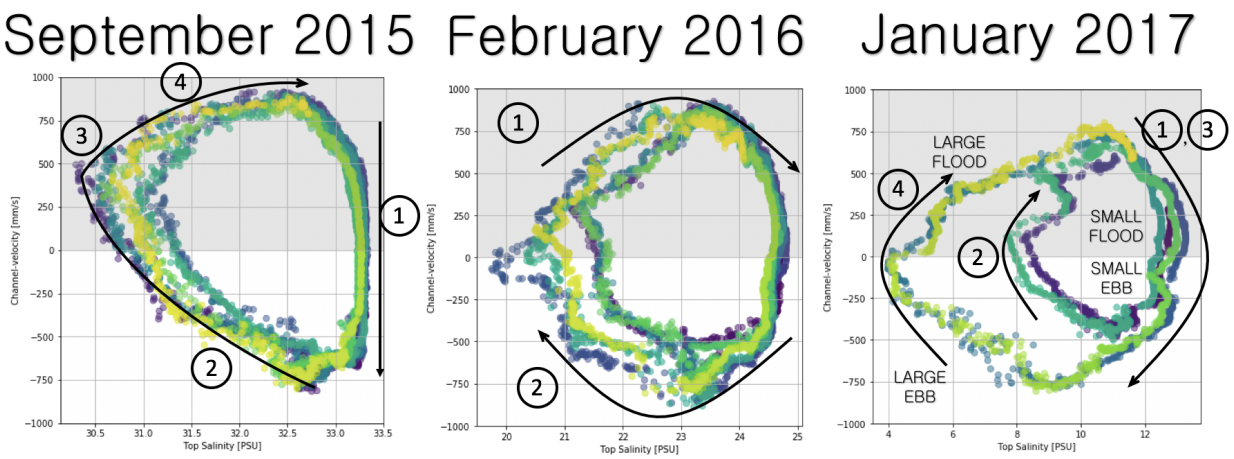

Figure 4.13: Scatter plot of channel velocity versus top salinity for three varying seasons at CM17 within the deep channel of LSSFB (*34.47798, -122.07658*). In increasing buoyancy input: September 2015, February 2016, and January 2017. Positive channel velocities correspond to flood tides and is shaded in gray. Negative channel velocities correspond to ebb tides and has a white background. A few tides were selected out of the deployment for these scatter plots: September 13 - 16, 2015, February 22 - 25, 2016, and January 27 - 29, 2017.

during the warmer months of the year. Perhaps this offset of tide and atmospheric forcing is a contributing mechanism responsible for these two week fluctuations in water temperature that is observed from March - October 2016. It should be noted that the phasing of M2 tide to the day-night cycle will be correlated with the spring-neap cycle, so we can't fully separate the two effects.

Intercomparisons between Fall 2015, Winter 2015-2016, Winter 2016-2017

Figure 4.13 shows scatter plots of top salinity (x-axis) versus along-channel velocity (y-axis) for the three deployments with velocity data. Positive values of the along-channel velocity correspond to the flood tide which pulls water from outside LSSFB into the estuary (shaded gray). Negative values of the along-channel velocity correspond to the ebb tide which pulls water from the marsh-perimeters into the estuary (shaded white). As expected, during all three seasons the top salinity increases over the ebb tide and decreases over the flood tide. However, the shape of the change in salinity varies based on the buoyant input.

The dry, fall 2015 has a flatter shape on the right-hand side due to the upper limit of salinity. During the flood to ebb transition (1), the estuary experiences maximum salinity around 33.25 PSU. February 2016 and January 2017 have rounder shapes and lower magnitudes of salinity corresponding to freshwater inputs in each season. As freshwater input increases, the range of salinity experienced at CM17 for a given tide increases. September

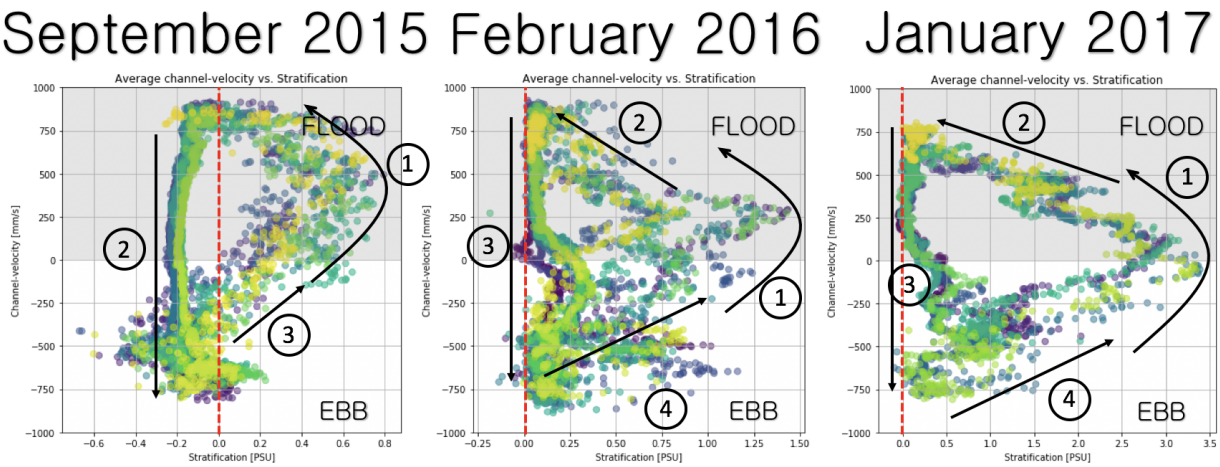

Figure 4.14: Scatter plot of channel velocity versus stratification for three varying seasons at CM17 within the deep channel of LSSFB (*34.47798, -122.07658*). In increasing buoyancy input: September 2015, February 2016, and January 2017. Positive channel velocities correspond to flood tides and is shaded in gray. Negative channel velocities correspond to ebb tides and has a white background. Stratification is calculated by taking the difference between the measured salinity at the bottom of the water column and the measured salinity at the top of the water column. A few tides were selected out of the deployment for these scatter plots: September 13 - 16, 2015, February 22 - 25, 2016, and January 27 - 29, 2017.

2015 ranges from 30.5 to 33.5 (ΔS = 3 PSU). February 2016 ranges from 20 to 25 PSU (ΔS = 5 PSU). Lastly, February 2017 ranges from 4 to 13 PSU (ΔS = 9 PSU). With greater buoyant input, the left side of the scatter plot would flat line at 0 PSU similar to the flat line at the upper limit shown in September 2015.

For all seasons, the salinity drops most quickly from beginning to mid flood and increases most quickly from mid to end ebb. Changes in salinity are more gradual from mid flood to mid ebb. At the beginning to mid flood, salty water from outside the mouth of the estuary is pulled over top fresher water causing instability which leads to rapid mixing which would explain the rapid change in salinity from beginning to mid flood. Decrease of salinity from mid to late ebb tide is likely due to the longitudinal advection of salinity gradients.

During the January 2017 selected tides (January 27 - 29, 2017), there are tidal asymmetries which result in variation of the minimum salinity. During the larger ebb tides, the salinity is pulled farther down to 20 PSU versus during the smaller ebb tides, the salinity is pulled to 21.5 PSU.

Figure 4.14 shows scatter plots of stratification (x-axis) versus the along-channel velocity (y-axis). Stratification is calculated by taking the difference between the bottom and top measured salinity. Each of the three deployments have varying shapes and patterns. All three move in a counter clockwise direction with time. As buoyancy input increases (September 2015 to February 2016 to January 2017), the magnitude of maximum stratification increases.

The timing of maximum stratification occurs at the ebb to flood transition in February 2016 and January 2017. However, the maximum stratification in September 2015 is delayed and occurs slightly after the tidal transition. Minimum stratification in September 2015 is -0.2 PSU whereas the minimum stratification in February 2016 and January 2017 are 0 PSU. During the September 2015 season, there can be up to a 1.5 degrees Celsius top and bottom temperature difference. Therefore, the negative persisting stratification is likely not a density instability but is likely a neutral density profile.

The rate of stratification break down over the beginning to mid-flood is more consistent in the winter seasons (February 2016, January 2017) than in September 2015. In the two winter seasons, at the transition from flood to ebb there is a small creation of stratification that begins at the end of the flood and increase into the ebb tide which is broken down as the ebb velocities increase. This is likely due to lateral exchange during the tidal transition (see chapter 2 for details). Between the three scatter plots, as buoyant input via precipitation increases, the scatter is stretched along the horizontal axis with a slight shift to the right. Even in the most extreme present conditions, runaway stratification does not occur. Turbulent mixing is always strong enough to destratify the water column on each given tide.

Summary of Annual Cycle

Observed salinity and temperature measurements in LSSFB show high spatial and seasonal variability. Warmest temperatures up to 25 degrees Celsius and lowest salinity down to 5 PSU are found in the shallow perimeters (Coyote) during the months with highest atmospheric temperatures. In the shallow perimeters, water temperature throughout the water column is more quickly influenced by atmospheric heating and cooling. Rivers input freshwater directly into the perimeters and then rainfall runoff trickles in through the marshes after precipitation events creating both longitudinal and lateral gradients.

Salinity is highly influenced by precipitation. Salinity at CM17 ranges from 3 PSU in the wet winter of 2016-2017 to 33 PSU in the dry fall of 2015. As buoyant input increased, stratification increased as well. Even during El Niño, runaway stratification did not occur. However, runaway stratification is most likely to occur in winter seasons with extreme precipitation. Water column temperature showed seasonal variation following atmospheric heating and cooling as well as a two week fluctuation perhaps due to the timing of the tide and daily heating/cooling.

4.7 Event Response, Winter 2015-2016

In the 2015-2016 winter season, there were large storms spaced out around two-weeks from each other which caused the top salinity to freshen by 10 PSU. There seems to be a consistent slope in which the top salinity recovers to equilibrium after a major rainfall event seen in

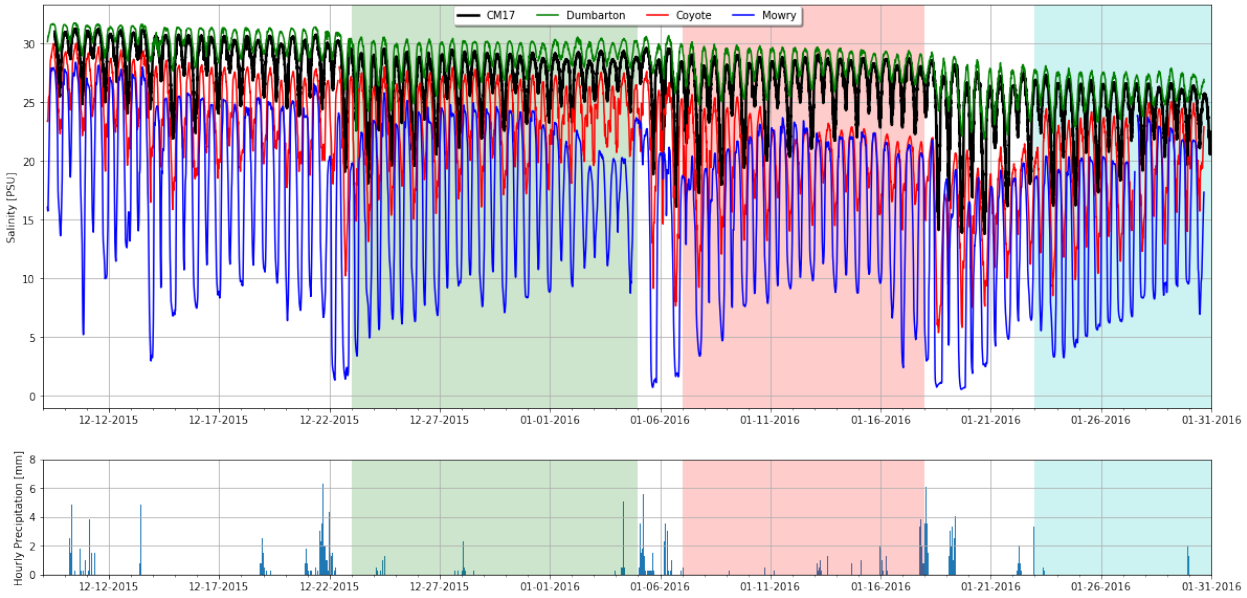

Figure 4.15: Measured salinity at various locations in LSSFB. Dumbarton, CM17 (average of top, middle and bottom), and Coyote are located along-channel in LSSFB while Mowry is across-channel from CM17. Both Coyote and Mowry are located in shallow sloughs at the perimeter. Highlighted areas show salinity recovery after a precipitation event.

Figure 4.15. The recovery can be described by a diffusion coefficient, K.

$$\frac{\partial S}{\partial t} + u\frac{\partial S}{\partial x} = \frac{\partial}{\partial x}(K\frac{\partial S}{\partial x}) \tag{4.2}$$

Figure 4.15 shows the observed salinity in along-channel locations (Dumbarton, CM17, Coyote) and one across-channel location (Mowry). When a rainfall event occurs, the salinity in all locations drop. Shallower locations such as Coyote and Mowry, are most affected by the rainfall events. During the December 22, 2015 storm, the slough, perimeter sites, Coyote and Mowry, have a drop in salinity one tidal cycle before CM17 and Dumbarton locations. During large ebb tides after large rainfall events, the salinity at CM17 overlap with the salinity in the perimeter, Coyote and Mowry. When CM17 and Mowry salinities are similar, Mowry begins to recover back to a saltier state as it mixes with the rest of the estuary. Mowry recovers back to its original salinity on the order of days whereas CM17 and Dumbarton recovers on the order of about two weeks. The overall salinity after each of the rainfall events does not recover completely by the time the next event occurs. Looking at the maximum salinity over this time period in Figure 4.16 at CM17, after each large rainfall event (December 22, January 6, and January 18), there is a decrease of about 1 PSU that does not fully recover to its original salinity before the event occurred.

Figure 4.16 shows more detail of the water column dynamics that occur in the center of the estuary during this season. One or two tidal cycles after large rainfall events, the

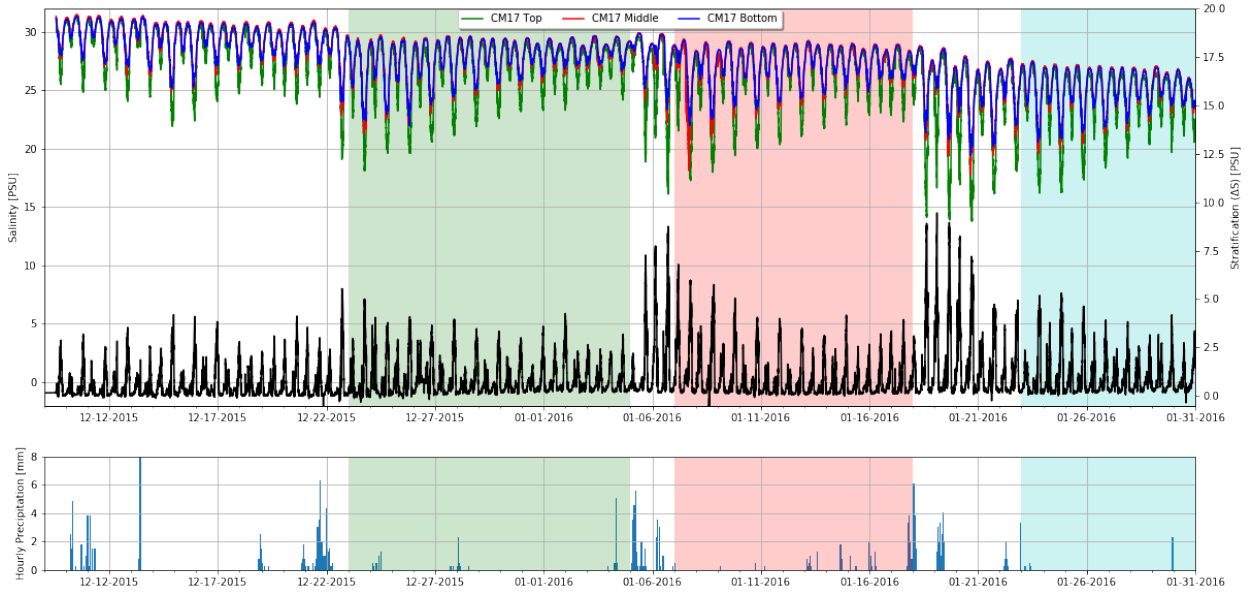

Figure 4.16: Top, middle, and bottom salinity at CM17 and precipitation at Union City during a wet, rainy winter season (December 2015 - January 2016). Highlighted time windows used to observe the salinity recovery rate after the each event.

stratification increases. During the first storm on December 22, stratification jumped from 4 PSU to 8 PSU. The second storm, January 6, had a more dramatic increase from 3 PSU to 11 PSU. And the last storm at January 18 had the largest increase in stratification to almost 15 PSU. As freshwater input increases, there is more potential for larger stratification events. Despite the large input of freshwater to the system, stratification is completely broken down over each following flood tide. This storm has a small intermittent storm around January 23. In order to capture only the recovery, the final storm window begins at January 23 even though the bulk of the storm occurs around January 18.

Mathematical Representation of Recovery

In order to model salinity recovery during this winter season, the salinity time series is split into 3 windows representing each of the large precipitation and recovery events that follow. The three time windows are December 23, 2015 - January 5, 2016 (shaded green in Figures 4.15, 4.16, 4.17, and 4.18), January 7 - 18, 2016 (red), and January 23 - 31, 2016 (blue). The daily minimum, water-column averaged salinity is used to fit two functions in order to model the recovery (red dots in Figures 4.15, 4.16, 4.17, and 4.18).

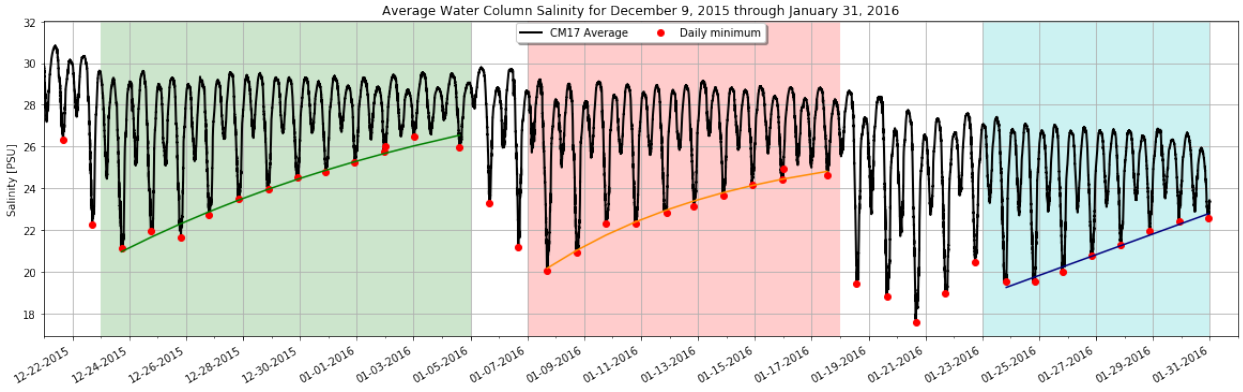

Figure 4.17: Average top, middle, and bottom salinity (black line), daily minimum (red dot), with an exponential decay fit ($S(t) = S_* - Ce^{-t/T_d}$) for CM17 in LSSFB during the winter 2015 - 2016 season. Green fit: $S = 30.9$ PSU, $C = 9.91$ PSU , $T_d = 1.24 \times 10^6$ s; Red fit: $S = 26.3$ PSU, $C = 6.08$ PSU , $T_d = 5.91 \times 10^5$ s; Blue fit: $S = 4250$ PSU, $C = 4.23 \times 10^3$ PSU , $T_d = 7.36 \times 10^8$ s.

Exponential Decay Function

By assuming LSSFB is a continuously stirred tank rector (CSTR), the average salinity in the estuary, S, is represented by the equation with an offset of S_*, coefficient, C, and a recovery time scale of T_d.

$$S(t) = S_* - Ce^{-t/T_d} \tag{4.3}$$

Figure 4.17 shows the three fits for each recovery time window. The best exponential fit was determined using the Levenberg-Marquardt algorithm in scipy's curve fit function. The best fit of the daily minimum salinity time series in the first window from December 23, 2015 - January 5, 2016 is as follows:

$$S(t) = 30.9 - 9.91e^{t/(1.24\times10^6)} \tag{4.4}$$

Here, $T_d = 1.24\times10^6$ seconds or 14.3 days. For the second and third time window (highlighted red and blue in Figure 4.17), fitting the salinity time series to an exponential equation results in dissimilar values for T_d. For the second fit, $T_d = 5.91 \times 10^5$ s (6.8 days), and for the third fit, $T_d = 7.36 \times 10^8$ s (8500 days). Therefore, an exponential representation of the salinity recovery after a precipitation event does not result in consistent recovery time values. The inconsistency could be due to the assumptions in using an exponential decay, because of limited data points, or because as precipitation compounds in the estuary, the recovery time changes. The fit in the third window should likely be discounted due to the longer length and occurrence of an interim rain during this storm (January 18 - 23). There are also Bay-scale adjustments that are not accounted for in these fits. As rain is input into the system, the rain will push salt downstream which then relaxes back. As the rain increases, the relaxation becomes weaker. This could play a role in the variation in fitted T_d values as time persists.

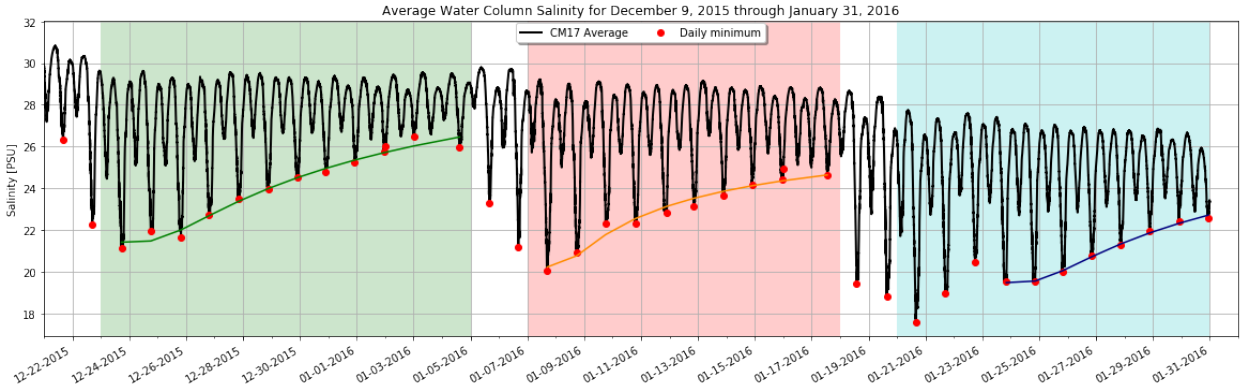

Figure 4.18: Average top, middle, and bottom salinity (black line), daily minimum (red dot), with the solution to the heat initial value problem with Heaviside initial conditions ($S(x,t) = S_0 + C \times erf(\frac{19{,}270}{\sqrt{4Kt}})$) for CM17 in LSSFB during the winter 2015 - 2016 season. Green fit: $S_0 = 33.8$ PSU, $C = -12.4$ PSU, $K = 261\ m^2/s$; Red fit: $S_0 = 28.2$ PSU, $C = -7.96$ PSU, $K = 624\ m^2/s$; Blue fit: $S_0 = 29.9$ PSU, $C = -10.4$ PSU, $K = 295\ m^2/s$.

Dispersion Model

The tidally averaged equation 4.2 leaves a diffusion equation describing salinity transferred by a Fickian diffusion process. There are a large number of solutions for these equations. The most fundamental solution to the tidally averaged equation 4.2 is one with an initial salinity introduced at time $t = 0$ with a step function distribution in space. The initial condition is given by the step function

$$S(x,0) = \begin{cases} 0 & x < 0 \\ S & x > 0 \end{cases}$$

The fundamental solution takes a time-dependent, Gaussian form (Equation 4.5) [15, 21].

$$S(x,t) = S_0 + C \times erf(\frac{x_0}{\sqrt{4Kt}}) \tag{4.5}$$

Salinity time series can be fitted to the equation to determine best fit values of S_0, C, and K. The fitted value of S_0 is dependent on the starting salinity or offset which is of little interest for the hydrodynamics of a given estuary with a given bathymetry. The value of S_0 will be dependent on environmental factors, such as the timing and frequency of precipitation events. The value of S_0 will be greater with less freshwater input and lower with more freshwater input.

Fitting each time window to the above equation and substituting the distance from San Mateo Bridge to CM17 ($x_0 = 19{,}270$ meters) results in fits shown in Figure 4.18. When fitting to the heaviside solution estimates of the dispersion coefficient, K are 261 m^2/s, 624 m^2/s, and 295 m^2/s for the first (green), second (red), and third (blue) time windows. These

estimates of recovery are similar to longitudinal estuarine disperson estimates in literature. Dye experiments conducted in an Eastern Scheldt estuary scale model estimated estuarine disperson of $K \approx 200\ m^2/s$ [13]. Estimates in the Delaware River Estuary using USGS data and a one-dimensional steady state, spatially constant longitudinal dispersion coefficient found K to vary from 140 to 200 m^2/s [44], Lewis found that a longitudinal dispersion coefficient of $K = 100\ m^2/s$ was reasonably representative of dispersion in five UK estuaries [28], and a study on the spatial and temporal variability of longitudinal dispersion rates in Chesapeake Bay calculated dispersion coefficients between 200 and 1000 m^2/s with an average of 650 m^2/s [2]. All three estimates of K in Figure 4.18 are of the same order of magnitude to what was found in other estuaries, giving reassurance to the values found using this technique.

4.8 Summary

This chapter focused on conclusions about the seasonal variability of salinity and stratification. Based off observations, LSSFB has high variability of salinity in space and time. In the late summer, early fall months, LSSFB experiences maximum water temperatures ranging from 20 to 25 degrees Celsius along with little to no precipitation. In the winter months, LSSFB has water temperatures as low as 8 degrees Celsius with frequent and high volume precipitation events. Water temperature variability on a 24-hour window revealed four various time windows of heating and cooling patterns: nighttime ebb, daytime flood, daytime ebb, and nighttime flood. During each of these phases, there is either heating or cooling due to atmospheric temperatures and advection of perimeter waters into the estuary on ebb tides or waters from outside the mouth into the estuary on flood tides.

Comparisons of varying seasons reveled the most likely season for runaway stratification in LSSFB would be in winter months with high precipitation. As precipitation increases, buoyancy input increases resulting in stronger stratification events.

In this chapter, salinity recovery time series after precipitation events in the winter 2015-2016 season provided estimates of residence times and longitudinal dispersion rates. By fitting daily salinity minimums to an exponential decay function, the residence time of LSSFB was found to be on the order of two weeks. Using a dispersion model, the longitudinal dispersion rate was found to range from 100-600 m^2/s.

The next steps to further understand seasonal patterns in LSSFB is to create hindsight models which can fill in unknown data in space and time. With higher spatial and temporal resolution, the mechanisms creating seasonal variations in salinity and temperature can be defined.

Chapter 5

Conclusions

Rapid advancement of scientific research, coupled with its increasing specialization and technical language, widens the knowledge gap between scientists and lay public. Recent political events have farther revealed the disconnect between environmental scientists and the American public. As a democratic society, it is necessary for scientists to inform citizens of conclusions and findings from their research. As climate change will greatly affect coastal communities, the need to effectively communicate scientific findings in the Bay Area becomes of upmost importance. The communication of science has historically been a one-way flux of information, scientists informing public through the various channels of modern media [5]. The public has not often been included in the scientific process. Bensuade argues that "the world of knowledge is clearly divided into two categories: that of the scientists, who hold the monopoly of true, valid statements, and that of the rest, the numerous, anonymous, and amorphous mass forming the public" [5]. The notion of science being based on hard facts, does not disqualify the public's knowledge. In an attempt to contribute to accessibility, I've presented hand-drawn graphics of estuarine dynamics in this section.

This dissertation aimed to identify seasonal and tidal patterns of stratification and temperature for environmental policy makers and environmental scientists interested in potential harmful algal blooms in Lower South San Francisco Bay. Based on a quantitative and qualitative analysis of salinity, temperature, and velocity measurements throughout the estuary, it can be concluded that changes in seasonal climate patterns are important factors to consider when setting restrictions on the future nutrient inputs into the bay. The results indicate that salinity and stratification in the estuary is highly dependent on seasonal precipitation. As we expect more prolonged drought seasons and more extreme precipitation events in the future, it creates a greater risk for the development of harmful algal blooms.

These observations in LSSFB revealed the complex, 3-dimensional nature of the creation and destruction of stratification. Chapter 2 discussed the timing of longitudinal and lateral dynamics and their role in the creation and destruction of stratification on a tidal time scale. Figure 5.1 summarizes the tidal pattern of stratification. These observations show the need to include both longitudinal and lateral dynamics in understanding and modeling stratification. In the past, literature has focused on either longitudinal mechanisms creating

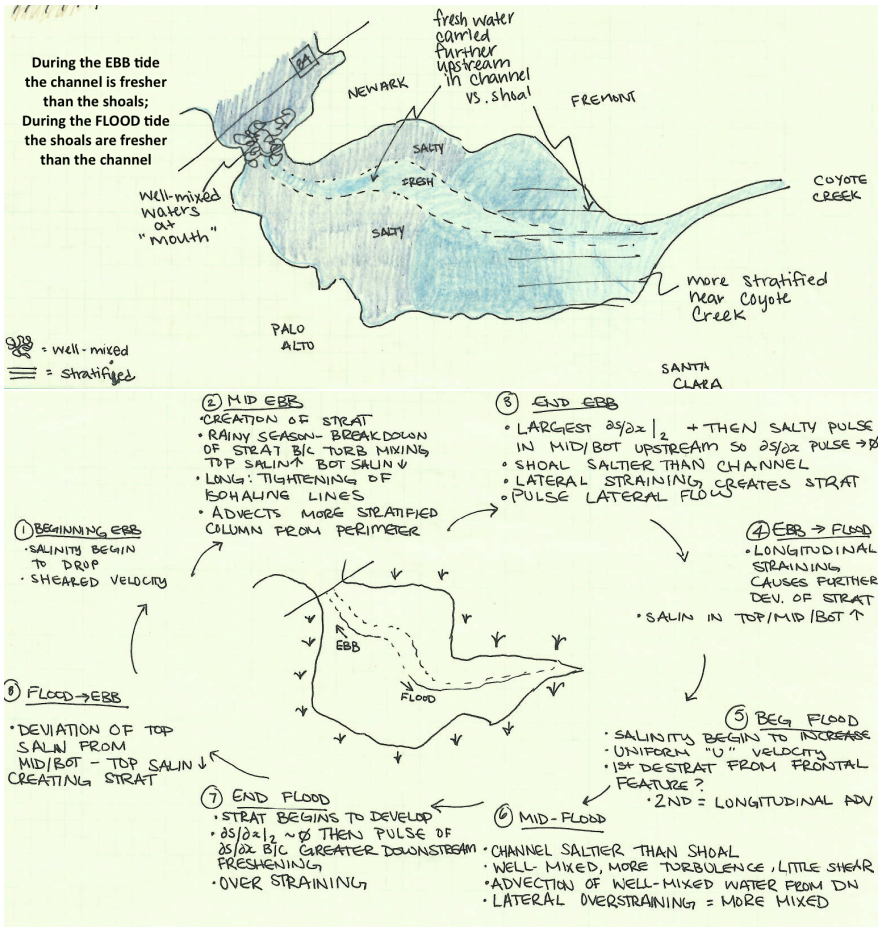

Figure 5.1: Top panel is a sketch of LSSFB over an ebb tide. Note: After the end of a flood tide, the lateral density gradient can reverse due to differential advection meaning the channel is more saline than the shoals. The bottom panel describes the characteristics in the tidal creation and destruction of stratification.

and destroying stratification or lateral mechanisms. Since LSSFB has close proximity to its perimeter, it is necessary to look at both the longitudinal and lateral mechanisms to accurately capture tidal patterns of salinity and stratification.

Lateral exchanges at tide transitions play an important role in the tidal salinity and stratification pattern. During tide transitions, the lateral salinity gradient is at a maximum while the velocity is at a minimum often resulting in lateral exchange. On the ebb to flood tide transition, the salinity in the channel is fresher than the salinity in the shoal resulting in an increase of salinity to the entire water column. On the flood to ebb tide transition, a two-layer lateral exchange is developed causing a decrease of salinity at the top of the water column within the channel. Figure 5.2 summarizes the lateral exchange pattern.

Chapter 4 describes the seasonal variation of salinity and temperature in LSSFB. There is high seasonal variability in terms of precipitation which leads to high variability in salinity

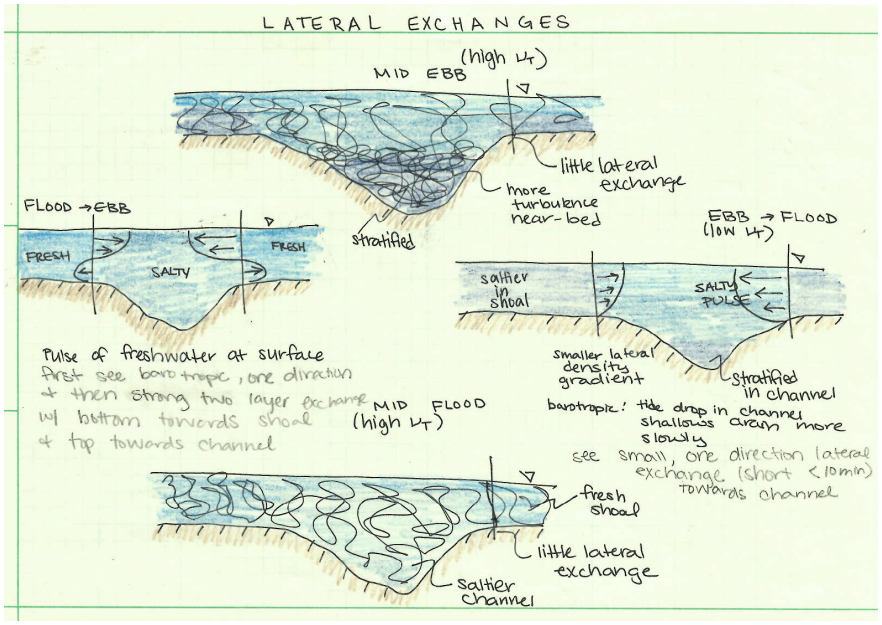

Figure 5.2: Snapshots of lateral cross-sections in LSSFB over a tidal cycle. The figure should be read in a clockwise direction.

and stratification. When precipitation increases, there is greater input of freshwater causing lower salinity throughout the estuary and increased stratification. LSSFB has high spatial variability of salinity throughout all seasons further stressing the importance of looking at all three dimensions when modeling estuaries. In the channel of the estuary, salinity ranges from 0 PSU to 33 PSU over a given year. Observations of perimeter salinity shows tidal variability patterns similar to observed patterns in the channel but with larger fluctuations. Based on seasonal variations, the most likely season of runaway stratification would be seasons with the largest buoyant input. For LSSFB, this tends to be in the winter months (December through February).

Another goal of this dissertation is to quantify estuarine residence time and longitudinal disperson rates for LSSFB. Based on a quantitative analysis of salinity and temperature time series, it can be concluded that the residence time of LSSFB is on the order of 2-3 weeks while the longitudinal dispersion rate is between 50 - 600 m^2/s. Future estuarine models can be refined through the estimation of residence time and longitudinal dispersion rate.

Observations of temperature revealed high seasonal and spatial variation in water column temperature. At the center of LSSFB in the channel, water column temperature ranges from 8 degrees Celsius in the winter season, minimizing in January, to 25 degrees Celsius in the summer and fall season, maximizing in the months of June, July, and August. Within the seasonal temperature fluctuations, there are two-week fluctuations of 5 degree Celsius which could be explained by the offset between the tides (M2 tide, 12.4 hours) and atmospheric heating and cooling (24 hours). Further research is needed to determine the causes of the

two-week fluctuations.

To better understand the implications of these results, future models should be used to address maximum nutrient limits in LSSFB before an onset of an algal bloom based on new climate conditions. While this research clearly illustrates how stratification and temperature in the estuary is affected by varied precipitation and atmospheric temperatures, it raises the question of how climate adjustments will affect the ecology.

Bibliography

[1] John C. Andrews and Hans Muller. "Space-time variability of nutrients in a lagoonal patch reef". In: *Limnology and Oceanography* 28.2 (1983). DOI: 10.4319/lo.1983.28.2.0215.

[2] Jay A. Austin. "Estimating effective longitudinal dispersion in the Chesapeake Bay". In: *Estuarine, Coastal and Shelf Science* 60 (2004). DOI: 10.1016/j.ecss.2004.01.012.

[3] Ben K. Basu and Frances R. Pick. "Factors regulating phytoplankton and zooplankton biomass in temperate rivers". In: *Limnology and Oceanography* 41.7 (1996). DOI: 10.4319/lo.1996.41.7.1572.

[4] Johannes Becherer et al. "Lateral Circulation Generates Flood Tide Stratification and Estuarine Exchange Flow in a Curved Tidal Inlet". In: *Journal of Physical Oceanography* 45 (2014). DOI: 10.1175/JPO-D-14-0001.1.

[5] Bernadette Bensaude-Vincent. "A genealogy of the increasing gap between science and the public". In: *Public Understanding of Science* 10 (2001). DOI: 10.3109/a036858.

[6] John Bourgeois. *South Bay Salt Pond Restoration Project*. [Online; accessed 2014-03-30]. URL: http://www.southbayrestoration.org/.

[7] K. F. Bowden and S. H. Sharaf El Din. "Circulation, Salinity and River Discharge in the Mersey Estuary". In: *Geophysical Journal International* 10.4 (1966). DOI: 10.1111/j.1365-246X.1966.tb03066.x.

[8] W. R. Boynton et al. "Inputs, Transformations, and Transport of Nitrogen and Phosphorus in Chesapeake Bay and Selected Tributaries". In: *Estuaries* 18.18 (1995). DOI: 10.2307/1352640.

[9] V. Monica Bricelj and Darcy J. Lonsdale. "Aureococcus anophagefferens: Causes and ecological consequences of brown tides in U.S. mid-Atlantic coastal waters". In: *Limnology and Oceanography* 45.5, part 2 (1997). DOI: 10.4319/lo.1997.42.5_part_2.1023.

[10] David L. Christensen et al. "Pelagic responses to changes in dissolved organic carbon following division of a seepage lake". In: *Limnology and Oceanography* 41.3 (1996). DOI: 10.4319/lo.1996.41.3.0553.

[11] James E. Cloern et al. "Projected Evolution of California's San Francisco Bay-Delta-River System in a Century of Climate Change". In: *PLoS ONE* 6.9 (2011). DOI: 10.1371/journal.pone.0024465.

[12] Audric G. Collignon and Mark T. Stacey. "Intratidal Dynamics of Fronts and Lateral Circulation at the Shoal-Channel Interface in a Partially Stratified Estuary". In: *Journal of Physical Oceanography* 42 (2012). DOI: 10.1175/JPO-D-11-065.1.

[13] J. Dronkers and J. T. F. Zimmerman. "Some principles of mixing in tidal lagoons". In: *Oceanologica Acta* (1982).

[14] Keith R. Dyer. *Estuaries: a physical introduction*. John Wiley, 1973. ISBN: 0471229059.

[15] Hugo Fischer et al. *Mixing in Inland and Coastal Waters*. Academic Press, 1979. ISBN: 9780122581502.

[16] Amy C. Foxgrover et al. "2005 Hydrographic Survey of South San Francisco Bay, California". In: *U.S. Geological Survey Open-File Report* (2007). DOI: 10.3133/ofr20071169.

[17] W Rockwell Geyer. "Influence of Wind on Dynamics and Flushing of Shallow Estuaries". In: *Estuarine, Coastal and Shelf Science* 44.6 (1997). DOI: 10.1006/ecss.1996.0140.

[18] W Rockwell Geyer, R. Chant, and R. Houghton. "Tidal and spring-neap variations in horizontal dispersion in a partially mixed estuary". In: *Journal of Geophysical Research* 113 (2008). DOI: 10.1029/2007JC004644.

[19] W Rockwell Geyer and Parker MacCready. "The Estuarine Circulation". In: *Annual Review of Fluid Mechanics* 46 (2014). DOI: 10.1146/annurev-fluid-010313-141302.

[20] W Rockwell Geyer, John Trowbridge, and Melissa Bowen. "The Dynamics of a Partially Mixed Estuary". In: *Journal of Physical Oceanography* 30 (2000). DOI: 10.1175/1520-0485(2000)030<2035:TDOAPM>2.0.CO;2.

[21] Alexander Grigoryan. *Heat Kernel and Analysis on Manifolds*. Bielefeld, Germany: International Press, 2000.

[22] Donald V. Hansen and Maurice Rattray Jr. "New Dimensions in Estuary Classification". In: *Limnology and Oceanography* 11.3 (1966). DOI: 10.4319/lo.1966.11.3.0319.

[23] Linda Huzzey and John Brubaker. "The formation of longitudinal fronts in a coastal plain estuary". In: *Journal of Geophysical Research* 93.C2 (1988). DOI: 10.1029/JC093iC02p01329.

[24] David Jay and J. Dungan Smith. "Circulation, density distribution and neap-spring transitions in the Columbia River Estuary". In: *Progress in Oceanography* 25 (1990). DOI: 10.1016/0079-6611(90)90004-L.

[25] Jessica Lacy et al. "Interaction of lateral baroclinic forcing and turbulence in an estuary". In: *Journal of Geophysical Research* 108.C3 (2003). DOI: 10.1029/2002JC001392.

[26] James Lerczak and W. Rockwell Geyer. "Modeling the Lateral Circulation in Straight, Stratified Estuaries". In: *Journal of Physical Oceanography* 34 (2004). DOI: 10.1175/1520-0485(2004)034<1410:MTLCIS>2.0.CO;2.

[27] James Lerczak, W. Rockwell Geyer, and Robert J. Chant. "Mechanisms Driving the Time-Dependent Salt Flux in a Partially Stratified Estuary". In: *Journal of Physical Oceanography* 36 (2006). DOI: 10.1175/JPO2959.1.

[28] Roy E. Lewis and Reginald J. Uncles. "Factors affecting longitudinal dispersion in estuaries of different scale". In: *Ocean Dynamics* 53 (2003). DOI: 10.1007/s10236-003-0030-2.

[29] Lisa Lucas et al. "Processes governing phytoplankton blooms in estuaries. I: The local production-loss balance". In: *Marine Ecology Progress Series* 187 (1999). DOI: 10.3354/meps187001.

[30] Parker MacCready. "Calculating Estuarine Exchange Flow Using Isohaline Coordinates". In: *Journal of Physical Oceanography* 41 (2011). DOI: 10.1175/2011JPO4517.1.

[31] Parker MacCready, W. Rockwell Geyer, and Hans Burchard. "Estuarine Exchange Flow Is Related to Mixing through the Salinity Variance Budget". In: *Journal of Physical Oceanography* 48 (2018). DOI: 10.1175/JPO-D-17-0266.1.

[32] Parker MacCready, Robert D. Hetland, and W. Rockwell Geyer. "Long-term isohaline salt balance in an estuary". In: *Continental Shelf Research* 22 (2001). DOI: 10.1016/S0278-4343(02)00023-7.

[33] Frank Melzner et al. "Future ocean acidification will be amplified by hypoxia in coastal habitats". In: *Marine Biology* 160.8 (2013). DOI: 10.1007/s00227-012-1954-1.

[34] Stephen G. Monismith, Jon R. Burau, and Mark T. Stacey. "Stratification dynamics and gravitational circulation in northern San Francisco Bay". In: *San Francisco Bay: The Ecosystem* (1996). Ed. by James T. Hollibaugh.

[35] Nancy E. Monsen et al. "A comment on the use of flushing time, residence time, and age as transport time scales". In: *Limnology and Oceanography* 47.5 (2002). DOI: 10.4319/lo.2002.47.5.1545.

[36] H-M Nepf and W. Rockwell Geyer. "Intratidal variations in stratification and mixing in the Hudson estuary". In: *Journal of Geophysical Research* 101.C5 (1996). DOI: 10.1029/96JC00630.

[37] NOAA. *ERDDAP: Easier access to scientific data.* [Online; accessed 2015]. URL: https://coastwatch.pfeg.noaa.gov/erddap/index.html.

[38] National Oceanic and Atmospheric Administration. *Alameda, CA - Station ID: 9414750.* [Online; accessed 2019-05-19]. URL: https://tidesandcurrents.noaa.gov/stationhome.html?id=9414750.

[39] National Oceanic and Atmospheric Administration. *What are spring and neap tides?* [Online; accessed 2019-11-01]. URL: https://oceanservice.noaa.gov/facts/springtide.html.

[40] Scripps Institution of Oceanography. *Scripps Institution of Oceanography SIO 20.* [Online; accessed 2018-08]. URL: http://meteora.ucsd.edu/~iacob/es20/slides/slides012513.pdf.

[41] Mark D. Ohman and Simon N. Wood. "Mortality estimation for planktonic copepods: Pseudocalanus newmani in a temperate fjord". In: *Limnology and Oceanography* 41.1 (1996). DOI: 10.4319/lo.1996.41.1.0126.

[42] Anabela Oliveira and Antonio M. Baptista. "Diagnostic modeling of residence times in estuaries". In: *Water Resources Research* 33.8 (1997). DOI: 10.1029/97WR00653.

[43] Jean Painchaud et al. "Bacterial dynamics in the upper St. Lawrence estuary". In: *Limnology and Oceanography* 41.8 (1996). DOI: 10.4319/lo.1996.41.8.1610.

[44] Richard W. Paulson. "Variation of the Longitudinal Dispersion Coefficient in the Delaware River Estuary as a Function Freshwater Inflow". In: *Water Resources Research* 6.2 (1970). DOI: 10.1029/WR006i002p00516.

[45] Ruskin. *RBRdue and RBRconcerto.* [Online; accessed 2018-04-15]. URL: https://rbr-global.com/products/standard-loggers/rbrduo-ct.

[46] Lawrence P. Sanford, William C. Boicourt, and Stephen R. Rives. "Model for Estimating Tidal Flushing of Small Embayments". In: *Journal of Waterway, Port, Coastal, and Ocean Engineering* 118.6 (1992). DOI: 10.1061/(ASCE)0733-950X(1992)118:6(635).

[47] David H. Schoellhamer. "Sudden Clearing of Estuarine Waters upon Crossing the Threshold from Transport to Supply Regulation of Sediment Transport as an Erodible Sediment Pool is Depleted: San Francisco Bay, 1999". In: *Estuaries and Coasts* 34 (2011). DOI: 10.1007/s12237-011-9382-x.

[48] Seabird Scientific. *SBE 37-SM MicroCAT C-T (P) Recorder.* [Online; accessed 2018-04-15]. URL: http://www.seabird.com/sbe37sm-microcat-ctd/.

[49] Malcom Scully and Carl T. Friedrichs. "The Importance of Tidal and Lateral Asymmetries in Stratification to Residual Circulation in Partially Mixed Estuaries". In: *Journal of Physical Oceanography* 37.6 (2007). DOI: 10.1175/JPO3071.1.

[50] Malcom Scully and W Rockwell Geyer. "The Role of Advection, Straining, and Mixing on the Tidal Variability of Estuarine Stratification". In: *Journal of Physical Oceanography* 42 (2012). DOI: 10.1175/JPO-D-10-05010.1.

[51] Jian Shen and Harry V. Wang. "Determining the age of water and long-term transport timescale of the Chesapeake Bay". In: *Estuarine, Coastal and Shelf Science* 74 (2008). DOI: 10.1016/j.ecss.2007.05.017.

[52] J-H Simpson et al. "Tidal Straining, Density Currents, and Stirring in the Control of Estuarine Stratification". In: *Estuaries* 13.2 (1990). DOI: 10.2307/1351581.

[53] Mark Stacey, Jon Burau, and Stephen Monismith. "Creation of residual flows in a partially stratified estuary". In: *Journal of Physical Oceanography* 106.C8 (2001). DOI: 10.1029/2000JC000576.

[54] Mark Stacey, Stephen Monismith, and Jon Burau. "Observations of Turbulence in a Partially Stratified Estuary". In: *Journal of Physical Oceanography* 29 (1999). DOI: 10.1175/1520-0485(1999)029<1950:OOTIAP>2.0.CO;2.

[55] Stanford. *Lecture 2: physical characteristics of the ocean*. [Online; accessed 2019-11]. URL: https://pangea.stanford.edu/courses/EESS146Bweb/Lecture%5C%202.pdf.

[56] Robert V. Thomann and John A. Mueller. *Principles of Surface Water Quality Modeling and Control*. Harper Row, 1997. ISBN: 9780060466770.

[57] Ivan Valiela et al. "Macroalgal blooms in shallow estuaries: Controls and ecophysiological and ecosystem consequences". In: *Limnology and Oceanography* 42.5, part 2 (1997). DOI: 10.4319/lo.1997.42.5_part_2.1105.

[58] California Department of Water Resources. *California Irrigation Management Information System (CIMIS)*. [Online; accessed 2017-04-15]. URL: http://www.cimis.water.ca.gov/.

[59] Frances P. Wilkerson et al. "Phytoplankton Blooms and Nitrogen Productivity in San Francisco Bay". In: *Estuaries and Coasts* 29.3 (2006). DOI: 10.1007/BF02784989.

[60] Taylor Winchell et al. "Nutrient Moored Sensor Program: Program Update". In: (2018).